

REGISTRATION AND ANALYSIS OF DEVELOPMENTAL IMAGE SEQUENCES

Istvan Csapo

A dissertation submitted to the faculty of the University of North Carolina at Chapel Hill in
partial fulfillment of the requirements for the degree of Doctor of Philosophy in the
Department of Computer Science.

Chapel Hill
2018

Approved by:
Marc Niethammer
Martin Styner
Eva Anton
Alex Berg
Vladimir Jojic

©2018
Istvan Csapo
ALL RIGHTS RESERVED

ABSTRACT

Istvan Csapo: Registration and Analysis of Developmental Image Sequences
(Under the direction of Marc Niethammer)

Mapping images into the same anatomical coordinate system via image registration is a fundamental step when studying physiological processes, such as brain development. Standard registration methods are applicable when biological structures are mapped to the same anatomy and their appearance remains constant across the images or changes spatially uniformly. However, image sequences of animal or human development often do not follow these assumptions, and thus standard registration methods are unsuited for their analysis.

In response, this dissertation tackles the problems of i) registering developmental image sequences with spatially non-uniform appearance change and ii) reconstructing a coherent 3D volume from serially sectioned images with non-matching anatomies between the sections.

There are three major contributions presented in this dissertation. First, I develop a similarity metric that incorporates a time-dependent appearance model into the registration framework. The proposed metric allows for longitudinal image registration in the presence of spatially non-uniform appearance change over time—a common medical imaging problem for longitudinal magnetic resonance images of the neonatal brain. Next, a method is introduced for registering longitudinal developmental datasets with missing time points using an appearance atlas built from a population. The proposed method is applied to a longitudinal study of young macaque monkeys with incomplete image sequences. The final contribution is a template-free registration method to reconstruct images of serially sectioned biological samples into a coherent 3D volume. The method is applied to confocal fluorescence microscopy images of serially sectioned embryonic mouse brains.

ACKNOWLEDGEMENTS

First and foremost, I thank my advisor, Marc Niethammer, for his support and unwavering enthusiasm. Marc is a generous mentor and a first-rate teacher. I am grateful for having had the opportunity to work with him.

I thank my committee, Martin Styner, Eva Anton, Alex Berg, and Vladimir Jovic for their support and valuable feedback. My collaborators at the Neuro Image Research and Analysis Laboratories, Martin Styner and Yundi Shi, contributed heavily to the work presented in the first part of this dissertation.

It has been a great pleasure to work with the members of the Anton Lab and the associated staff at the Department of Cell Biology and Physiology. I am especially thankful to Eva Anton for sharing his deep knowledge of brain development and giving me the opportunity to work on such a fundamentally important problem; to Martis Cowles for the excellent discussions and close collaboration on the neuron migration project; to Gary Wilkins for spending countless hours behind the microscope to collect our images and teaching me the surgical and lab skills used to prepare the samples; and to Vladimir Ghukasyan for improving our images and teaching me how to use the confocal microscope.

I thank my fellow lab mates, Tian Cao, Heather Couture, Yi Hong, Liang Shan, and Xiao Yang—I drew a lot of inspiration from their work. I thank the faculty and staff members of the Department of Computer Science who were always willing to help.

Finally, I thank my parents for their encouragement and support.

TABLE OF CONTENTS

LIST OF TABLES	viii
LIST OF FIGURES	ix
LIST OF ABBREVIATIONS	xii
1 Introduction	1
1.1 Motivation	1
1.1.1 Temporally-Dependent Image Similarity Measure	3
1.1.2 Registration of Developmental Image Sequences with Missing Data.....	3
1.1.3 3D Reconstruction of Serially Sectioned Images	4
1.2 Thesis and Contributions	5
1.3 Overview of Chapters	6
2 Background	7
2.1 Image Registration	7
2.1.1 Similarity Measures	9
2.1.2 Regularization.....	10
3 Temporally-Dependent Image Similarity Measure	12
3.1 Model-Based Similarity Measure	14
3.1.1 General Local Intensity Model Estimation for SSD	14
3.1.2 Logistic Intensity Model with Elastic Deformation	15
3.2 Parameter Estimation	16
3.2.1 Registration Model	16
3.2.2 Model Parameter Estimation	17

3.3	Experimental Results	17
3.3.1	White Matter Intensity Distributions from Real Data	19
3.3.2	Experiment 1: Model Selection	20
3.3.3	Experiment 2: Synthetic Data	23
3.3.3.1	Affine transformation model	24
3.3.3.2	Deformable registration	25
3.3.4	Experiment 3: Simulated Brain Data	25
3.3.4.1	Smoothing kernel size	28
3.3.4.2	White matter segmentation	28
3.3.5	Experiment 4: Monkey Data	29
3.4	Conclusions.....	32
4	Quantitative MRI Atlas of Postnatal Rhesus Macaque Brain Maturation	34
4.1	Introduction.....	34
4.2	Estimating the Atlas from a Population	36
4.2.1	Monkey Dataset	37
4.2.2	Model Estimation	38
4.2.3	Comparison to Expected Myelination Pattern	39
4.3	Conclusions.....	41
5	Registration of Developmental Image Sequences with Missing Data	42
5.1	Using the Maturation Information	43
5.2	Experimental Results	43
5.2.1	Registering Synthetic 2D Dataset.....	44
5.2.2	Registering Real 3D Dataset	46
5.2.2.1	Accuracy of affine registration.....	46
5.2.2.2	Influence of prior with missing data.....	50
5.3	Conclusions.....	51
6	3D Reconstruction of Serially Sectioned Images.....	53

6.0.1	Previous Work	56
6.1	Image Acquisition.....	58
6.1.1	Measuring Tissue Loss Due to Sectioning.....	59
6.2	3D Reconstruction	62
6.2.1	Manual Preprocessing	65
6.2.2	Intensity Normalization	67
6.2.3	Segmentation.....	67
6.2.4	Stacking	69
6.2.5	Reconstruction	70
6.3	Experimental Results	71
6.3.1	Reconstructing 3D Synthetic Data	72
6.3.1.1	Experiment.....	72
6.3.2	Reconstructing Confocal Microscopy Embryonic Mouse Data	74
6.3.3	Mapping Neuron Migration in the Developing Brain	76
6.4	Conclusions.....	80
7	Discussion	84
7.1	Summary of Contributions.....	84
7.2	Future Work	87
7.2.1	Model-Based Similarity Measure	87
7.2.2	Atlas of Brain Maturation	87
7.2.3	Template-free 3D Reconstruction.....	88
	BIBLIOGRAPHY	89

LIST OF TABLES

3.1	Model selection experiment results	23
3.2	Landmark registration error	31
5.1	Registration error for synthetic data experiment with varying prior weights	45
5.2	Registration error for monkey data experiment	51
6.1	Mouse confocal fluorescence microscopy datasets	60

LIST OF FIGURES

1.1	Mouse embryo development: 9.5-12.5 days	2
2.1	Registration overview	7
2.2	Standard similarity measures.....	10
3.1	Simplified model of neurodevelopment	12
3.2	Logistic intensity model	15
3.3	Synthetic dataset with logistic white matter intensity change and longitudinal deformation over time	18
3.4	Simulated brain images	19
3.5	Spatiotemporal distribution of white matter intensities in 9 monkeys	20
3.6	Synthetic datasets with 10 time points generated with various intensity models	21
3.7	The influence of the intensity model on the registration.....	22
3.8	Experimental setup for synthetic datasets	24
3.9	Experiment 1: results with affine transformation	26
3.10	Experiment 1: results with deformable transformation.....	27
3.11	The effect of various smoothing kernel sizes on the intensity model estimation	29
3.12	SSR registration: effect of smoothing kernel size.....	30
3.13	SSR registration: effect of white matter segmentation accuracy	30
3.14	Corresponding target and source landmarks for a single subject	31
3.15	Experimental setup and results for a single subject	32
3.16	Landmark distance mismatch	33
4.1	Axial slices of MR brain images of monkey at ages 2 weeks, 3, 6, 12, and 18 months	35
4.2	Example of an expert-defined anatomical landmark	37
4.3	Intensity model	39
4.4	Estimated onset and rate of maturation	40

5.1	Synthetic dataset with logistic white matter intensity change	44
5.2	Registration results with no prior	46
5.3	Subset of landmarks	47
5.4	Cartoon depiction of the typical anterior-posterior deformation	49
5.5	Landmark errors per time point	49
5.6	Registration results for a single subject	52
6.1	Neurogenesis and differentiation	54
6.2	Mouse embryo development	58
6.3	Serial sectioning of the embryonic mouse brain	59
6.4	Microscopy imaging of tissue sections	61
6.5	Tissue loss of confocal microscopy sections	63
6.6	Synthetic serially-sectioned dataset	64
6.7	Serially-sectioned mouse embryo dataset	65
6.8	Optical slices from a tissue section	66
6.9	Evaluation of the tissue mask	67
6.10	Intensity normalization of tissue sections	68
6.11	Serially-sectioned dataset tissue masks	69
6.12	3D reconstruction algorithm	71
6.13	3D synthetic dataset: reconstruction example	73
6.14	3D synthetic dataset: reconstruction results	74
6.15	3D synthetic dataset: reconstruction errors	75
6.16	Mouse dataset reconstruction results: axial view	75
6.17	Mouse dataset reconstruction results: E14	76
6.18	Mouse dataset reconstruction results: E16	77
6.19	Mouse dataset reconstruction results: E18	78
6.20	Mouse dataset reconstruction results: FAS	78
6.21	Reconstruction results summary	79

6.22	3D reconstruction results	81
6.23	3D neuron migration atlas	82
6.24	3D neuron migration atlas: cross-sectional views	83

LIST OF ABBREVIATIONS

CT	Computed Tomography
MI	Mutual Information
MR	Magnetic Resonance
MRI	Magnetic Resonance Imaging
NCC	Normalized Cross Correlation
SSD	Sum of Squared Differences
SSR	Sum of Squared Residuals
STD	Standard Deviation

CHAPTER 1

Introduction

1.1 Motivation

With the advancement of biological imaging technologies, living organisms can be studied at an ever increasing spatial and temporal resolution. Various imaging modalities provide measurements at scales ranging from the molecular mechanisms of individual cells to the structural organization of whole organ systems. The latest microscopy and genetic techniques have allowed researchers to continuously capture and track thousands of cells during the development of the fruit fly embryo (Amat and Keller, 2013) and image the complete real-time neuronal activity of the zebrafish (Keller and Ahrens, 2015). These advances in biological imaging technologies, coupled with advances in genetics (Deisseroth, 2015) and biochemistry (Chung and Deisseroth, 2013), enabled researchers to probe and study complex biological processes in unprecedented detail.

One of the most complex biological processes is animal development. In the earliest stages of embryonic development, a single cell is transformed into thousands of cells that are organized into tissues and further grouped into organs and organ systems to form a fully functional organism. In later stages, neural circuitry is established in the central nervous system and neurons form a dense network of synaptic, electric, and modulatory connections from which function and complex behaviors arise. Normal function is dependent on the proper structural organization of cells at various scales, and disruptions to the orderly organization of cells can have severe detrimental effects on the developed organism. In humans, disruptions during the development of the central nervous system can lead to impairment that continues through adult life and may cause a wide variety of disorders, including autism spectrum disorders and schizophrenia (Bailey, 1998; Bill and Geschwind, 2009; Evsyukova et al., 2013).

As imaging techniques continue to improve, the data produced from the study of developmental processes is becoming increasingly detailed and spans enormous structural and functional changes. An illustrative example of the vast changes that can occur in a short period of time is the developmental

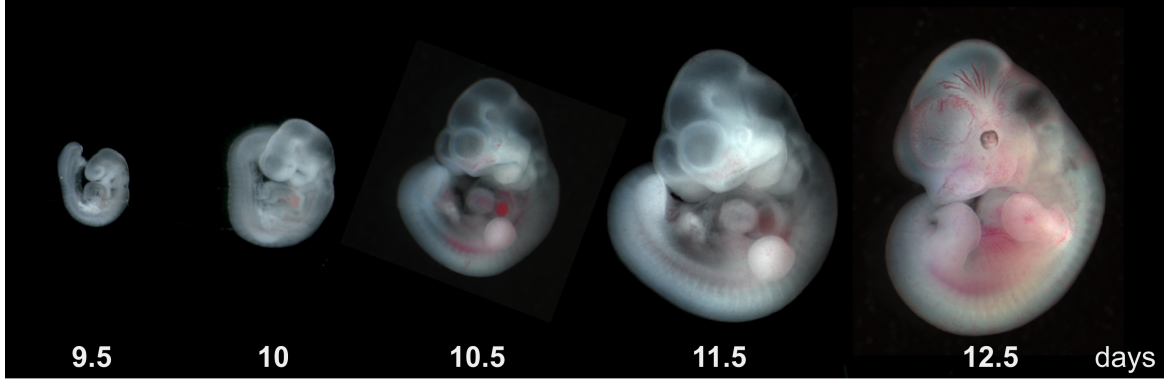


Figure 1.1: Mouse embryo development from embryonic age 9.5 days to 12.5 days [Image from: Dr. Erica D. Watson, University of Cambridge (with permission)].

stages of the mouse embryo shown in Figure 1.1. The first three images span only 24 hours and a single confocal fluorescence microscopy acquisition of one of the embryonic brains (a dataset analyzed in a later chapter), that is no larger than $2mm^3$, can generate 5×10^9 voxels with high enough resolution to show individual neuronal axons.

The nonlinear nature of the appearance and shape change of anatomical structures during development pose a significant challenge for accurate analysis. Many of the existing methods to analyze and quantify biological imaging data rely on assumptions of similarities in structure and appearance between individual images that no longer hold for these highly dynamic datasets. New image analysis methods are required to model complex developmental processes and to uncover subtle deviations from normal development while being able to deal with the large structural and appearance changes present in the image sequences.

One of the fundamental image analysis steps is mapping images into the same coordinate system. For biological datasets, this coordinate system is commonly in anatomical space and the mapping is established via image registration. There are two primary approaches for establishing the mapping between images. The first uses common features, such as edges or segmented structures, in the images to find corresponding points. The second approach, used in this dissertation, is based on the intensity values of the images directly without extracting any geometric features.

The intensity-based registration method aims to deform one or more of the images to match the intensity values across the images based on a measure of similarity. Commonly-used similarity measures for image registration are the sum of squared differences (SSD), normalized cross correlation (NCC), and mutual information (MI). All three measures rely on assumptions about the intensity distribution of

the anatomically equivalent structures in the images that do not hold for many datasets acquired during development.

This dissertation focuses on registration methods for biological image sequences acquired during development. There are three primary contributions. The first contribution is a model-based similarity measure for longitudinal image registration in the presence of spatially non-uniform appearance change over time. The second contribution is a method for registering longitudinal datasets with missing time points, using an appearance atlas built from a population. The third contribution is a template-free registration method to reconstruct images of serially-sectioned biological samples into a coherent 3D volume.

1.1.1 Temporally-Dependent Image Similarity Measure

Certain biological processes are best studied by acquiring in-vivo longitudinal image sequences of the organism. One such process is brain development. The resulting time-varying datasets often capture not only the considerable morphological changes, but also appearance changes. Mapping such image sequences into the same anatomical coordinate system is challenging since standard similarity measures rely on strong assumptions about the appearance of anatomical structures that no longer hold in this case. These similarity measures are too restrictive to account for the appearance change of the same anatomical structures and instead induce deformations—that result in incorrect mapping between images—to achieve similarity.

In order to facilitate the correct mapping between anatomical structures that go through appearance change, I present a novel similarity metric that incorporates a time-dependent appearance model into the registration framework. The model is used to change the appearance of the target image to match the moving image. Then the moving image can be registered to the intensity-adjusted target image, effectively removing the appearance change for a good model.

1.1.2 Registration of Developmental Image Sequences with Missing Data

Collecting longitudinal imaging data is challenging; the same organism has to be imaged multiple times. Depending on the biological process and the organisms being studied, longitudinal studies can span only minutes or multiple decades. It is not uncommon that some of the images cannot be acquired or

some acquisitions are corrupted and the resulting dataset is incomplete. While an improvement over the standard similarity measures, the temporally-dependent similarity measure I present is fully data-driven and parameter estimation may, therefore, become unreliable if the number of images in the longitudinal dataset is low. Furthermore, estimation of the model parameters is not possible if the number of available images is lower than the number of unknowns in the parametric intensity model.

One approach to account for missing time points during the parameter estimation step is to include prior knowledge about the model parameters into the model. For the temporally-dependent similarity measure, I incorporate a population maturation atlas as a prior to better guide the deformable registration for longitudinal datasets with missing time points. The prior is weighted such that its influence diminishes as the number of available time points increases. The atlas is built from a population of rhesus macaque monkeys with complete longitudinal datasets, and the proposed method is evaluated on datasets with missing time points.

1.1.3 3D Reconstruction of Serially Sectioned Images

While longitudinal studies are powerful for studying certain biological processes over time, there are several tradeoffs compared to cross-sectional studies. In cross-sectional studies subjects are not imaged multiple times, but rather a section of the population is imaged once. This type of study design is practical since the images can be collected in a short period of time by choosing subjects that span the whole extent of the biological process of interest. For example, in order to study the effects of aging on the normal human brain, a cross-sectional study can collect data from young and old subjects at the same time instead of having to follow subjects for decades.

Another advantage of cross-sectional studies is ability to use destructive imaging techniques. For longitudinal studies, the organism has to remain intact and thus only in-vivo imaging techniques can be used. For studying brain development, this excludes high resolution microscopy techniques that usually require tissue staining and sectioning—although, this has been changing as new technologies such as light sheet ([Keller and Ahrens, 2015](#)) microscopy have enabled the high resolution in-vivo imaging of small organisms.

In order to study brain development at the resolution of individual neurons, fluorescence confocal microscopy is a commonly used technique which requires the sectioning and staining of the tissue samples. One fundamental analysis step for serially-sectioned samples is the reconstruction of the sectioned data

into a coherent 3D volume that resembles the geometry of the intact sample before sectioning. Existing reconstruction methods either require an imaging modality with dense structural information or using an external template as a reference image volume that is not available for many studies. I present a novel method for reconstructing serially-sectioned fluorescence microscopy images without an external template. These images also lack the dense structural information needed by many commonly used reconstruction methods.

1.2 Thesis and Contributions

Thesis: Advanced image registration methods can allow accurate anatomical mapping between images that are dissimilar in appearance or anatomy. Such registration methods are essential for analyzing animal brain development.

The following contributions are presented in this dissertation:

1. A temporally-dependent similarity measure to aid the registration of longitudinal datasets with appearance change over time.
2. A developmental atlas of the neonatal rhesus macaque brain that captures the appearance change of the maturing white matter in a population of normal subjects.
3. A longitudinal registration method that can use a population atlas to deal with missing time points in a longitudinal image sequence.
4. A template-free 3D reconstruction method for serially-sectioned image data acquired with an imaging modality that does not capture rich structural information from the samples.

1.3 Overview of Chapters

The remaining chapters are organized as follows:

Chapter 2 provides an overview of the topics that are discussed in this dissertation, including background on image registration focusing on similarity metrics and regularization.

Chapter 3 introduces a novel temporally-dependent similarity measure for longitudinal registration. The method is validated on two longitudinal datasets: a synthetic phantom image dataset and a real dataset of magnetic resonance images of the macaque brain, with manually selected landmarks for validation.

Chapter 4 presents a population atlas capturing the appearance changes over time of the macaque monkey during early postnatal development. The atlas is built from the parameters of the model-based similarity measure introduced in the previous chapter.

Chapter 5 presents a registration method, based on the temporally-dependent similarity measure, for longitudinal datasets with missing time points. The population atlas built in the previous chapter is used as a prior for this registration method.

Chapter 6 presents a novel approach for reconstructing images acquired from serially-sectioned biological samples into a coherent 3D volume, without relying on an external template.

Chapter 7 concludes the dissertation with a discussion of contributions and an outline of possible future work.

CHAPTER 2

Background

2.1 Image Registration

Finding correspondences between images is one of the fundamental problems of image analysis. Correspondence between images establishes a common coordinate system that is meaningful within the context of the image analysis problem. In medical image analysis, for example, the common coordinate system is often in anatomical space that allows mapping between structurally or functionally similar regions. Figure 2.1 shows the mapping between two brain images. Corresponding brain structures have a similar appearance in both images, hence an appearance based registration method can find the mapping between them. Registration can be performed between two or more images, but in this section I focus on registration problems involving two images. One image is usually referred to as the source (or moving) image and the other as the target (or fixed) image.

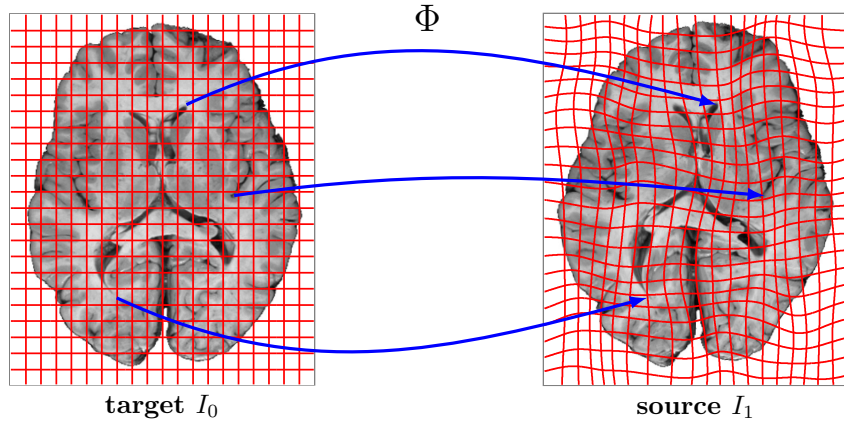


Figure 2.1: Spatial correspondence of two brain images. The space transformation Φ maps the coordinates of the target image to the corresponding anatomical coordinates of the source image. The aim of image registration is to recover Φ .

In order to find the mapping, a way of measuring similarity between the source and the target images needs to be established. Typically, similarity is measured by manually defined landmarks, matching

features between the images, or direct measures of image intensity differences (such as sum of squared difference, cross correlation, or mutual information). In medical image analysis, finding manually defined landmarks is prohibitively time consuming and most images lack reliable dense features; therefore, image intensity based measures are the most commonly used similarity measures. It is important to note that images are assumed to have similar structure and appearance for typical image registration methods. However, this assumption does not always hold for biological images of development, where not only the morphology but the appearance of the observed organisms or structures can change drastically over time as well.

The aim of image registration is to recover the transformation that maps the images into the same coordinate system, while simultaneously restricting the transformation to the space of feasible transformations. Feasibility, again, depends on the application, but typically the aim is to avoid folding or tearing in the deformed images. When registering bone, for example, we might want to allow only rigid transformations, but allow deformable transformations for soft tissue registration. One way to enforce feasible transformations and at the same time make the overall estimation problem well-posed is either by restricting the deformation model to parametric models (such as similarity, rigid, or affine) or, for non-parametric deformation models, by imposing regularity on the deformation field.

Formulating image registration as an optimization problem, we want to find a transformation Φ that minimizes the joint objective function

$$E = \underbrace{S[\Phi]}_{\text{regularizer}} + \frac{1}{\sigma^2} \underbrace{D[I_0, I_1 \circ \Phi^{-1}]}_{\text{similarity term}}, \quad (2.1)$$

where S is the regularization term that encourages Φ to be a plausible (usually smooth) transformation, D is the image similarity measure, $I_1 \circ \Phi^{-1}$ is the transformed source image, and σ controls the tradeoff between the regularization term and the image similarity term. Here, I chose to measure image similarity in the coordinate system of I_0 , but it can just as easily be done in the coordinate system of I_1 , or in a coordinate system halfway between the images making the registration results independent of such design choices. For simplicity, I measure similarity in the coordinate system of I_0 .

2.1.1 Similarity Measures

The role of the similarity term is to measure the quality of the alignment. The global optimum of the measure, therefore, should signal perfect alignment between the images. Three of the commonly used similarity measures are the sum of squared differences (SSD), normalized cross correlation (NCC), and mutual information (MI).

SSD assumes the image intensities to be identical at corresponding spatial locations ($I_0 = I_1$). This assumption is not valid for multimodal images or images with a change in appearance. It is the most specific similarity measure of the three and defined as

$$SSD[I_0, I_1] = \int_{\Omega} (I_0(x) - I_1(x))^2 dx,$$

where Ω is the image domain.

Normalized cross correlation is based on a weaker assumption of only an affine intensity relationship ($I_0 = aI_1 + b$):

$$NCC[I_0, I_1] = \frac{1}{\|I_0\| \|I_1\|} \int_{\Omega} I_0(x) I_1(x) dx,$$

where $\|I_i\| = \sqrt{\langle I_i, I_i \rangle}$ and $\langle \cdot, \cdot \rangle$ is the inner product.

Mutual information (MI) (Viola and Wells, 1995; Collignon et al., 1995) assumes a statistical relationship between the images without making any assumptions about the nature of this relationship. Therefore, it is suitable for a wide range of registration problems and it is the most general measure used for comparison in this thesis. The idea is to maximize the mutual information between two images with respect to the transformation. This is achieved by calculating the joint histogram, expressing the joint probabilities over the whole image. MI is defined as

$$MI[I_0, I_1] = H(I_0) + H(I_1) - H(I_0, I_1),$$

where $H(\cdot)$ is the marginal and $H(\cdot, \cdot)$ is the joint entropy. The joint entropy is calculated from the joint probability density, $\rho(i_0, i_1)$, of the images as

$$H(I_0, I_1) = - \sum_{i_0, i_1} \rho(i_0, i_1) \log \rho(i_0, i_1),$$

where i_0 and i_1 are the possible image intensities for I_0 and I_1 . In practice, the joint density is calculated from the joint image histogram and in that case i_0 and i_1 represent intensity ranges corresponding to the histogram bins. The marginal entropies are calculated similarly from the marginal densities. MI is maximum when the mapping between the intensities (or intensity ranges) i_0 and i_1 produces “sharp” joint histogram.

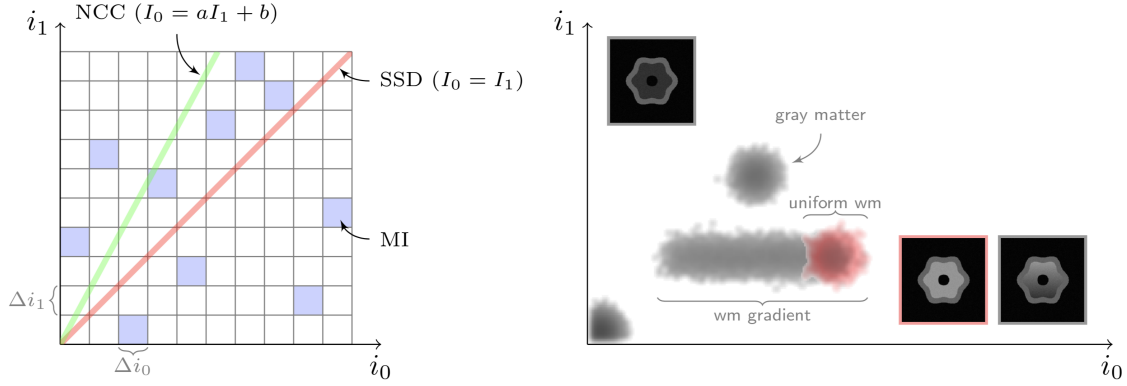


Figure 2.2: The graph on the left shows the optimal intensity relationships between two images I_0 and I_1 with intensities i_0 and i_1 , respectively, for SSD (red), NCC (green), and MI (blue). Δi_0 and Δi_1 are the histogram bin widths used for MI. Note that for MI the intensity ranges do not need to lie on a line. The graph on the right is the joint histogram of two synthetic images (gray matter is the thin outer layer, white matter is the inner gray region) I_1 and I_0 (perfectly aligned) with either uniform white matter or with a spatial white matter intensity gradient. In the presence of the gradient the optimal intensity relationship is not satisfied for any of the measures, and therefore they will induce registration errors.

2.1.2 Regularization

Image registration, in general, is an ill-posed problem since the solution that minimizes the similarity measure is often not unique. To single out a particular solution the regularization term S is added, which measures the quality or plausibility of the solution. Note that the regularization term can be usually omitted for low-dimensional transformation models (rigid, affine) and the registration still converges to a plausible solution. For high-dimensional, deformable transformation models, on the other hand, regularization is essential for avoiding implausible deformations that are not consistent with the physical properties of the deformed material (to avoid the folding of space, for example). Some regularizers for image registration include diffusion (used in optical flow (Horn and Schunck, 1981)), curvature (Fischer and Modersitzki, 2003), elastic (Broit, 1981) and fluid flow (Christensen et al., 1996).

In this dissertation, I use the elastic regularizer for the deformable registration experiments. It is based on the physical model of linear elasticity and it is defined on the displacement field u as

$$S[u] = \int_{\Omega} \frac{\mu}{4} \sum_{j,k=1}^d \underbrace{(\partial_{x_j} u_k + \partial_{x_k} u_j)^2}_{\text{rigidity}} + \frac{\lambda}{2} \underbrace{(\text{div } u)^2}_{\text{volume change}} dx,$$

where Ω is the image domain, μ and λ are the Lamé constants that control elastic behavior, and the div is the divergence operator defined as $\nabla \cdot u$, where ∇ is the gradient operator. I use $\mu = 1$ and $\lambda = 0$ unless noted otherwise (these and the trade off parameter between the regularization and the image match term were chosen based on visual inspection of test cases).

CHAPTER 3

Temporally-Dependent Image Similarity Measure

The effect of appearance change on the result of image registration depends on the chosen transformation model and the chosen image similarity measure. Generally, transformation models with few degrees of freedom (such as rigid or affine transformations) are affected less by local changes in image appearance than transformation models which can capture localized spatial changes, such as elastic or fluid models. As later shown in Section 3.3.3, affine methods perform well even in the presence of strong non-uniform appearance change, while deformable methods introduce erroneous local deformations in order to resolve inconsistencies in appearance. However, transformation models which can capture local deformations are desirable for many longitudinal studies as changes in morphology tend to be spatially non-uniform.

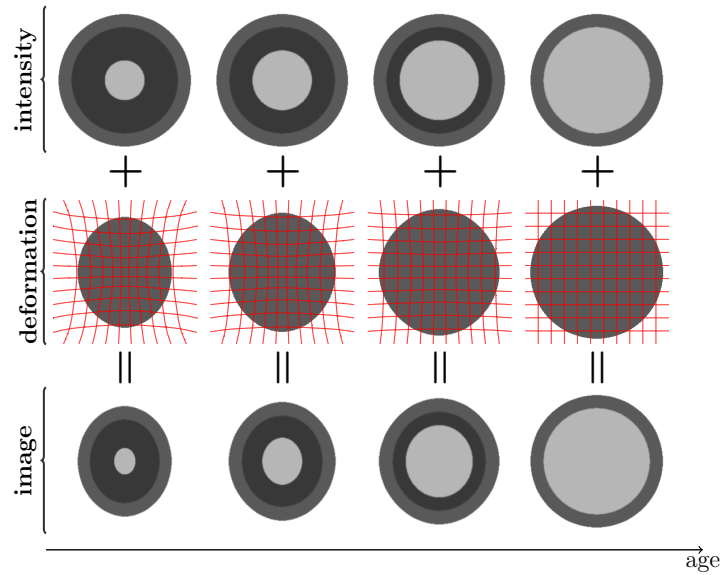


Figure 3.1: Simplified model of neurodevelopment. The outer ring represents gray matter; the bright central ring is the myelinating white matter surrounded by darker, unmyelinated white matter. The overall changes (*bottom row*; age increases to the right) can be decomposed into intensity changes due to the myelination process (*top row*) and morphological changes due to growth (*middle row*).

For longitudinal registration, temporal regularization of the transformation model has been explored recently. This is motivated by the assumption that unrealistic local changes can be avoided by enforcing temporal smoothness of a transformation (Durrleman et al., 2009; Fishbaugh et al., 2011). In this chapter, I instead focus on the complementary problem of determining an appropriate image similarity measure for longitudinal registration in the presence of temporal changes in image intensity.

Approaches which address non-uniform intensity changes have mainly addressed registration for image-pairs. These approaches either rely on local image uniformities (Loeckx et al., 2010; Studholme et al., 2006) or try to estimate image appearance changes jointly with an image transform (Friston et al., 1995; Roche et al., 2000; Miller and Younes, 2001; Periaswamy and Farid, 2003). Often (e.g., for bias field compensation in magnetic resonance imaging), image intensity changes are assumed to be smooth in both space and time. This assumption is not valid for certain applications, including longitudinal magnetic resonance (MR) imaging studies of neurodevelopment.

The changes seen on the MR images during neurodevelopment result from a variety of concurrent biological processes. Changes in various factors of tissue composition, such as myelin and water content, are coupled with both tissue generation and tissue loss (Casey et al., 2005). The majority of the changes seen in MR images, however, can be attributed to the myelination of the neuronal axons and morphological changes due to growth. In a simplified model of neurodevelopment, these two processes can be decoupled and modeled separately as shown in Figure 3.1. The goal is to register the images in the bottom row. Existing deformable registration algorithms can resolve the morphological differences between source and target images if the image intensities within tissue classes remain constant or vary slowly. Therefore, if the model of intensity change is known the intensity change can be modded out and the only remaining task of the registration method is to recover the spatial transformation (middle row), reducing the original problem to registering each source image in the bottom row to the corresponding intensity adjusted target image in the top row.

The proposed approach estimates local longitudinal models of intensity change using all available images. Once the intensity model is known, existing deformable registration methods can be used to find the spatial transformation between the images. The final solution is obtained by alternating between the parameter estimation for the local models of intensity change and the estimation of the spatial transformation. Image similarities are computed relative to the estimated intensity models, hence accounting for local changes in image intensities. While the motivating application is studying brain

maturation, the proposed method is general and can be applied to any longitudinal image registration problem with non-uniform appearance change (for example, time-series imaging of contrast agent injection).

Section 3.1 introduces the model-based image similarity measure, sum of squared residuals (SSR). Section 3.2 discusses parameter estimation. Section 3.3 describes the performed experiments and discusses results.

The work presented in this chapter has been published in (Csapo et al., 2012b,a, 2013).

3.1 Model-Based Similarity Measure

Assume we have an image intensity model $\hat{I}(x, t; p)$ which for a parameterization, p , describes the expected intensity values for a given point x at a time t . This model is defined in a spatially fixed target image, I_T . Then, instead of registering a measured image I_i at t_i to a fixed target image I_T , we can register it to the corresponding intensity-adjusted target image $\hat{I}(x, t_i; p)$, effectively removing temporal intensity changes for a good model and a good parameterization, p . Hence,

$$\text{Sim}(I_i \circ \Phi_i^{-1}, I_T) \quad \text{is replaced by} \quad \text{Sim}(I_i \circ \Phi_i^{-1}, \hat{I}(x, t_i; p)),$$

where $\text{Sim}(\cdot, \cdot)$ is any chosen similarity measure (e.g., sum of squared differences (SSD), normalized cross correlation, or mutual information), and Φ_i^{-1} is the map from image I_i to the spatially fixed target space. Since the proposed method aims to create an intensity adjusted model \hat{I} that matches the appearance of the source image, SSD is an appropriate choice for the similarity measure. The new intensity-adjusted SSD similarity measure becomes the sum of squared residual (SSR) model, where the residual is defined as the difference between the predicted and the measured intensity value.

3.1.1 General Local Intensity Model Estimation for SSD

Since SSR is a local image similarity measure, for a given set of N measurement images $\{I_i\}$ at times $\{t_i\}$ we can write the full longitudinal similarity measure as the sum over the individual SSRs, i.e.,

$$SSR(\{I_i\}; p) = \sum_{i=0}^{N-1} \int_{\Omega} (I_i \circ \Phi_i^{-1}(x) - \hat{I}(x, t_i; p))^2 dx, \quad (3.1)$$

where Ω is the image domain of the fixed image. For given spatial transforms Φ_i , Equation (3.1) is simply a least-squares parameter estimation problem given the measurements $\{I_i \circ \Phi_i^{-1}(x)\}$ and the predicted model values $\{\hat{I}(x, t_i; p)\}$. The objective is to minimize Equation (3.1) while, at the same time, estimating the model parameters p . The optimum is found by alternating optimization with respect to the intensity model parameters, p , and the spatial transformations Φ_i to convergence (see Section 3.2). Note that looking at only two images at a time without enforcing some form of temporal continuity would lead to independent registration problems and discontinuous temporal intensity models. However, this potential problem is avoided by using all available images in the longitudinal set to estimate the intensity model parameters.

3.1.2 Logistic Intensity Model with Elastic Deformation

SSR can be combined with any model for intensity change, ranging from a given constant target image (the trivial model) and linear models to nonlinear models that are more closely adapted to the myelination process during neurodevelopment. Since the myelination process exhibits a rapid increase in MR intensity (in T1 weighted images) during early brain development followed by a gradual leveling off (Dobbing and Sands, 1973), nonlinear appearance models are justified. I use a logistic model for the experiments, which is often used in growth studies (Fekedulegn et al., 1999), but also investigate various polynomial models in Section 3.3.2. The logistic model is defined as

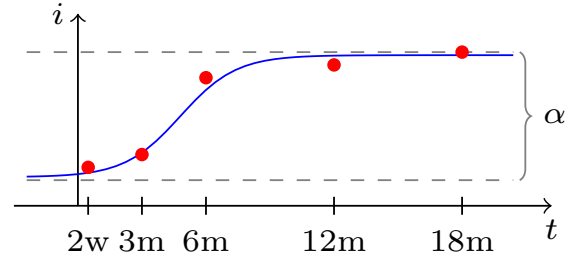


Figure 3.2: Logistic intensity model.

$$\hat{I}(x, t; \alpha(x), \beta(x), k(x)) = \frac{\alpha(x)}{1 + \beta(x)e^{-k(x)t}}, \quad (3.2)$$

where α , β , and k are spatially varying model parameters. We can attribute biological meaning to these parameters, k being the maximum rate of intensity change, α the maximum increase of white matter intensity during myelination, and β is related to the onset time of myelination (see Figure 3.2). Assuming that both unmyelinated and fully myelinated white matter intensities are spatially uniform, α is kept constant as the difference between myelinated (upper asymptote) and unmyelinated (lower asymptote)

white matter intensities. This is a simplifying, but reasonable, assumption since intensity inhomogeneities in unmyelinated or myelinated white matter are small compared to the white matter intensity change due to the myelination process itself (Barkovich et al., 1988).

3.2 Parameter Estimation

Once the parameters for the local intensity models are known, SSR can be used to replace the image similarity measure in any longitudinal registration method. Here, I use an elastic deformation model (Section 3.2.1) and jointly estimate the parameters for the intensity model (Section 3.2.2).

3.2.1 Registration Model

The growth process of the brain not only includes appearance change but complex morphological changes as well, hence the need for a deformable transformation model. To single out plausible deformations, I use an elastic regularizer (Broit, 1981) defined on the displacement field u as

$$S[u] = \int_{\Omega} \frac{\mu}{4} \sum_{j,k=1}^d \underbrace{(\partial_{x_j} u_k + \partial_{x_k} u_j)^2}_{\text{rigidity}} + \frac{\lambda}{2} \underbrace{(\text{div } u)^2}_{\text{volume change}} dx,$$

where μ ($=1$) and λ ($=0$) are the Lamé constants that control elastic behavior and the div is the divergence operator defined as $\nabla \cdot u$, where ∇ is the gradient operator. The behavior of the elastic regularizer might be better understood if we convert the Lamé constants to Poisson's ratio ν ($=0$) and Young's modulus E ($=2$). The given Poisson's ratio allows volume change such that the change in length in one dimension does not cause expansion or contraction in the other dimensions. This is a desirable property in our case, since tissue is both generated and destroyed during development resulting in volume change over time. Young's modulus, on the other hand, describes the elasticity of the tissue and was chosen experimentally to allow large deformations while limiting the amount of folding and discontinuities.

Registration over time then decouples into pairwise registrations between the intensity-adjusted target image \hat{I} and given source images I_i . This is sufficient for our test of the longitudinal image similarity measure, but could easily be combined with a spatiotemporal regularizer, which would then directly couple the transformations between the images of a time-series (instead of only having an indirect coupling through the model-based similarity measure).

3.2.2 Model Parameter Estimation

The intensity model parameters are only estimated within the white matter where image appearance changes non-uniformly over time; for simplicity, gray matter intensity was assumed to stay constant. The methods for obtaining the white matter segmentations for each dataset are described in the corresponding experimental sections. In addition, the effect of white matter segmentation accuracy on the model-based registration is investigated in Section 3.3.4.2.

Instead of estimating the parameters independently for each voxel, spatial regularization was achieved by estimating the medians of the parameters from overlapping local $3 \times 3 \times 3$ neighborhoods (the effect of various neighborhood sizes on registration accuracy is investigated in Section 3.3.4.1).

The algorithm is defined as follows:

- 0) Initialize model \hat{I} parameters to $p = p_0$ (constant intensity model if no prior is given).
- 1) Affinely pre-register images $\{I_i\}$ to $\{\hat{I}(t_i)\}$.
- 2) Estimate model parameters p from the pre-registered images.
- 3) Estimate the appearance of \hat{I} at times $\{t_i\}$, giving $\{\hat{I}(t_i)\}$.
- 4) Estimate displacement fields $\{u_i\}$ by registering images $\{I_i\}$ to $\{\hat{I}(t_i)\}$.
- 5) Estimate p from the registered images $\{I_i \circ u_i\}$.
- 6) Repeat from step 3 until convergence.

The algorithm terminates once the registration energy decreases by less than a given tolerance between subsequent iterations. In the experiments only a few iterations (typically less than 5) were required. If desired, a prior model defined in the target image (a form of intensity model parameter atlas) could easily be integrated into this framework.

3.3 Experimental Results

The validation of the model-based similarity measure requires a set of longitudinal images with known ground truth transformations between the source images and the target images. Three different types of datasets were used for validation:

- *Synthetic 2D* (Figure 3.3)
- *Simulated brain images 3D* (Figure 3.4)
- *Real monkey data 3D* (Figure 3.14)

For the synthetic and simulated datasets, known longitudinal deformations can be added to the generated images in order to simulate growth over time. The deformations are generated from an identity spline transformation (that produces no deformation) with 4×5 (2D synthetic data) and $4 \times 5 \times 4$ (3D simulated data) equally spaced control points for the target image (thus the target image has the same geometry as the original synthetic or simulated image). The deformation for the next time point is then generated by randomly perturbing the spline control points of the previous time point by a small amount. This step is iteratively repeated until a new deformation is generated for each time point. The deformation between any two time points is small, but the cumulative deformation between the first and last time points is considerable (see Figure 3.3).

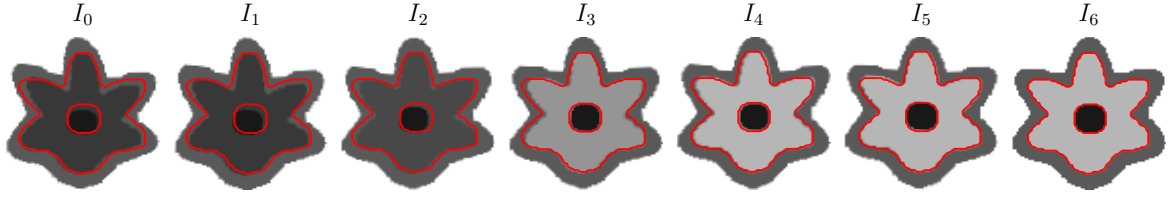


Figure 3.3: Synthetic dataset with logistic white matter intensity change and longitudinal deformation over time. I_0, \dots, I_5 are source images, I_6 is the target image. The outline shows the white matter gray matter boundary of the target image.

Since the ground truth transformations are known, the accuracy of the registration method can be determined by registering each source and target image pair and comparing the resulting transformations to the ground truth transformations. Registration accuracy was determined by computing the distance between the ground truth and the recovered transformation. The root mean squared (RMS) error of the voxel-wise distance within the mask of the target image then yielded the registration error.

For the real datasets, however, the ground truth transformations are not known and cannot be easily determined. Therefore, instead of using a ground truth deformation, manually defined landmarks are used in the source and target images to measure how well they are aligned after registration. For this dataset, registration error was computed as the average Euclidean distance between the target and the registered landmarks.

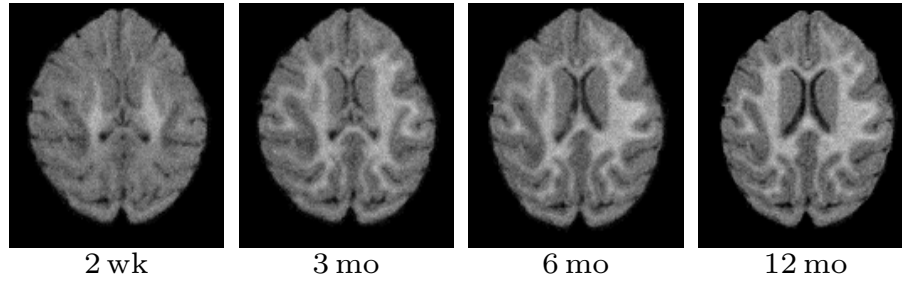


Figure 3.4: Simulated brain images with white matter intensity distributions estimated from the monkey data.

Imaging for the monkey data was performed on a 3T Siemens Trio scanner at the Yerkes Imaging Center, Emory University, with a high-resolution T1-weighted 3D magnetization prepared rapid gradient echo (MPRAGE) sequence ($TR = 3,000\text{ms}$, $TE = 3.33\text{ms}$, flip angle = 8° , matrix = 192×192 , voxel size = 0.6mm^3 , some images were acquired with $TE = 3.51\text{ms}$, voxel size = 0.5mm^3).

The following section describes several experiments that test the proposed similarity measure with progressively more difficult registration problems. Next, additional experiments compare the proposed method to three of the commonly used similarity measures: sum of squared difference (SSD), normalized cross correlation (NCC), and mutual information (MI).

Image registration was performed with the publicly available registration toolbox, FAIR (Modersitzki, 2009).

3.3.1 White Matter Intensity Distributions from Real Data

An important part of the registration experiments is testing the similarity measures on realistic appearance change while knowing the ground truth deformations. To this end, the spatial and temporal intensity changes from the MR images of 9 rhesus monkeys during the first 12 months of life were calculated. The white matter intensity trajectories acquired from the real monkey data were then sampled to generate the synthetic images for 2D validation experiments in Section 3.3.3.

The spatial white matter distributions were calculated for each time point (2 week, 3, 6, 12 month) of the 9 monkeys. The early time points have low gray-white matter contrast, therefore the white matter segmentation of the 12 month image was transferred to the earlier time points (this is often the case for longitudinal studies of neurodevelopment where good tissue segmentation might only be available at the latest time point). For the purpose of a simplified simulation, the white matter intensity change of the

whole brain orthogonal to the posterior-anterior direction was averaged (most of the intensity change is along this direction (Kinney et al., 1994)). Figure 3.5 shows the mean and variation of the white matter intensity profiles from all four time points. Myelination starts in the posterior and central regions of the white matter and continues towards the periphery and, dominantly, towards the anterior and posterior regions. These findings agree with existing studies on myelination (Kinney et al., 1994). Of note is the strong white matter intensity gradient in the early time points due to the varying onset and speed of the myelination process.

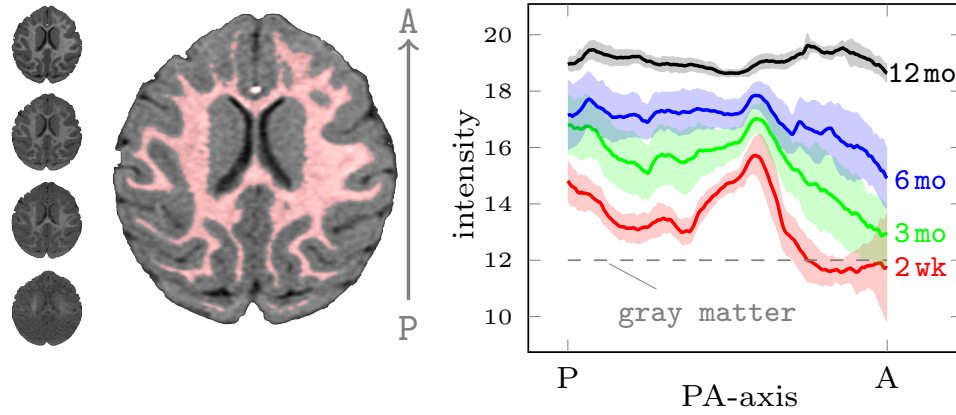


Figure 3.5: Spatiotemporal distribution of white matter intensities in 9 monkeys. A single slice from each time point is shown in order in the left column (2 week at the bottom), and the white matter segmentation (red) at 12 months is shown in the middle. Plotted, for each time point, the mean (line) ± 1 standard deviation (shaded region) of the spatial distribution of the white matter intensities averaged over the whole brain of each monkey orthogonal to the PA direction. The images were affinely registered and intensity normalized based only on the gray matter intensity distributions (gray matter is assumed to stay constant over time). The white matter intensity measurements were sampled to generate synthetic datasets for experimental validation in Section 3.3.3.

3.3.2 Experiment 1: Model Selection

In this experiment I investigated the choice of the parametric intensity model for \hat{I} on registration accuracy, given datasets generated with various intensity models. While the logistic model described in Section 3.1.1 is a reasonable model for the intensity change seen due to myelination, the true intensity model of the data is often unknown and therefore our choice of the intensity model can affect registration accuracy.

Four intensity models were investigated: constant, linear, quadratic, and logistic. Five 128×128 2D synthetic longitudinal image sets were generated with 10 time points each (I_0, \dots, I_9). The synthetic

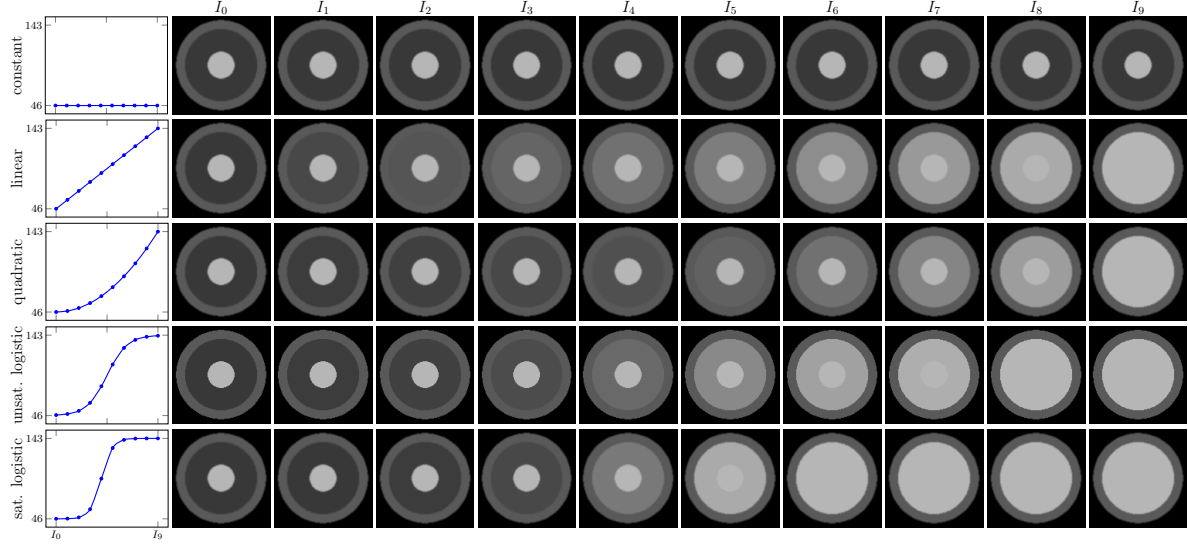


Figure 3.6: Synthetic datasets with 10 time points generated with various intensity models. The outer ring resembling gray matter and the inner ring resembling myelinated white matter stay constant over time. The middle ring representing myelinating white matter changes over time according to the intensity models shown in the first column.

images consist of three concentric rings, the outer ring resembling gray matter, the middle ring white matter going through myelination, and the inner ring myelinated white matter. The outer and inner rings have constant intensity over time (69 and 143 respectively, based on average tissue intensities from the monkey data), while the intensity of the ring representing myelinating white matter was set according to one of five intensity profiles (with unmyelinated white matter = 46 and myelinated white matter = 143): constant, linear, quadratic, unsaturated logistic, and saturated logistic (see Figure 3.6 for the five datasets). The last time point I_9 was designated as the target image and the earlier time points as the source images. The source images were then registered to the target image with deformable elastic registration (FAIR: SSD similarity measure with registration parameter $\alpha = 1000$), using one of the four intensity models for the model image \hat{I} (constant, linear, quadratic, logistic). There is no displacement between the source and target images, thus the ground truth transformation is the identity.

Figure 3.7 shows an extreme case of the model-based registration experiment with a saturated logistic intensity model used for generating the original longitudinal images and a constant model used for the model estimation step. The constant model cannot capture the simulated logistic intensity change within the white matter, therefore considerable deformation is introduced (the correct deformation is the identity).

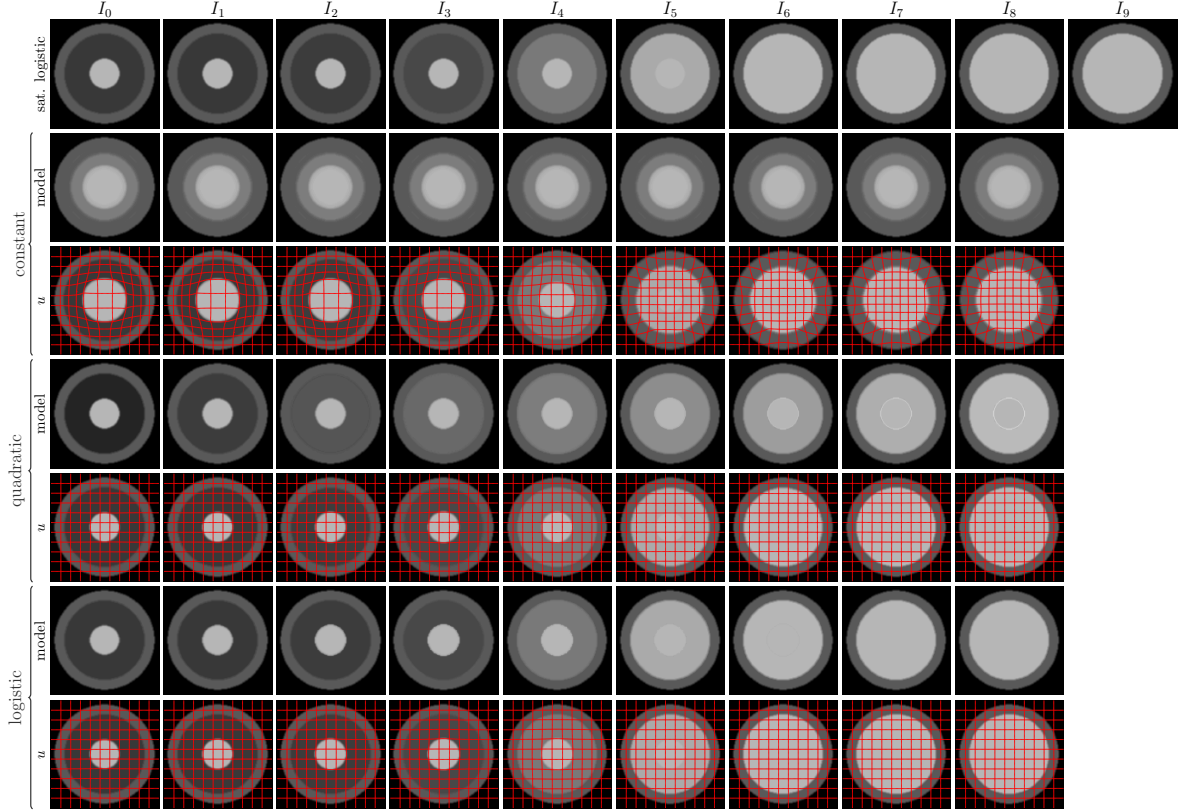


Figure 3.7: The influence of the intensity model on the registration is shown. *Top row*: images generated with the saturated logistic intensity profile. The goal is to register the source images I_0, \dots, I_8 to the target image I_9 with SSR. The following rows show the intensity-adjusted model images $\{\hat{I}(t_i)\}$ and the SSR registration results with the deformation field u overlaid (red grid) for constant, quadratic, and logistic intensity models. Note that the source images are registered to the corresponding intensity-adjusted model images. The correct deformation field is the identity, but the constant model cannot capture the logistic intensity change, therefore erroneous deformations are introduced (warped grid).

Table 3.1: Model selection experiment results. In each row, the data for the experiment was generated by the type of intensity model shown. Each column shows the registration error (in pixels) obtained when using that model in the column for the model-based similarity measure (best values are highlighted).

	constant	linear	quadratic	logistic
constant	0.04	0.04	0.04	0.04
linear	0.68	0.07	0.07	0.13
quadratic	0.60	0.10	0.05	0.16
logistic (unsaturated)	1.63	0.10	0.09	0.12
logistic (saturated)	2.36	0.16	0.16	0.12

Table 3.1 shows the registration errors for all 20 combinations between the five different intensity profiles used to generate the longitudinal images and four model types used for the intensity model estimation. Each row shows the registration error for one of the five generated datasets (lowest errors for each set are highlighted). The columns show the model used for estimating the intensity change over time for \hat{I} . The results show that the quadratic model is a good choice if the underlying true model is polynomial or the logistic model is not saturated; however, the logistic model is necessary when the true model is logistic and the time points are far enough to saturate the model.

3.3.3 Experiment 2: Synthetic Data

In this experiment, I created sets of 64×64 2D synthetic images (based on the Internet Brain Segmentation Repository (IBSR, 2007) synthetic dataset). Each set consisted of 11 time points (I_i , $i = 0, \dots, 10$). I_0 was designated as the target image and all subsequent time points as the source images. The gray matter intensities of all 11 images were fixed ($I_i^{\text{gm}} = 80$). For the source images, I_1, \dots, I_{10} , I introduced two types of white matter appearance change:

- i) Spatially uniform white matter appearance change over time, starting as dark (unmyelinated) white matter ($I_1^{\text{wm}} = 20$) and gradually brightening (myelinated) white matter ($I_{10}^{\text{wm}} = 180$), resulting in linear contrast inversion between gray and white matter. The target white matter intensity was set to 100.
- ii) White matter intensity gradient along the posterior-anterior direction with increasing gradient magnitude over time. The target image had uniform white matter ($I_0^{\text{wm}} = 50$). For the source images the intensity gradient magnitude increased from 1 to 7 intensity units per pixel (giving

$I_1^{\text{wm}} = \{50, \dots, 70\}$ up to $I_{10}^{\text{wm}} = \{50, \dots, 200\}$). These gradients are of similar magnitude, as observed in the real monkey data (see Figure 3.5).

I tested the similarity measures for two types of transformation models: affine and deformable with elastic regularization. Figure 3.8 shows the experimental setup with the deformable transformation model (for the affine registration experiments Φ_i was an affine transform; for the deformable registration experiment Φ_i was a longitudinal spline deformation with 20 control points). The aim of the experiment was to recover the ground truth inverse deformation, Φ_i^{-1} , by registering the 10 source images to I_0 (giving $\hat{\Phi}_i^{-1}$) with each of the four similarity measures (SSD, NCC, MI, SSR). I repeated each experiment 100 times for each transformation model with different random deformations, giving a total of 16 000 registrations (2 white matter change \times 2 transformation model \times 10 source image \times 4 measure \times 100 experiment). Significance was calculated with Welch's t -test (assuming normal distributions, but unequal variances) at a significance level of $\alpha = 0.01$.

Next, I describe the results of the experiments for each transformation model.

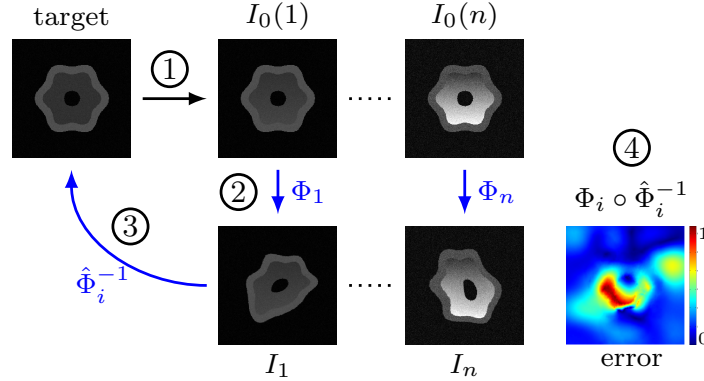


Figure 3.8: Experimental setup: 1) Increasing white matter intensity gradient is added to the target, I_0 . 2) Adding known random longitudinal deformations yields the source images, 3) which are registered back to the target. 4) Registration error is calculated from the known (Φ_i) and recovered ($\hat{\Phi}_i^{-1}$) transformations.

3.3.3.1 Affine transformation model

Affine registration is often appropriate for images from the same adult subject. In our case, it is only a preprocessing step to roughly align the images before a more flexible, deformable registration. Nevertheless, the initial alignment can greatly affect the initial model estimation and the subsequent

deformable solution. Therefore, I first investigate the sensitivity of affine registration to white matter appearance changes separately from deformable registration.

Figure 3.9 shows the results for registering I_1 through I_{10} to the target image I_0 from multiple sets ($n = 100$, giving 1000 pair-wise registrations for each similarity measure) of longitudinal images with both uniform and gradient spatial white matter intensity profiles.

With uniform white matter, all four measures performed well when the contrast of the source image was close to the contrast of the target image (near 0 white matter intensity difference in the first plot of the median root means squared registration error). The results for the gradient white matter profiles show that the performance of both SSD and NCC declined as the gradient magnitude increased, while MI and SSR aligned the images well even with the strongest gradient. Overall, SSR significantly outperformed NCC and MI but not SSD; however, the differences between the overall registration errors are on the order of 0.001 voxels for SSD, MI, and SSR (see Table 1a. in Figure 3.9).

The experiments suggest that affine registration can be reliably achieved by SSD, MI or SSR, but for simplicity MI should be used if affine alignment is the only objective.

3.3.3.2 Deformable registration

Similarly to the affine experiment, Figure 3.10 shows the error plots for deformable registrations in the presence of white matter intensity change. For uniform white matter, SSD again produced small registration errors when the contrast difference was small, but fared worse than MI and SSR in the presence of large intensity differences between the target and the source images. SSR performed slightly better than MI for all time points.

The setup with deformable registration and white matter gradient resembles the real problem closely and therefore is the most relevant. Here, SSD and NCC introduced considerable registration errors with increasing gradient magnitude. The registration error of MI remained under 2 voxels (mean = 1.62 ± 0.45), while SSR led to significantly less error (mean = 1.25 ± 0.35) for all time points.

3.3.4 Experiment 3: Simulated Brain Data

The next set of experiments used simulated 3D brain images with white matter intensity distributions based on the monkey data. The images were preprocessed as described in Section 3.3.1. First, I estimated

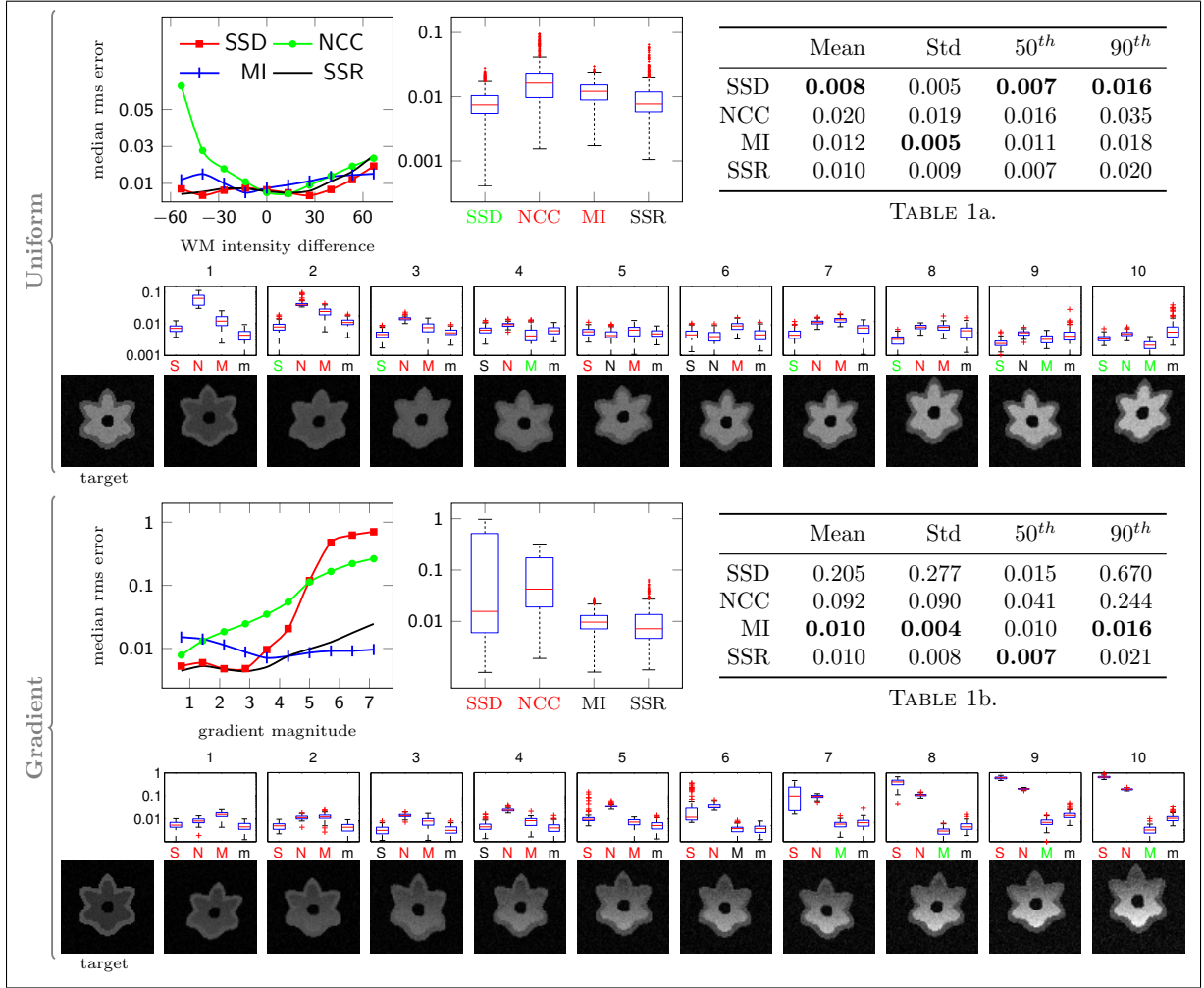


Figure 3.9: Results for Experiment 1 with affine transformation, uniform and gradient white matter intensity change. For uniform white matter, the line plot shows the median RMS error vs. the white matter intensity difference between the source and the target images ($I_i^{\text{wm}} - I_0^{\text{wm}}$) for each time point (0 means the images have the same contrast). For the gradient white matter, the x-axis of the line plot is the magnitude of the gradient. The boxplots and the tables summarize the aggregate results over all time points (the box is the 25th and 75th percentile, the red line is the medium, the whiskers are $1.5 \times$ interquartile range, and the red marks are outliers). The small boxplots show results for each time point (S, N, M, and m are SSD, NCC, MI, and SSR respectively). For each boxplot, the x-label is highlighted in red/green if SSR performed significantly better/worse than that particular measure. The row of images shows the target and source images for a single trial. Note that all boxplots and the bottom line plot have log y scales.

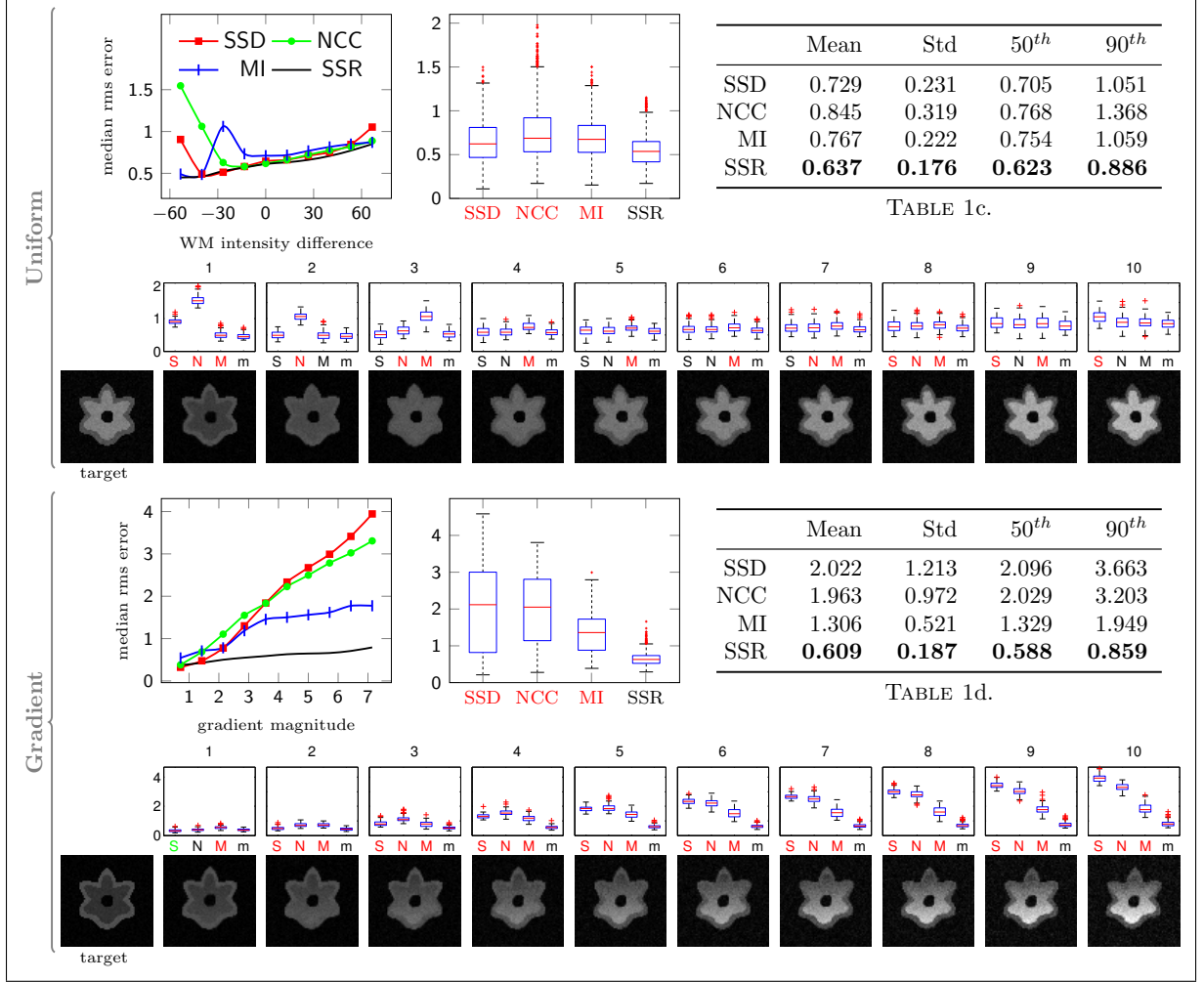


Figure 3.10: Experiment 1 results with deformable transformation. The graphs are set up similarly as in Figure 3.9 except all plots have linear y scales. The last setup with deformable transformation model and gradient white matter intensity is the most challenging and relevant to the real world problem.

the voxel-wise longitudinal intensity model within the white matter from the four time points of a single subject, using SSR with a logistic intensity model. The estimated intensity model was then applied to each white matter voxel of the 12 month image to generate four different time points I_0, \dots, I_3 with the same geometry as the 12 month image, but with different white matter intensity distributions. The time points were random perturbations of the original image time points (0.5, 3, 6, and 12 months) with normal distribution $\mathcal{N}(\mu = 0, \sigma^2 = 1 \text{ week})$. The final source images were obtained by adding known longitudinal random deformations to the generated images I_0, \dots, I_2 (see Figure 3.4). 100 sets of longitudinal images were generated for the following experiments with different random time perturbations and spatial deformations.

3.3.4.1 Smoothing kernel size

In this experiment I investigated the effect of the smoothing kernel size on the registration accuracy of SSR. In addition to no smoothing, four isotropic median kernels with sizes 3, 5, 7, and 9 voxels were used to smooth the model parameters.

The size of the smoothing kernel had no significant influence on the global registration error (see Figure 3.12), even though larger kernels tend to over smooth the salient features of the model, such as the boundary between the unmyelinated and myelinated white matter. No smoothing, on the other hand, allows areas of poor model estimation, due to misregistration between the time points, to remain in the intensity model. Most noticeably, initial misregistration near the gray matter white matter boundary can lead to a boundary shift.

Next, I illustrate this boundary shift with a 2D synthetic longitudinal dataset with a small misalignment between the time points shown in Figure 3.3. Assuming that this is the best initial alignment between the time points, the top row of Figure 3.11 shows the model images estimated from the dataset at time t_2 with three different kernel sizes; the bottom row shows the registration results between the source (I_2) and model images ($\hat{I}(t_2)$). As the kernel size increases, the model better approximates the true tissue intensities near the boundary and the registration error (boundary shift) decreases. While a large smoothing kernel is advantageous near the boundary, a smaller kernel is less likely to smooth out salient features within the white matter. Thus smoothing with an adaptive kernel size inversely proportional to the distance from the white matter boundary might be the most advantageous.

3.3.4.2 White matter segmentation

Since the intensity change over time occurs in the white matter, the current algorithm estimates the model parameters only within the white matter segmentation. Reliable white matter segmentations, however, may not be available. In order to test the registration accuracy with various quality white matter segmentations, I registered each of the 100 longitudinal sets of the 3D simulated brain images using SSR with 7 white matter masks with varying quality, shown in Figure 3.13 (from an empty mask (M_{-3}) through the accurate (M_0) white matter mask and a full brain mask). The masks under/over estimating the white matter were generated by eroding/dilating the accurate white matter mask (M_0) of the 12 month image. Figure 3.12 shows the registration accuracy for each of the masks. The registration error

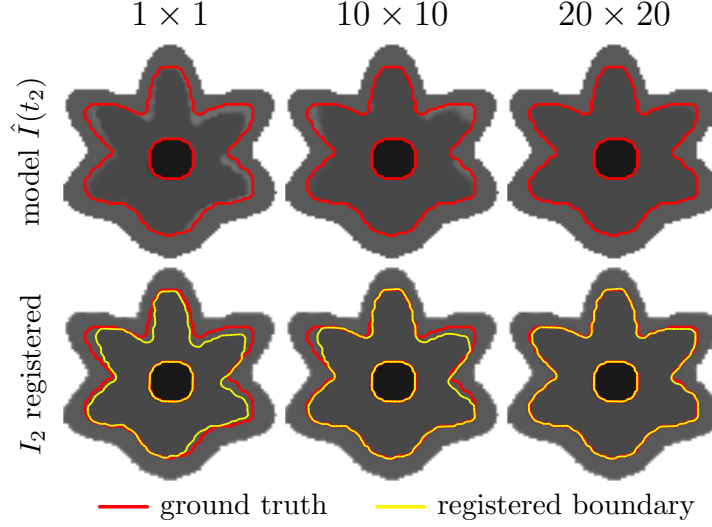


Figure 3.11: The effect of various median smoothing kernel sizes on the intensity model estimation and the subsequent registration (dataset is shown in Figure 3.3). *Top row*: shows the estimated model from the misaligned synthetic longitudinal dataset with 1×1 , 10×10 , and 20×20 voxel kernels (the red outline is the correct tissue boundary). *Bottom row*: shows the results of elastically registering time point I_2 to the models $\hat{I}(t_2)$ in the top row (the yellow outline is the boundary after the registration).

is lowest when the white matter mask is accurate or slightly underestimated, therefore accurate white matter segmentation is necessary.

3.3.5 Experiment 4: Monkey Data

I compared the model-based similarity measure to mutual information (MI) on sets of longitudinal magnetic resonance images of 9 monkeys, each with 4 time points (2 week, 3, 6, and 12 month). Each time point was affinely pre-registered to an atlas generated from images at the same time point (the atlas images for the four time points were affinely registered) and intensity normalized so that the gray matter intensity distributions matched after normalization (gray matter intensity generally stays constant over time). The tissue segmentation was obtained at the last time point with an atlas-based segmentation method (Styner et al., 2008).

I registered 3D images of the three early time points $I_{2\text{wk}}$, $I_{3\text{mo}}$, $I_{6\text{mo}}$ to the target image $I_{12\text{mo}}$ with an elastic registration method. Since the ground truth deformations were not known, manually selected landmarks (Figure 3.14) identified corresponding regions of the brain at the different time points (10-20 landmarks in a single slice for each of the 4 time points in all 9 subjects; the landmarks were picked

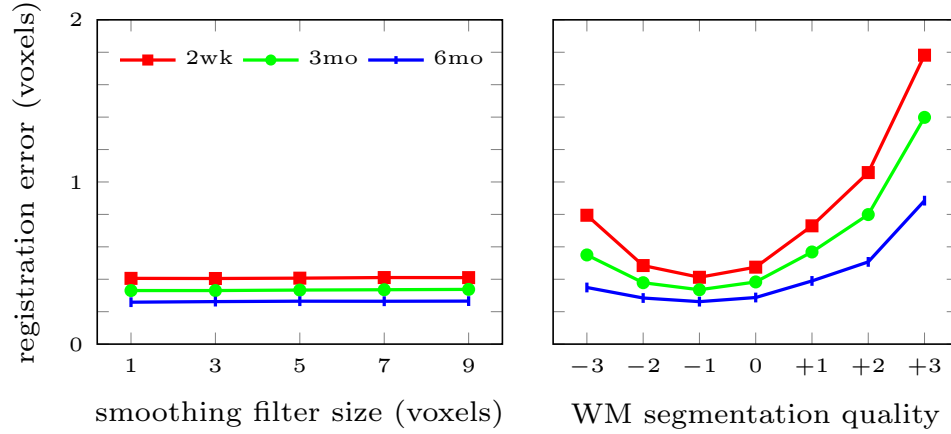


Figure 3.12: Results for SSR registration with different median smoothing kernel sizes (left) and varying quality white matter segmentations (right; x-axis shows the amount of erosion (-) or dilation (+) applied to the accurate (0) white matter mask).

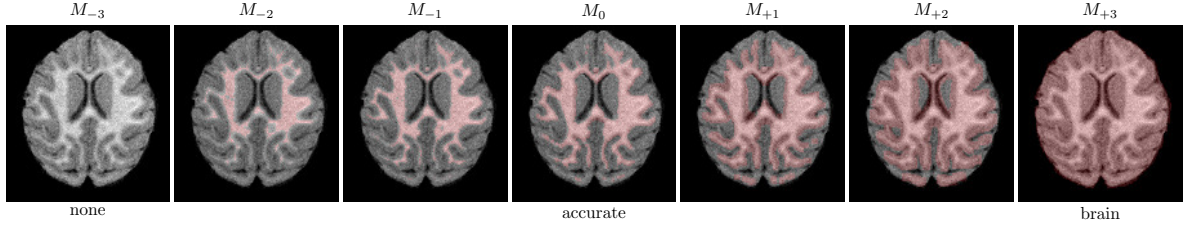


Figure 3.13: White matter segmentations used to investigate the influence of segmentation accuracy on SSR registration (erosion (M_{-}) and dilation (M_{+}) are applied to the accurate (M_0) segmentation).

based on geometric considerations). The distance between transformed and target landmarks yielded registration accuracy. Figure 3.15 shows the experimental setup.

Note that for the model-based method the target image is not I_{12mo} , but the model $\hat{I}_{12mo}(t)$ estimated at time t of the source image. Here, the target image is I_{12mo} as white matter segmentation is easily obtained given the good gray matter white matter contrast, but other time points could be used.

With MI, the registration method accounts for both the non-uniform white matter appearance change and the morphological changes due to growth through large local deformations. This is not desirable since the registration method should only account for the morphological changes. These local deformations are especially apparent for registrations between I_{2wk} (and to a lesser extent I_{3mo}) and the target I_{12mo} and suggest large local morphological changes contradictory to normal brain development (Dobbing and Sands, 1973). The landmark mismatch results (Figure 3.16) show that both mutual information and

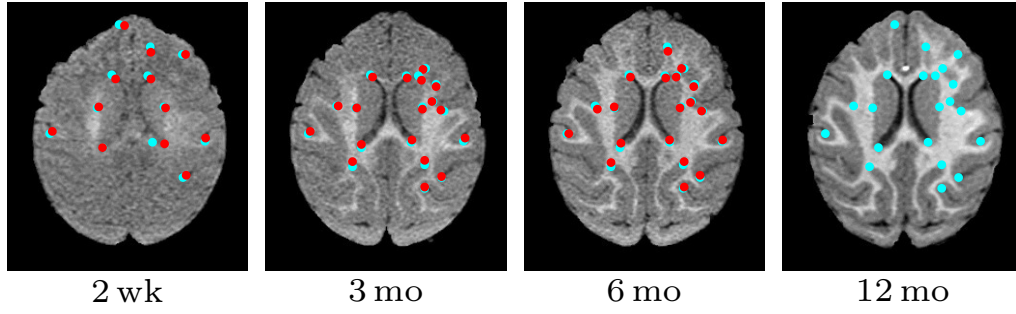


Figure 3.14: Corresponding target (cyan) and source (red) landmarks for a single subject.

Table 3.2: Landmark registration error (in voxels) between target $I_{12\text{mo}}$ and source images $I_{2\text{wk}}$, $I_{3\text{mo}}$, $I_{6\text{mo}}$ (significance level is $\alpha = 0.05$; significant results are highlighted).

	$I_{2\text{wk}}$				$I_{3\text{mo}}$				$I_{6\text{mo}}$			
	<i>mean</i>	<i>std</i>	50 th	90 th	<i>mean</i>	<i>std</i>	50 th	90 th	<i>mean</i>	<i>std</i>	50 th	90 th
MI	1.76	1.09	1.60	3.22	1.07	0.77	0.84	2.04	0.66	0.46	0.56	1.22
SSR	1.15	0.84	0.93	2.24	0.74	0.57	0.54	1.66	0.61	0.39	0.50	1.18

the model-based approach perform well in the absence of large intensity non-uniformity; however, SSR consistently introduces smaller erroneous deformations than MI.

Table 3.2 shows the aggregate results of the landmark mismatch calculations for both methods. The model-based approach can account for appearance change by adjusting the intensity of the model image (see the estimated model images in Figure 3.15) and therefore is most beneficial when the change in appearance between the source and target image is large ($I_{2\text{wk}}$, $I_{3\text{mo}}$).

I also compared 1st and 2nd degree polynomial intensity models to the logistic model and found no significant difference. This agrees with our findings from Section 3.3.2, where with only 4 time points even the 1st degree model can reasonably estimate the local appearance changes. However, similarly to the earlier model selection experiment, the logistic model should outperform the simpler models in larger studies with more time points or when the model appearance needs to be extrapolated (e.g., if new images are acquired later in a longitudinal study after the previous time points have been aligned).

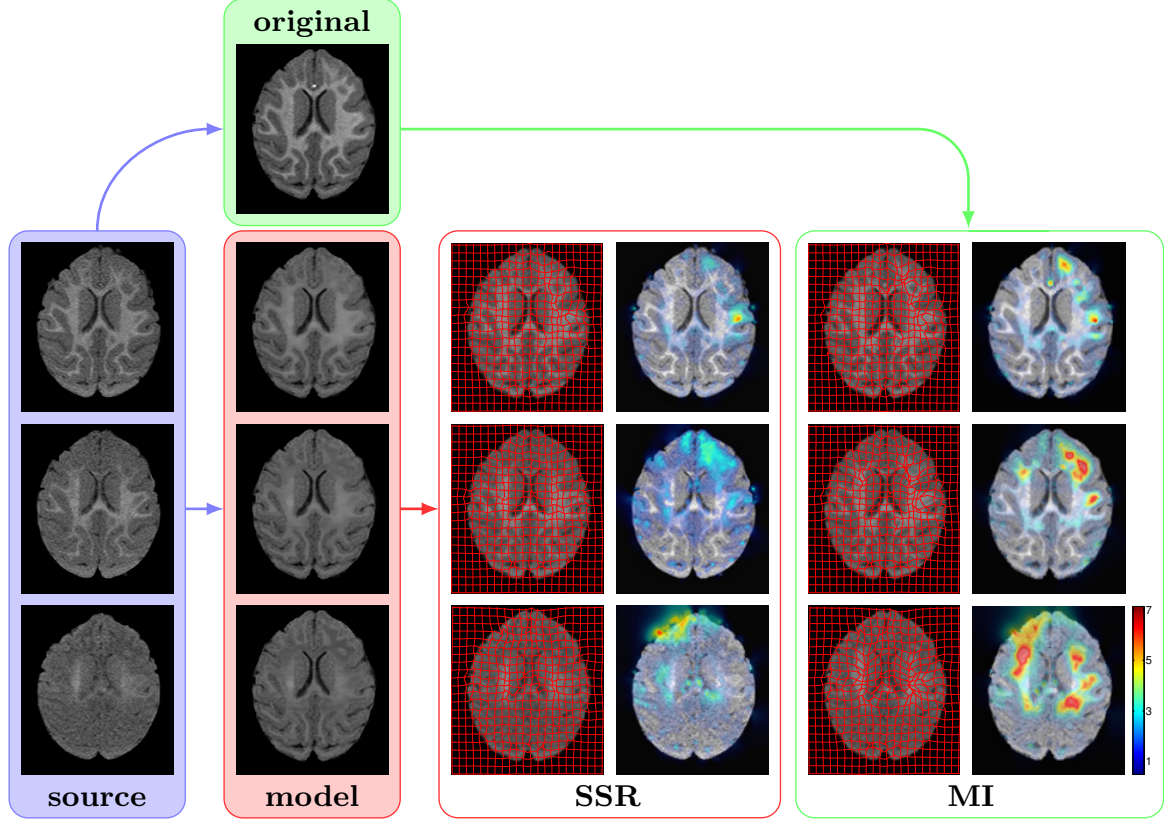


Figure 3.15: Experimental setup for a single subject. To test MI, the source images (blue; from bottom: I_{2wk} , I_{3mo} , I_{6mo}) are registered to the latest time point I_{12mo} (green). The resulting deformation field and the magnitude of the deformations (in pixels) is shown in the right panel. For SSR, the source images are registered to the model (red) that estimates the appearance of I_{12mo} at the corresponding time of each source image (results in middle panel). The results are evaluated using manually chosen landmarks in the target and source images (not shown here).

3.4 Conclusions

I proposed a new model-based similarity measure which allows the deformable registration of longitudinal images with appearance change. This method can account for the intensity change over time and enables the registration method to recover the deformation due only to changes in morphology. I compared the model-based approach to mutual information and demonstrated that it can achieve higher accuracy than mutual information in cases when there is a large appearance change between source and target images. I used a logistic model of intensity change and an elastic deformation model; however, the formulation is general and can be used with any other appearance or deformation model. In the following chapter, the proposed method is used to construct an atlas of brain maturation.

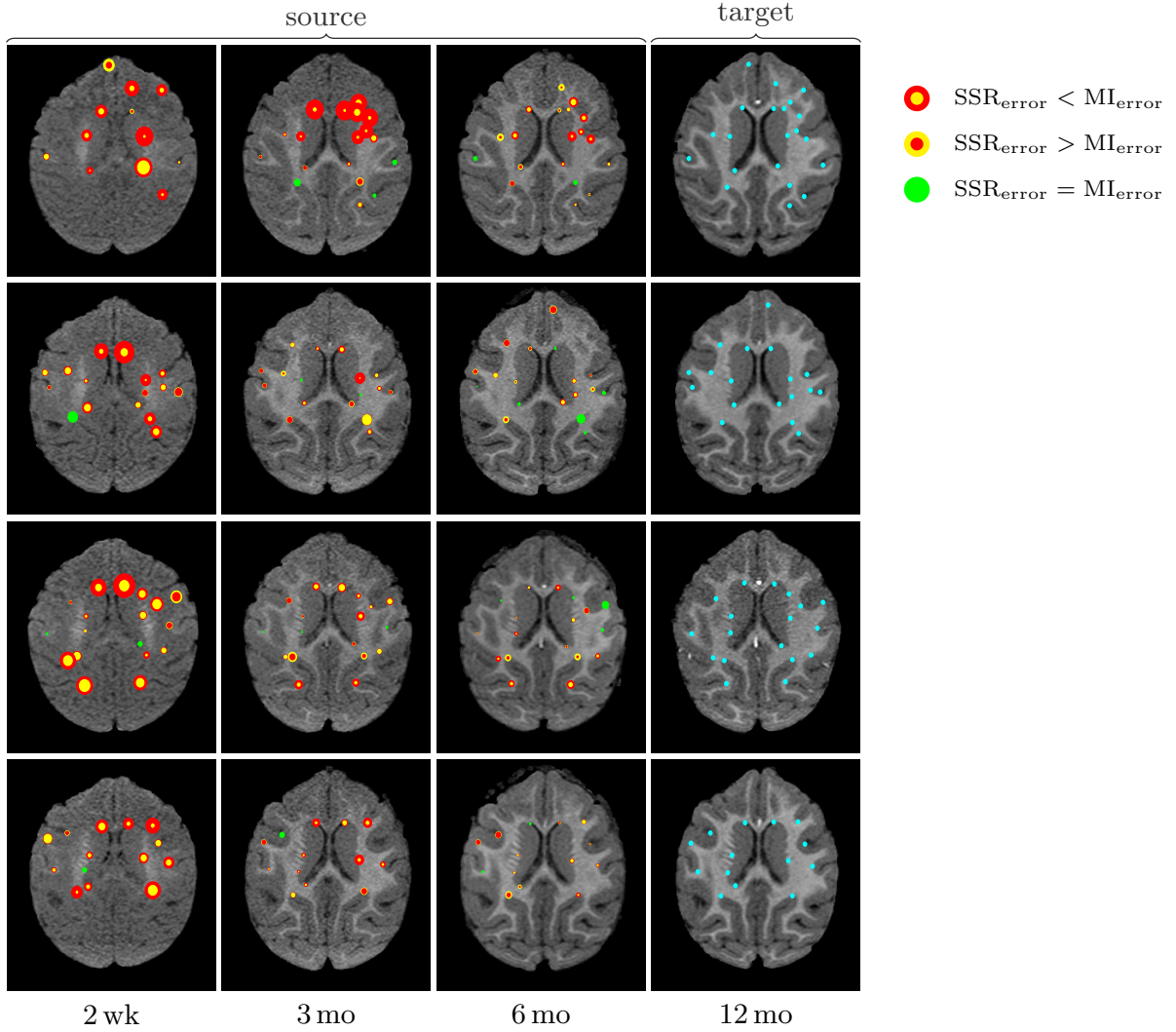


Figure 3.16: Landmark distance mismatch. Each row shows a single subject. The last column shows the target images and landmarks (cyan). Columns 1-3 are the source images: each target-source landmark pair is marked as a circle (*red*: mutual information; *yellow*: SSR) with size proportional to the distance (mismatch) after registration between the landmark pair (the smaller circle is always on top). That is, the size of the circles is proportional to registration accuracy (smaller is more accurate) in that particular location. The results show that for most landmarks the error was smaller using SSR than MI (the size of the yellow circle representing SSR registration error is smaller than the size of the red circle representing MI registration error for the same landmark).

CHAPTER 4

Quantitative MRI Atlas of Postnatal Rhesus Macaque Brain Maturation

4.1 Introduction

The maturation of the mammalian brain relies on a tightly coordinated sequence of cell proliferation, cell positioning, axonal growth and pruning, and the elaboration of the myelin sheath of the axons (myelination). The spatial and temporal trajectories of brain maturation and cognitive development are driven by genetics, environmental factors, and learning, and vary considerably between individuals (Knickmeyer et al., 2008). While most mammalian organ systems fully develop in utero, the brain continues to develop and acquire new functionality well after birth. The resulting plasticity of the immature brain enables organisms to rapidly adapt to their environment (Zilles, 1992), but it also leaves the brain vulnerable to developmental insults (McEwen, 1994). A variety of toxic, infectious, vascular, traumatic, and psychological insults have been shown to alter the normal trajectory of brain development (Riley et al., 2011; Rees and Inder, 2005; Morton et al., 2017; Friess et al., 2007; Lupien et al., 2009). In addition to these early postnatal insults, there has been a growing interest in studying normal brain maturation and neurodevelopmental disorders, such as autism spectrum disorders and schizophrenia, with the aid of non-invasive medical imaging technologies (Toga et al., 2006).

In humans, overall brain size nearly doubles during the first year of neonatal development and reaches 80-90% of its adult volume by age 2 (Knickmeyer et al., 2008). This rapid increase in volume does not affect all brain structures equally. Gray matter, the cerebellum, and the lateral ventricles contribute the majority of the brain volume increase during the first year of development, while white matter volume increases only modestly (Knickmeyer et al., 2008). In addition to morphological changes, the myelination of white matter proceeds rapidly during this same period, leading to non-uniform spatial and temporal changes in the magnetic resonance (MR) appearance of white matter throughout the brain (Sampaio and Truwit, 2001). In fact, myelination is the primary driver of MR signal changes that first appear in T1-weighted images and later in T2-weighted images as the composition of the myelin sheaths

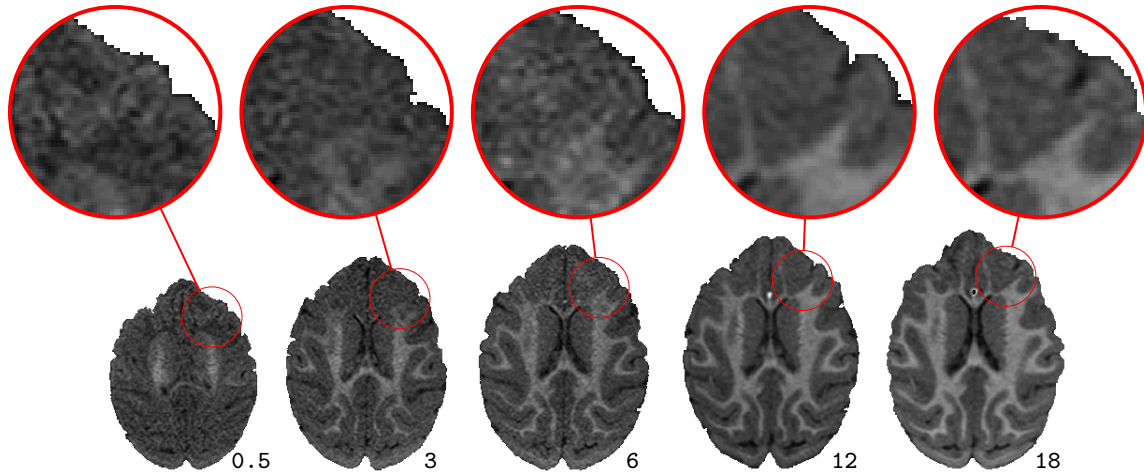


Figure 4.1: Axial slices of MR brain images of monkey at ages 2 weeks, 3, 6, 12, and 18 months. White matter appearance changes non-uniformly as axons are myelinated during brain development.

changes (Barkovich et al., 1988). The combined morphological and appearance changes (see Figure 4.1) make longitudinal analysis of brain development a challenging problem. Longitudinal analysis has to be flexible enough to allow for the large non-uniform morphological and appearance changes, while at the same time provide temporally smooth solutions.

Animal models, ranging from rodent to non-human primate, have been widely used in comparative human brain development studies. Non-human primate models have been especially important, due to their phylogenetic proximity to humans and their similar brain architecture, prolonged gestational period, developmental trajectories, complex cognitive function, and social behavior (Capitanio and Emborg, 2008). While chimpanzees are our closest non-human relatives, practical considerations have led to the use of more distantly related primate species as the predominant research subjects (Lacreuse and Herndon, 2008). In fact, an old world monkey species, the rhesus macaque, is the most widely used non-human primate model (Carlsson et al., 2004) and it has even been the subject of a series of infamous landmark studies that have changed how we approach child-rearing to this day (Harlow et al., 1971).

Despite the increasing quantity and quality of the imaging data, distinguishing normal and pathological changes in a population remains a challenge and requires the availability of normative data. One commonly used technique for analysis is aggregating imaging data into a common brain atlas. Mature brain atlases have been widely used for aiding registration (Serag et al., 2012) and segmentation (Fischl et al., 2002), but atlases of brain maturation have been less prominent. However, accurate characterization of spatial and temporal patterns of maturation can be useful in a variety of imaging tasks, including

finding the developmental age of brain regions (Dean et al., 2015), describing atypical development (Just et al., 2012), or aiding registration (the topic of Chapter 5). While longitudinal atlases for morphological changes have been developed, there are few atlases that capture the longitudinal appearance change of the developing brain, especially atlases that target prenatal and early postnatal brain development – periods when image registration and segmentation are especially difficult. This is not surprising, given the challenging nature of longitudinal imaging in utero and during early postnatal development. Existing brain atlases targeting this period have focused on bulk measures, such as volumetric changes of segmented regions (Gilmore et al., 2011), or on morphological changes only. However, a number of atlases summarize other quantitative measures of brain maturation (most often diffusion characteristics hinting at the underlying structural organization) for small mammals (Zhang et al., 2005; Huang et al., 2008; Chuang et al., 2011) and primates (Hikishima et al., 2013), including humans (Sadeghi et al., 2013; Dean et al., 2014, 2015; Makropoulos et al., 2016). Of these atlases, most are using built cross-sectional images and only Dean et al. provides a voxel-wise longitudinal estimation of diffusion characteristics (Dean et al., 2015). Even so, out of the 209 human subjects used by Dean et al., more than half have a single time point and only five have four time points (compared to our study with five time points for each subject).

4.2 Estimating the Atlas from a Population

To build the atlas, I made the following choices and assumptions:

1. **Locality of the model.** The model is defined over a white matter mask only as the expected change in gray matter intensity throughout neurodevelopment is negligible compared to the white matter.
2. **Atlas space.** As white/gray-matter contrast is best for a fully matured brain, the atlas is defined on an average atlas image for the latest time point in our dataset – where an automatic white matter segmentation can be reliably obtained. The atlas model parameters are resampled in the anatomical space of each subject through registering the atlas to the latest time point.
3. **Temporal model type.** Ideally, the model should be learned fully from the data. However, given the limited number of subjects typical for most neurodevelopmental studies, I use a logistic model (similarly to the model in Chapter 3) with fixed asymptotes (for minimal and maximal white matter

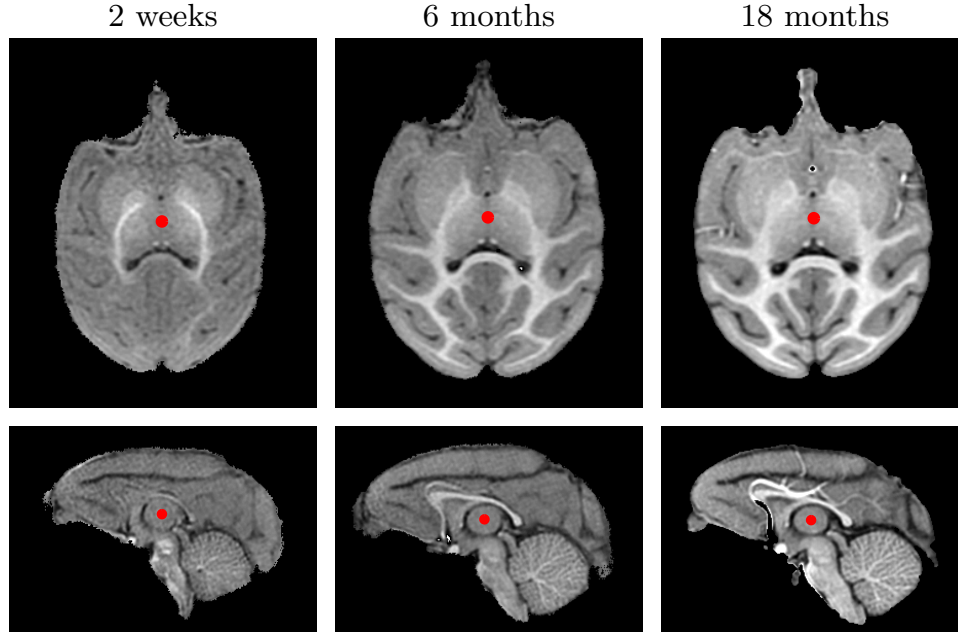


Figure 4.2: Example of an expert-defined anatomical landmark within the same subject (*top*: axial slices; *bottom*: sagittal slices).

intensity). This way the temporal model is parameterized by only two parameters capturing onset and rate of maturation.

4. **Spatial regularization.** In order to provide robust estimates of the model parameters with respect to image noise and small registration errors, spatial regularity is enforced on the estimated group-wise model parameters via a $3 \times 3 \times 3$ median filter.

4.2.1 Monkey Dataset

Both synthetic and real datasets were used for evaluation and atlas-building. The real dataset consists of longitudinal MR images with five time points (scanned at 2 weeks, 3, 6, 12, and 18 months) for 10 normal rhesus macaques acquired at the Yerkes Imaging Center (Emory University, GA). The subjects were scanned on a 3T Siemens Trio scanner at the Yerkes Imaging Center, Emory University, with a high-resolution T1-weighted 3D magnetization prepared rapid gradient echo (MPRAGE) sequence (TR = 3,000ms, TE = 3.33ms, flip angle = 8, matrix = 192×192 , voxel size = 0.6mm^3 , some images were acquired with TE = 3.51ms, voxel size = 0.5mm^3).

The images were inhomogeneity corrected (Tustison et al., 2010) and registered into a standardized atlas space using an affine transformation with a local cross correlation metric (ANTS (Avants et al., 2009)). Skull stripping and tissue segmentation were obtained with an atlas-based segmentation method (Styner et al., 2008). Furthermore, 35 anatomical landmarks were defined by an expert for all 5 time points (see Figure 4.2).

To build the maturation atlas intra-subject elastic deformable registration to the latest time point is performed first using the previously developed longitudinal SSR registration in Chapter 3. Inter-subject registration is then established by registering the oldest time point of each subject to a common atlas space. This establishes correspondences between all subjects for all time points. I thin the white matter mask to avoid model estimation errors for the logistic intensity model near tissue boundaries, due to partial voluming, segmentation errors, or registration errors. For each point in the thinned white matter mask the logistic models are then estimated as follows.

4.2.2 Model Estimation

For the point-wise estimation of logistic curves, I considered (i) a direct fit of a single logistic model to all data points (disregarding their longitudinal nature), (ii) a full longitudinal estimation procedure, and (iii) fitting individual logistic curves for each subject followed by the computation of the median of these logistic curves. Since different subjects of the same age may be at slightly different stages of neurodevelopment, the first two approaches would require a simultaneous estimation of this time-shift to avoid underestimating the maturation rate. I, therefore, chose the latter approach as it is robust to such time-shifts, is simple, and provides a parametric model. I locally compute the median curve over the population, using the approach proposed for calculating the functional boxplot (Sun and Genton, 2011), where I replace all the measured values by the values of their individual logistic model fits. As the median curve will be a curve from the dataset, I thus obtain a median logistic curve. (This is fundamentally different from computing a point-wise median.) The individual logistic models are fit using ordinary least squares¹ $[\hat{\theta}_j = \operatorname{argmin}_{\theta} \sum_i (I_j(t_i) - \operatorname{logistic}(t_i, \theta))^2]$, where $I_j(t_i)$ is the intensity at time point t_i

¹This could be easily replaced by a weighted least squares model approximating, for example, a Rician noise model (Salvador et al., 2004).

for subject j and θ denotes the coefficients for the logistic model. The logistic model is defined as

$$\text{logistic}(\mathbf{x}, t; \alpha, \beta(\mathbf{x}), k(\mathbf{x})) = \frac{\alpha}{1 + e^{-k(\mathbf{x})(t - \beta(\mathbf{x}))}}, \quad (4.1)$$

where α is a global parameter (intensity change between unmyelinated and myelinated white matter), β (onset: time of maximum rate of intensity change) and k (maximum rate of intensity change) are spatially varying model parameters (see Figure 4.3). I further compute the variance of the actual measured values with respect to the median logistic model ($\bar{\theta}$) at the ages of interest [$\hat{\sigma}^2(t_i) = \frac{1}{N(t_i)} \sum_j (I_j(t_i) - \text{logistic}(t_i, \bar{\theta}))^2$], where $N(t_i)$ denotes the number of measurements at time point t_i . This allows us to introduce local weights into the registration method described in Chapter 5.

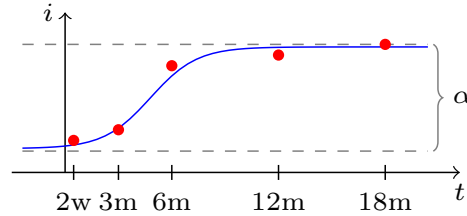


Figure 4.3: Logistic intensity model.

As maturation is expected to be locally smooth, I smoothly extend the estimated parameters of the logistic model to the full white matter mask. Figure 4.4 shows sample slices with the color-coded coefficients for onset and maturation rate.

Shortcomings of the model estimation. Time-shift uncertainties are only implicitly accounted for in the model, as the computed variances will be a combination between image noise, registration errors, and time-shifts of the maturation trajectories. An improved estimation procedure could also estimate the time-shifts, however at the cost of greater model complexity. The observations indicate that these shifts (if present) are relatively minor and therefore I chose not to explicitly model them.

4.2.3 Comparison to Expected Myelination Pattern

The myelination of the central nervous system occurs in a complex, but predictable, spatial and temporal sequence. The myelination pattern has been studied using both histology (Kinney et al., 1994) and, more recently, MR imaging (Sampaio and Truwit, 2001). Here, I compare the spatial and

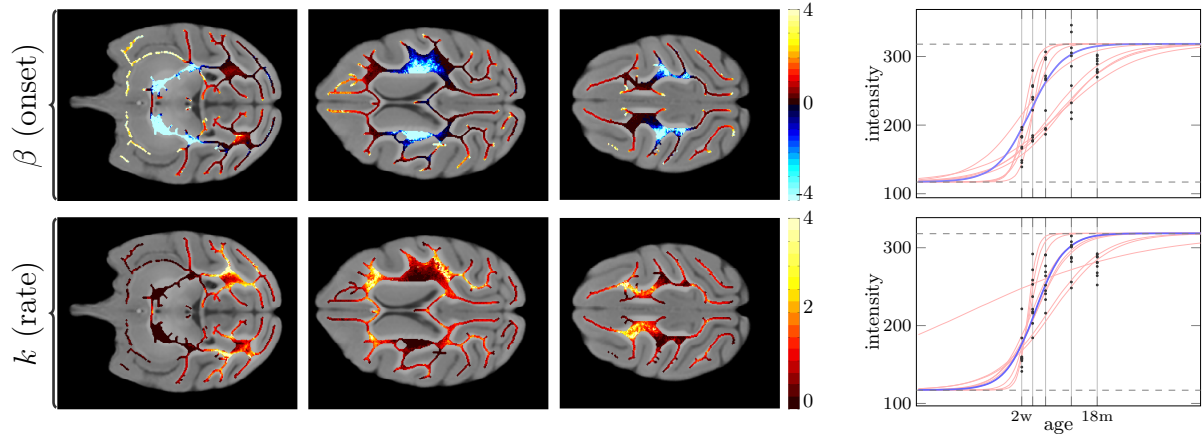


Figure 4.4: Estimated onset (in months) and rate of maturation overlaid on three axial slices of the structural atlas (*columns 1-3*: inferior to superior). Note that this is the initial estimate in the thinned white matter mask. The parameters follow an expected pattern of maturation. The plots show the individual (*red*) and median (*blue*) logistic curves and the intensity values (*black dots*) for the ten subjects for two different voxels.

chronological pattern of the maturation atlas of the macaque model to the patterns defined in previous histochemical and MR studies of myelination in humans.

Overall, the maturation atlas captures the expected maturation patterns, with areas deeper in the brain either reaching their matured intensity early or already being fully matured at two weeks of age (first time point). On a finer scale, several complex rules govern the spatial and temporal sequences of myelination as described in (Kinney et al., 1994):

1. **Myelination proceeds from the center to the periphery:** proximal pathways myelinate earlier and faster than distal ones.
2. **Myelination proceeds from back to front:** occipital poles myelinate before frontotemporal poles.
3. **Some structures myelinate early on:** at birth, the following cerebral structures are partially myelinated: cerebral peduncle, internal capsule, central corona radiata.

These myelination patterns can be seen on the maturation atlas in Figure 4.4. Parts of proximal structures, such as the internal capsule and corona radiata, are myelinated by birth. Myelination then proceeds distally with the posterior poles myelinating before the anterior poles of the frontal lobes. Note that since the atlas only captures neonatal maturation, the rate of the myelination is close to zero in regions already myelinated by birth.

4.3 Conclusions

The ability of MR imaging to reveal not only the structural organization of the brain, but the state of biological processes that drive brain maturation, provides a way to summarize the temporal and spatial nature of those maturation processes. One such process, myelination, reveals the developmental state of the white matter and it is the primary driver of appearance change in structural MR images. In this chapter, I built a longitudinal atlas of brain maturation based on the myelination driven MR signal changes of the neonatal rhesus macaque brain. The atlas shows patterns of brain maturation similar to patterns derived from previous histological and MR studies. This maturation atlas is unique, as it is based on parametric characterization of longitudinal white matter MR intensities using five time points per individual subject. The atlas can be useful for aiding image registration and segmentation methods during this early period of brain development when considerable morphological and appearance changes make analysis difficult.

CHAPTER 5

Registration of Developmental Image Sequences with Missing Data

As described in the previous chapters, standard similarity measures (such as mutual information or cross correlation) are not appropriate for registering images with both morphological and appearance changes and may lead to incorrect estimates of deformation that regularization alone cannot fully prevent. A way to improve alignment is to introduce meaningful constraints into the registration. In Chapter 3, white matter appearance over time is estimated locally and then used to create a predicted target image for registration at a given time point. By restricting intensities to conform to a parametric model, an improved registration performance can be obtained. While an improvement over the standard registration model, the proposed model is fully data-driven and parameter-estimation may therefore become unreliable if the number of images in the longitudinal dataset is low. Furthermore, estimation of the model parameters is not possible if the number of available images is lower than the number of unknowns in the parametric intensity model.

The maturation atlas developed in Chapter 4 captures the mean and variation of the model parameters for a normal population. These estimates can be used as a prior for novel datasets with missing or poor quality data. To improve the performance of the parameters estimation in the similarity measure developed in Chapter 3, the maturation atlas is incorporated as a prior to better guide the deformable registration for longitudinal datasets with missing time points. In addition, the prior may also aid the model-based registration of complete datasets when the model cannot be reliably estimated due to corrupted data or poor initial alignment.

Contributions.

- *A method to integrate the longitudinal intensity prior into a deformable registration approach to aid the registration for datasets with missing time points.*

- A *synthetic test case* showing improved alignment for the proposed registration approach over a deformable registration method that includes a longitudinal intensity model without any priors introduced in Chapter 3.
- An *evaluation on a real dataset* showing that the proposed method can achieve comparable registration results to registration with the full longitudinal image sequence, even with missing time points. The results are validated with manually selected landmarks.

5.1 Using the Maturation Information

Given a longitudinal set of images that should be registered the equivalent of the sum of squared difference, intensity difference with respect to a fit logistic model over all images is given as (from Section 3.1.1)

$$SSR(\{I_i\}) = \sum_{i=0}^{n-1} \int_{\Omega} (I(\Phi_i^{-1}(x), t_i) - \hat{I}(x, t_i))^2 dx, \quad (5.1)$$

where Ω is the image domain of the fixed image, \hat{I} is the intensity-adjusted spatially fixed target image, and Φ_i^{-1} is the map from the moving image I to the target image \hat{I} . To make use of the prior information this similarity measure is augmented to

$$SSRP(\{I_i\}) = \sum_{i=0}^{n-1} \int_{\Omega} (I(\Phi_i^{-1}(x), t_i) - \hat{I}(x, t_i))^2 dx + \gamma \int_{\Omega} \int_t \frac{1}{\sigma^2(x, t)} (I_p(x, t) - \hat{I}(x, t))^2 dt dx, \quad (5.2)$$

where I_p is the intensity predicted by the prior model, σ^2 is the variance of the image intensity values with respect to the model intensity (see Chapter 4 for more details on the model estimation), and $\gamma > 0$ is a chosen balancing constant. Hence, given a current estimate of the deformation, we can compute an estimate for the model \hat{I} locally by minimizing Equation (5.2) with respect to the parameters $\hat{\theta}$ of \hat{I} . The remainder of the procedure stays unchanged.

5.2 Experimental Results

To assess the utility of incorporating the white matter intensity prior into the longitudinal similarity measure SSR I i) validated the proposed method on a synthetic 2D dataset, ii) for the real 3D monkey

data (see detailed description of the data in Section 4.2.1), showed that affine registration alone is not sufficient to align developmental image sequences, and iii) tested the utility of the prior for incomplete real datasets.

5.2.1 Registering Synthetic 2D Dataset

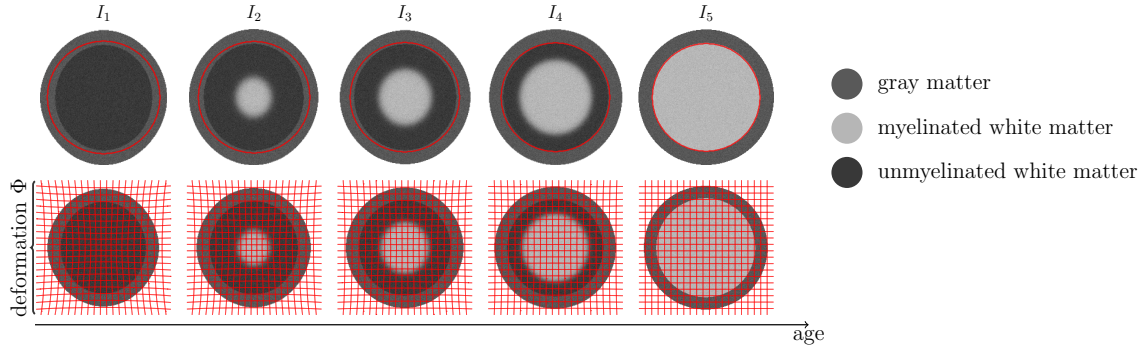


Figure 5.1: Synthetic dataset with logistic white matter intensity change and longitudinal deformation over time. I_1, \dots, I_4 are source images, I_5 is the target image. The red outline shows the white matter gray matter boundary of the target image (*top row*).

To test the influence of prior brain maturation information when used within the registration, I used a synthetic test case shown in Figure 5.1 and compared the model-based similarity measure SSR without prior to the new measure SSRP. The registration parameters were chosen experimentally to allow a reasonably flexible deformation (FAIR: SSD similarity measure with registration parameter $\alpha = 1000$). The five synthetic images I_1, \dots, I_5 represent simplified 2D MR images of the developing brain at times $t_i = 0, 0.5, 0.6, 0.7, 1.0$ with logistic white matter intensity change over time (the onset and rate of intensity change spatially varies within the white matter) and a Rician noise model. A small longitudinal deformation was added to the moving images I_1, \dots, I_4 to simulate a non-linear growth process (described in Section 5.2.2.1). The red outline shows the tissue gray/white matter boundary of the target image. The small misalignment of the tissue boundaries is representative of the misalignment seen in the real images after an initial affine registration. The intensity model estimation often fails to recover a reasonable model in these regions, due to the mixed gray and white matter voxels in the same spatial location at the various time points. The goal of the experiment is to recover the true deformation Φ_i^{-1} for each time point t_1, \dots, t_4 .

Table 5.1: Registration error for synthetic data experiment with varying prior weights and number of time points used for model estimation. The error is the average pixel-wise difference between the known true deformation and the recovered deformation within the mask of the target image (in pixels). The minimum for each row is highlighted in bold.

time points	prior weight (γ)				
	0	0.01	0.1	0.5	1
1 5	1.78	0.96	0.61	0.24	0.09
1 2 5	0.92	0.69	0.39	0.27	0.22
1 2 3 5	0.49	0.47	0.38	0.31	0.28
1 2 3 4 5	0.25	0.25	0.25	0.24	0.24

In this experiment the true intensity model is known for the synthetic images and it is used as the prior. The registration experiments were run with varying the prior weight parameter $\gamma = 0, 0.01, 0.1, 0.5, 1$ (with $\gamma = 0$ SSRP reduces to the standard SSR registration) and the number of time points available for the model estimation from 2 up to all 5 (total of 20 experiments). Figure 5.2 shows the registration results for two prior weights ($\gamma = 0, 1$) and two different number of time points for the model estimation. Using only two time points for the model estimation step, without the prior, results in a poor model and subsequently in poor registration. Adding the prior with more weight results in a greatly improved model and registration. Note that when all the time points are available for the model estimation the prior has less of an influence, since the model can be estimated well from the data alone. Table 5.1 shows the registration errors for all of the 20 experiments. The registration errors are computed as the average pixel-wise difference between the known true deformation and the recovered deformation within the mask of the target image. The prior considerably improves the registration results when the model is estimated from only a few time points, but has less of an effect when all time points are available. However, using the prior improved registration even with the complete dataset. This is due to the improved model estimation near tissue boundaries, where initial misregistration can result in mixing gray and white matter voxels and therefore lead to poor model estimation. Note that since the true prior is known for this experiment, the best results are obtained with largest overall weight on the prior (with two time points the data is weighted less than with all the time points).

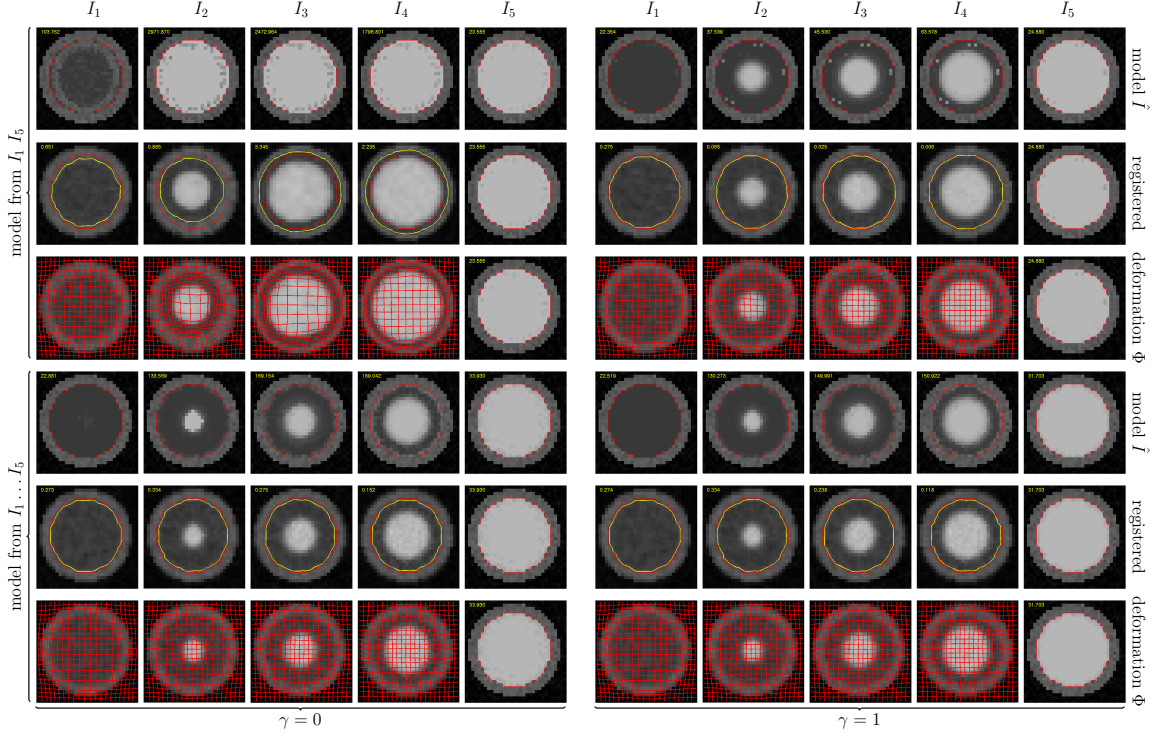


Figure 5.2: Registration results with no prior (left set of images) and use of the prior with weight 1 (right set of images) and the number of time points used for the model estimation. For the two different number of time points: *top row*: estimated model; *middle row*: the target tissue boundary (red) and the registered boundary (yellow) are overlaid on the registered images and should be close for good registration; *bottom row*: the deformation field is overlaid on the registered images. Ideally, there should be no deformation (straight grid) after the registration, since the geometry of the images is the same and only the intensity changes over time. With only two available time points for model estimation (top left quadrant), the model cannot be reliably estimated (top row) and therefore the registration produces large erroneous deformations (3rd row) and poor results (2nd row: the yellow tissue boundary outline of the registered image does not match the red tissue outline of the target image). The results improve with a large weight on the prior (top right quadrant) or with all five time points available for the model estimation (bottom left quadrant).

5.2.2 Registering Real 3D Dataset

The real monkey dataset is described in Section 4.2 and shown in Figure 4.1 for a single subject. I assessed the quality of the registration results using 35 manually defined landmarks. The landmarks were placed by a trained expert at prominent anatomical locations.

5.2.2.1 Accuracy of affine registration

While the non-uniform growth of various brain regions (Knickmeyer et al., 2008) indicates that affine registration should not be sufficient to align the longitudinal images, and therefore a deformable

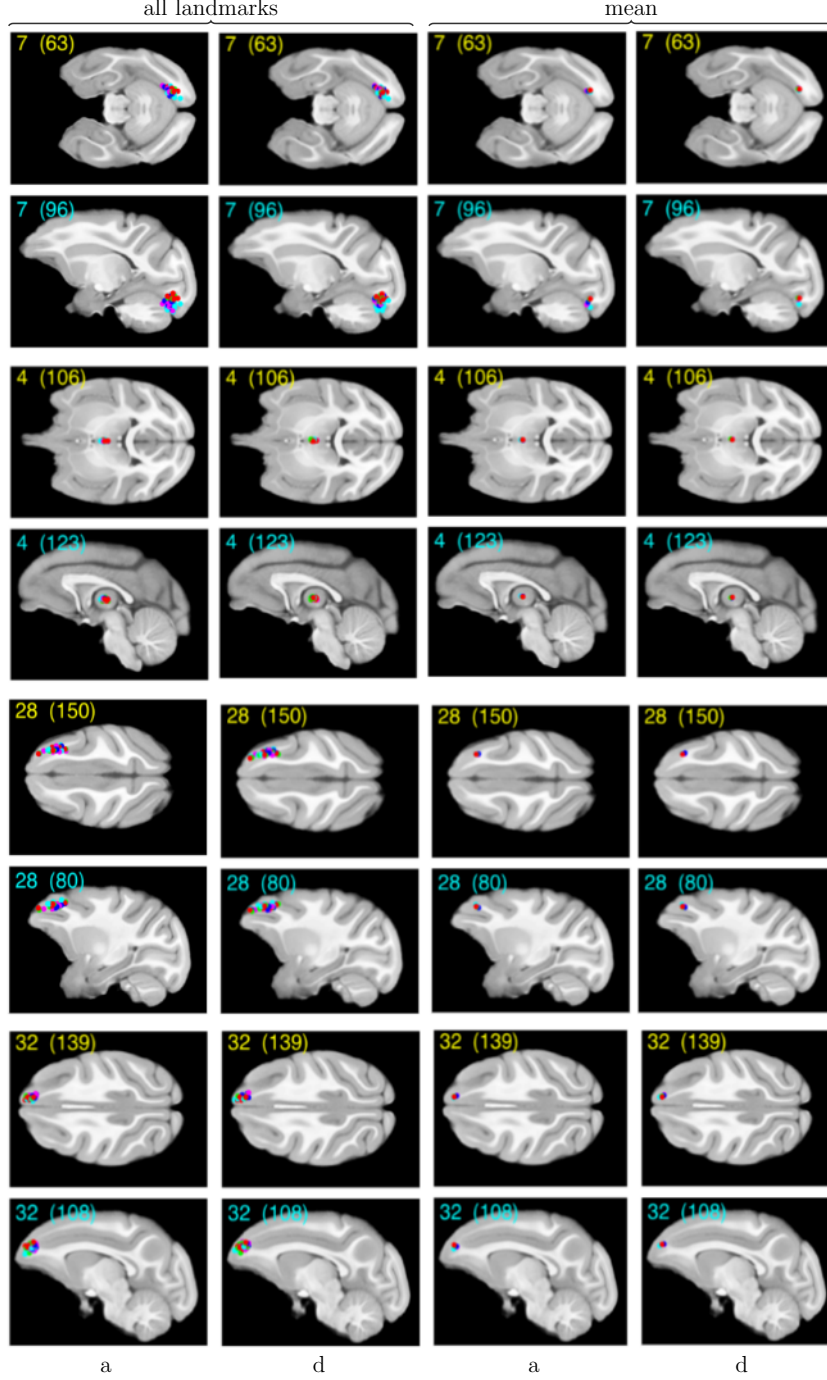


Figure 5.3: A subset of landmarks (7, 28, 4, 32) are shown on the structural atlas. For each landmark, the location is shown on the axial (*top row*) and the sagittal (*bottom row*) plane. The landmark locations are color coded by age (2wk: cyan; 3mo: magenta; 6mo: green; 12mo: blue; 18mo: red). For each landmark, the first two columns show all 50 locations (10 subjects \times 5 time points) for affine (a) and deformable (d) registrations. Columns 3 and 4 show the mean location for each age for affine (a) and deformable (d) registrations. Note that the I_{18mo} (target) images were affinely registered to the atlas before the within subject affine and deformable registrations, but variations in anatomy and landmark placement across subjects can be seen as the spread in landmark locations.

registration method is necessary, our experience suggests that affine registration alone can produce a good alignment even between I_{2wk} and I_{18mo} . To test the within-subject appropriateness of a simple affine image-alignment, for each subject I first affinely registered the longitudinal images (I_{2wk}, \dots, I_{12mo} to I_{18mo}) using a normalized cross correlation similarity measure, which has previously been found effective (see Chapter 3) even in the presence of image intensity changes as expected during brain maturation. Then I performed an additional deformable registration of the affinely aligned images using SSR.

The registration error was calculated as the distance between the transformed and the target landmarks. Significance was calculated with a paired-sample t-test at a significance level of $\alpha = 0.05$. The boxplots in Figure 5.5 show the landmark alignment errors per time point for both affine (a) and deformable (d) registration methods, using all landmarks (left plot; 350 landmark pairs per time point) and using only a subset of six landmarks (right plot; 60 landmark pairs per time point).

What is clear from both plots is that the registration error for both affine and deformable registration is inversely proportional to age, but there is no clear benefit of using deformable registration when aggregating the results over all the landmarks (the mean registration error for I_{2wk}, \dots, I_{12mo} are 1.95, 1.57, 1.04 and 0.65 mm for affine and 1.82, 1.44, 0.98, 0.74 mm for deformable registration, respectively; the means of the two methods are significantly different for each age). This would suggest that the poor affine alignment of I_{2wk} is not the result of an insufficient transformation model, but possibly increasingly inaccurate landmark placement due to poor tissue contrast at earlier time points (see Figure 4.2).

However, taking a closer look at individual landmarks revealed that only a small subset was not well aligned after affine registration. Figure 5.3 shows four landmarks after affine and deformable registration. Landmarks 28 and 4 were well aligned after affine registration and thus did not change after deformable registration; however, landmarks 7 and 32 moved closer to the target 18 month locations. Out of the 35 landmarks, I chose a subset of 6 that have significantly changed after the deformable registration (improvement was not a criteria when choosing the subset). The high variability across subjects of certain landmarks may be attributed to the inaccuracy of the landmarks at the earlier time points, due to poor tissue contrast or anatomical variations in those brain regions.

Once the analysis was restricted to a subset of the 6 landmarks previously described, the benefit of the deformable registration became apparent (see right plot in Figure 5.5; the mean registration error for I_{2wk}, \dots, I_{12mo} are 2.44, 2.03, 1.24, 0.59 mm for affine and 1.97, 1.24, 0.86, 0.72 mm for deformable registration, respectively; the means of the two methods are significantly different for each age). In fact,

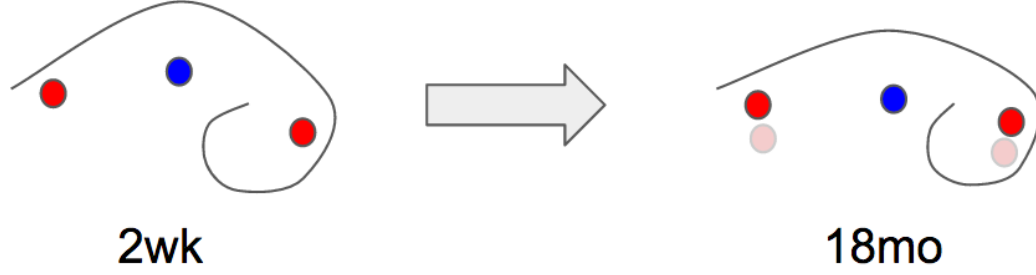


Figure 5.4: Cartoon depiction of the typical anterior-posterior deformation seen between the 2 week and the 18 month images (in the sagittal plane). The deformation is a result of the non-uniform growth trajectories of various brain regions. Landmarks located near the anterior and posterior regions (*red*) are affected more by the deformation than centrally located landmarks (*blue*).

these results are consistent with the longitudinal deformations seen in the images. Figure 5.4 shows the typical deformation of the brain seen in the datasets: an upward bending of the brain about the brainstem along the anterior-posterior line. This finding is consistent with the known developmental growth trajectories of the centrally located lateral ventricles and the cerebellum that contribute the majority of the subcortical brain volume increase during early postnatal development (Knickmeyer et al., 2008). The landmarks that have changed significantly are located in the regions that the bending deformation affected the most (superior-anterior and inferior-posterior regions).

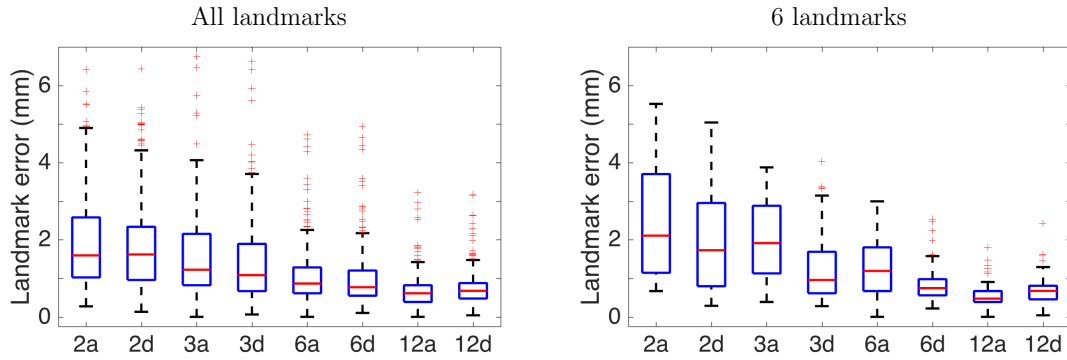


Figure 5.5: Landmark errors per time point for all 10 subjects, after registering the earlier time points I_{2wk}, \dots, I_{12mo} to the oldest I_{18mo} image within subjects using affine (2a, ..., 12a) and deformable (2d, ..., 12d) registration. While the deformable registration slightly improves alignment for I_{2wk}, \dots, I_{6mo} (and worsens it for I_{12mo}), the changes are negligible when aggregating over all landmarks (*left plot*), and are more prominent when only considering a subset of the landmarks (*right plot*).

5.2.2.2 Influence of prior with missing data

In this experiment, I tested the utility of SSRP that incorporates a prior into the model-based deformable registration method.

I registered a subset of the four early time points I_{2wk}, \dots, I_{12mo} to the target image I_{18mo} with the proposed model-based method for each of the 10 subjects. The subsets either contained $\{I_{2wk}\}$, $\{I_{2wk}, I_{3mo}\}$, $\{I_{2wk}, I_{3mo}, I_{6mo}\}$, or all four, $\{I_{2wk}, \dots, I_{12mo}\}$, moving images (the last subset corresponding to no missing data). The missing time points were not used for the model estimation. For each of the four subsets, the registration experiments were repeated with five different prior weights $\gamma = 0, 0.01, 0.1, 0.5, 1$ (with $\gamma = 0$ SSRP reduces to the standard SSR registration) totaling 20 experiments (as in Section 5.2.1). Figure 5.6 shows the estimated model and the registration results for a single image.

As in Section 5.2.2.1, the registration error was computed as the distance between registered and target landmarks. I used the most challenging registration between I_{2wk} and the I_{18mo} to assess the quality of the registrations (note that some of the intermediate time points were used for the model estimation for three of the subsets). Similarly to the previous experiment, I chose a new subset of 6 landmarks (different from the one used in Section 5.2.2.1) in the central region of the brain where using a prior had noticeable impact. The following results were computed using the subset of landmarks.

Table 5.2 shows the registration errors for all 20 experiments. For each moving image subset with a non-zero prior weight (columns 2-5), the registration errors were compared to the zero prior weight errors (column 1). The prior significantly improved the registration results by 0.21 mm for the datasets with three missing time points (top row; note that the model has only two parameters, onset and rate of myelination as described in Section 3.1.2, therefore two time points may be sufficient for estimation) at prior weight 1 (highlighted in bold). Additionally, there were significant improvements with the prior for two and no missing datasets. However, all improvements were at a sub-pixel level.

The synthetic experiments show a clear benefit when using the prior with missing data, but the improvement for the real data is difficult to show globally. While the prior has a clear impact on the estimated model images (\hat{I}), the benefit of using a prior only becomes evident when restricting the landmarks to the central region of the brain where the model estimation is most influenced by the prior. Note that while these improvements are only measured at sparsely placed landmarks, when trying to

Table 5.2: Registration error (in mm) for monkey data experiment with varying prior weights and number of time points used for model estimation. The registration errors are computed for the I_{2wk} to I_{18mo} registrations for all 4 subsets of moving images and 5 prior weights. For each row, statistically significant improvements with respect to the first column ($\gamma = 0$) are highlighted in bold.

time points	prior weight (γ)				
	0	0.01	0.1	0.5	1
1 5	2.08	2.11	2.07	2.02	1.87
1 2 5	1.96	1.91	1.91	1.84	1.86
1 2 3 5	1.88	1.89	1.91	1.86	1.86
1 2 3 4 5	1.90	1.93	1.84	1.88	1.89

measure subtle volumetric changes during development the small improvements are integrated over large structures.

A more in-depth analysis of the subtle improvements should be part of future work, but I list a few possible explanations of why the benefit of using a prior is not as evident for the real data as it was for the synthetic dataset: (i) the landmarks are placed in easily identifiable regions with prominent structures, therefore these regions are easily registered even without a prior; (ii) the landmarks are inaccurate in the earlier time points due to the poor tissue contrast and noisy images (see Figure 4.2); (iii) the morphological changes, other than affine, between the 2 week and the 18 month images are too subtle to be measured by sparse landmarks and only affected a small subset of the 35 landmarks.

5.3 Conclusions

I proposed to incorporate a longitudinal intensity atlas into a model-based longitudinal similarity measure. The atlas is used as a prior and can guide the registration when the model cannot be reliably estimated due to missing data. While the similarity measure uses a logistic model, the formulation is general and other models can be used. I showed that using a prior can improve registration with missing data. In the future, I will investigate the benefit of using a prior with datasets containing larger non-linear morphological changes.

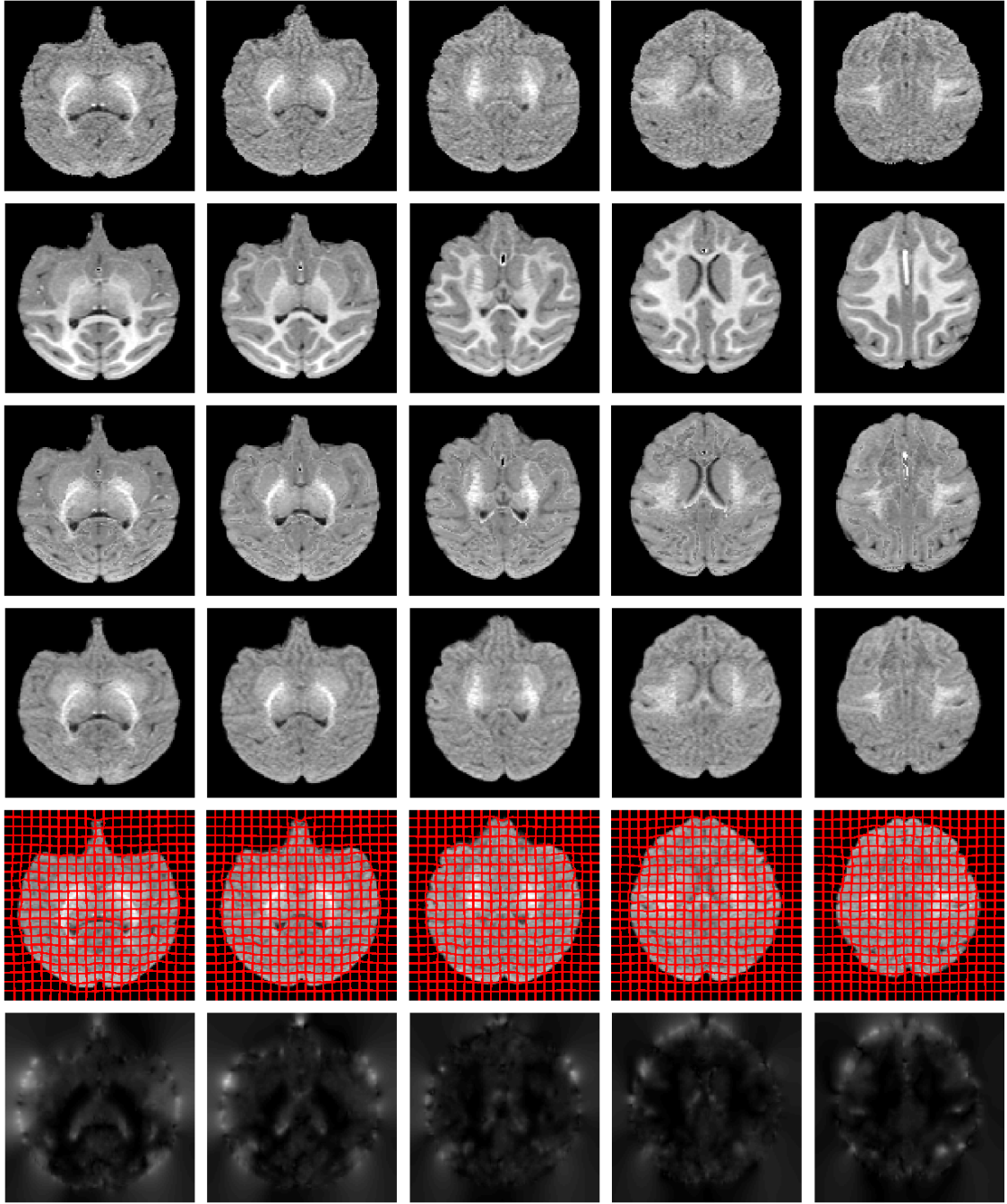


Figure 5.6: Registration results for a single subject. *Top row*: axial slices from 2 week moving image; *2nd row*: 18 month target image; *3rd row*: estimated model (note that the morphology is the same as the 18 month image shown in the row above, but the appearance is at age 2 weeks). *4th row*: registered image. *bottom 2 rows*: deformation. The resulting target image matches the appearance of the moving image closely. The landmarks used for validation are not shown here.

CHAPTER 6

3D Reconstruction of Serially Sectioned Images

A major line of research in computational neuroscience seeks to understand the formation and patterning of the neural circuitry in the brain (Keller and Ahrens, 2015). Investigating brain development is challenging technically, in part, due to the difficulty associated with collecting and analyzing empirical data from model organisms and the immense complexity of the biological processes involved. Brain function is an emergent property of the complex network of connections between neurons. In most organisms, the neural circuitry is not hard-wired to generate fixed patterns of behavior. Instead, the plasticity of the connections ensures that animals can adapt to changes in the environment (Zilles, 1992). This adaptability, however, is bound by the structural organization of the brain. While structural plasticity, mediated by neurogenesis, has been observed in the adult mammalian brain, the neuronal placement and composition established during the formation of the nervous system remain mostly unchanged throughout the life of the organism (Lipp and Bonfanti, 2016).

Therefore, the formation of functional neural connectivity depends on an appropriate neuronal placement in the developing brain (Ayala et al., 2007; Marín and Rubenstein, 2003; Oh et al., 2014). This placement is achieved through a process of coordinated patterns of neuronal migration, whereby distinct classes of neurons navigate long distances from their sites of birth to their final destinations in the cerebral cortex (Ghashghaei et al., 2007; Guo and Anton, 2014; Di Cristo, 2007; Lichtman and Smith, 2008), thereby forming the basis of the neuronal connectome. Figure 6.1 gives a high-level overview of neuron migration in the mouse brain: projection and interneurons originate in distinct areas of the brain and use various modes of locomotion and guidance to arrive at their place of implantation in the cortex. Defects in neuronal migration alter the positioning and thus the connectivity and function of the embedded neurons (Evsyukova et al., 2013). Such disruptions are at the core of a wide spectrum of neurological disorders, including autism, schizophrenia, epilepsy, fetal alcohol syndrome, mental retardation (Bailey, 1998; Bill and Geschwind, 2009; Evsyukova et al., 2013) and malformations, such as microencephaly, schizencephaly, lissencephaly, and macro/microgyria (Evsyukova et al., 2013; Metin

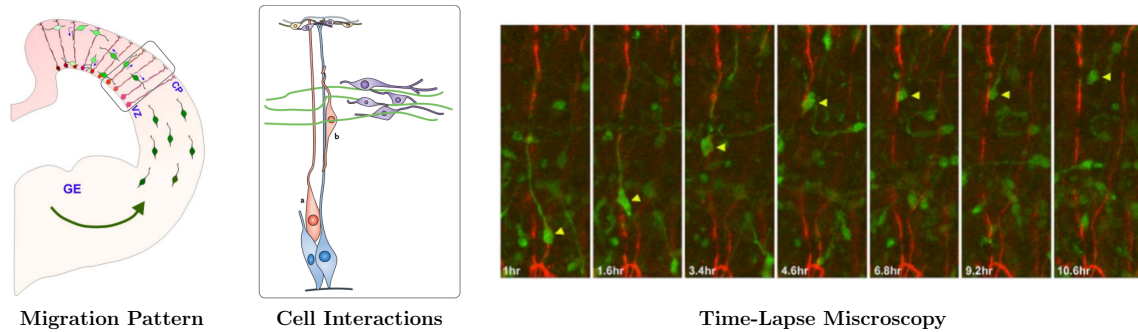


Figure 6.1: Neuron generation and differentiation happen at distinct locations. Left: Illustration of a coronal section of an embryonic mouse cortex. Interneurons are generated predominantly in the ganglionic eminence (GE) and migrate tangentially; projection neurons are generated near the ventricular zone (VZ) and migrate radially. Middle: Both populations migrate to the cortical plate (CP) using different modes of locomotion. Right: Fluorescence confocal microscopy images showing the radial adhesive locomotion of an interneuron using the radial processes of glia. (Images: Eva Anton)

[et al., 2008](#)). However, in spite of its significance, how different types of cortical neurons migrate from their sites of birth to their appropriate positions in the developing cerebral cortex remains a mystery.

The comprehensive reconstruction of neuronal dynamics is important for understanding the morphological development of the brain, comparatively analyzing mutant phenotypes, and correlating genetic expression with migration patterns. In order to faithfully reconstruct neuronal dynamics, the imaging modality used should have i) high enough spatial resolution to capture individual neurons, ii) high temporal resolution to allow the tracking of neuron migration, iii) specificity to the different classes of neurons, and iv) in vivo 3D volumetric images. Currently, no such imaging modality exists and, despite advances in noninvasive imaging technologies, such as micro-MRI and micro-CT, they lack the spatial resolution and specificity of ex vivo histology studies that remain the standard method to obtain high-resolution images of microanatomy ([Casero et al., 2017](#)). Histology-based imaging techniques, however, are destructive by their nature and cannot be used for longitudinal imaging studies. In order to study neuronal dynamics over time, we have to rely on cross-sectional studies by imaging multiple individuals at different time points.

In combination with transgenic model organisms and fluorescent histochemical markers, fluorescence spectral confocal microscopy is well suited for studying neuronal dynamics ([Osten and Margrie, 2013](#)), but it comes with its own set of challenges. In particular, due to the limited depth of tissue penetration of the histochemical markers and relatively shallow imaging depth of confocal microscopy, large samples have to be physically sectioned into thin tissue sections. In our study, the model organism is the mouse

imaged at multiple time points during embryonic development, when the size of the brain is $1 - 2\text{mm}$ and the thickness of the resulting sections is $50 - 70\mu\text{m}$ (about the thickness of a human hair). Confocal microscopy can focus at varying depths in the tissue and therefore generate a stack of optical slices through each section that is inherently coregistered. One of the main limitations of techniques requiring serial sectioning is that the images of the tissue sections cannot simply be stacked to reconstruct a coherent 3D volume that closely resembles the original sample. While the 2D optical slices within a tissue section can be reassembled into a 3D volume of the particular tissue section, the sectioning process introduces artifacts that affect each tissue section differently and destroys the inherent rigid alignment between sections.

In fact, there are two types of deformations we have to consider if the aim is a geometrically faithful reconstruction that matches the *in vivo* brain: global 3D nonlinear deformations (referred to as primary deformations) and nonlinear deformations specific to each of the tissue sections (secondary deformations) (Dauguet et al., 2007). The primary deformations are caused by the brain extraction process, loss of fluids and dehydration (causing shrinkage), chemical fixation, and embedding. The chemical fixation of tissue results in additional tissue shrinkage, while the excision and embedding introduce nonlinear deformations due to the mechanical stresses imposed on the tissue (Burton et al., 2014). These artifacts, however, do not impact the reassembly of the tissue sections into a coherent 3D volume, as they affect the brain as a whole before sectioning (Dauguet et al., 2007). Nevertheless, these global deformations should be taken into account when the 3D reconstruction is compared to other 3D volumes.

The secondary, and most severe, deformations stem from the mechanical sectioning, staining, and mounting of the embedded brain tissue, resulting in additional nonlinear deformations (Gardella et al., 2003) and often tearing or folding of the thin sections. We can reconstruct a coherent 3D volume by coregistering the stack of tissue sections. Since the optical slices within a tissue section are coregistered, we only need to match the optical slices at the interface of the consecutive tissue sections. The deformation that matches the tissue section interfaces then can be applied to the whole tissue section. However, an especially difficult part of registering the tissue section interfaces is that the anatomical structures in consecutive tissue sections are not equivalent. This mismatch can be attributed to the destruction of tissue, during the mechanical sectioning, and the optical limitation of the microscope to image a sample

near the glass coverslip. The difference in morphology can be severe with large inter-slice gaps (Ourselin et al., 2001). Therefore, exact matching of neighboring tissue sections is not desirable.

6.0.1 Previous Work

The process of reconstructing the original 3D volume of a sample from 2D histological sections, generally referred to as 3D reconstruction, has received considerable attention since the first serial sectioning and modeling study in 1883 (Born, 1883) and the landmark reconstruction of the retina in 1958 (Sjöstrand and Baker, 1958). The typical first step of the reconstruction process is a rigid alignment of the sections to each other. Due to the nonlinear deformations after sectioning, the rigid alignment usually produces a jagged 3D volume and the alignment is further refined with higher degrees of freedom registration methods, including affine (Adler et al., 2014), triangular mesh with spring connected vertices (Saalfeld et al., 2012), or nonparametric displacement field (Gaffling et al., 2015).

A large number of methods reconstruct the 3D volume with the aid of a reference image. The reference image can either be the same sample imaged with a non-destructive tomographic method, such as micro-MRI or micro-CT, before sectioning (Adler et al., 2014; Ceritoglu, 2010; Ourselin et al., 2001; Khimchenko et al., 2016), the inherently registered stack of 2D block face images captured directly at the vibratome (Casero et al., 2017), or an external atlas constructed from other samples (Ali and Cohen, 1998; Ju et al., 2006; Majka et al., 2016). Some methods have relied on fiducial markers embedded in the sample before sectioning to aid with alignment (Goldszal, 1995). However, fiducial markers can be unreliable, difficult to place, or require placement that results in destroying parts of the sample. Depending on the number of fiducials, the degrees of freedom of the transformation model might also be very limited. A transformation model with few degrees of freedom might be sufficient for rigidly embedded samples, such as plastic- or cryosectioning (Gardella et al., 2003), but it cannot account for the complex tissue deformations encountered with tissue embedded in a soft medium, for example agarose (used for our study). When available, external references can reduce geometric artifacts that are known to hinder reference-free reconstruction: straightening of curved shapes (reconstructing a straight banana from a stack of slices), reorienting the z-axis (reconstructing a normal *I* from an italicized *I*), or changing asymmetric shapes into symmetric ones (Casero et al., 2017). In our study, a reference image was not used because i) tomographic or block face images of the sample were not acquired before sectioning, and ii) external reference images could not be reliably matched to the developmental age of the mouse

embryo due to the tremendous rate of prenatal growth (see Figure 6.2 for a depiction of the mouse embryo development), and iii) the embryonic mouse brain is approximately a tubular shape with two planes of symmetry normal to the cutting plane. Instead, our method minimized the geometric artifacts by estimating a reference shape from the data, therefore alleviating the need for external references.

Other methods have used segmentation (Hibbard and Hawkins, 1988) and automatically derived features from the images, such as contours (Cohen et al., 1998; Ali and Cohen, 1998). Using the external surface characteristics alone can result in misalignment of the internal structures (Cifor et al., 2011) that can be mitigated by relying on other features, including edges (Kim et al., 1995; Kay et al., 1996) and points (Rangarajan et al., 1997). The internal point features might also be user-defined landmarks used to register histology images to a reference MR image (Stille et al., 2013; Jacobs et al., 1999; Li et al., 2006; Schormann et al., 1993; Zhan et al., 2007). These feature-based methods, however, are limited by the sparsely distributed user-defined features or by the scarcity of good quality features in certain modalities, such as confocal fluorescence microscopy (used for our study).

Intensity-based methods that rely on the similarity between pixel intensities of corresponding anatomical structures have also been successfully used for section alignment (Andreasen et al., 1992; Kim et al., 1997; Ourselin et al., 2001). These methods can overcome the poor internal alignment of the segmentation and contour-based methods, as well as the scarcity of features associated with some of the feature-based methods. However, they require an image modality that, in contrast to the fluorescence microscopy used in our study, captures dense structural information: traditional histology images using broad-spectrum light microscopy (Andreasen et al., 1992; Kim et al., 1997; Ourselin et al., 2001; Schmitt et al., 2006; Majka et al., 2016) or transmission electron microscopy (Saalfeld et al., 2012).

One approach that is similar to the proposed method uses iterative stacking and refinement, with an external reference volume, to reconstruct 3D volumes of retrograde fluorescent tracer injections in the marmoset cerebral cortex (Majka et al., 2016). Fluorescence microscopy images of the tracer injections were acquired only for every fifth section, while the remaining sections were Nissl-stained and used as proxies for the tracer sections during the reconstruction process. The reference volume was constructed from a publicly available atlas that also contained Nissl-stained acquisitions. Thus, the optical acquisitions with dense structural features were used for reconstruction. While our proposed method uses a similar iterative stacking and refinement strategy, it eliminates the need for an external reference volume and a proxy modality with dense image features.

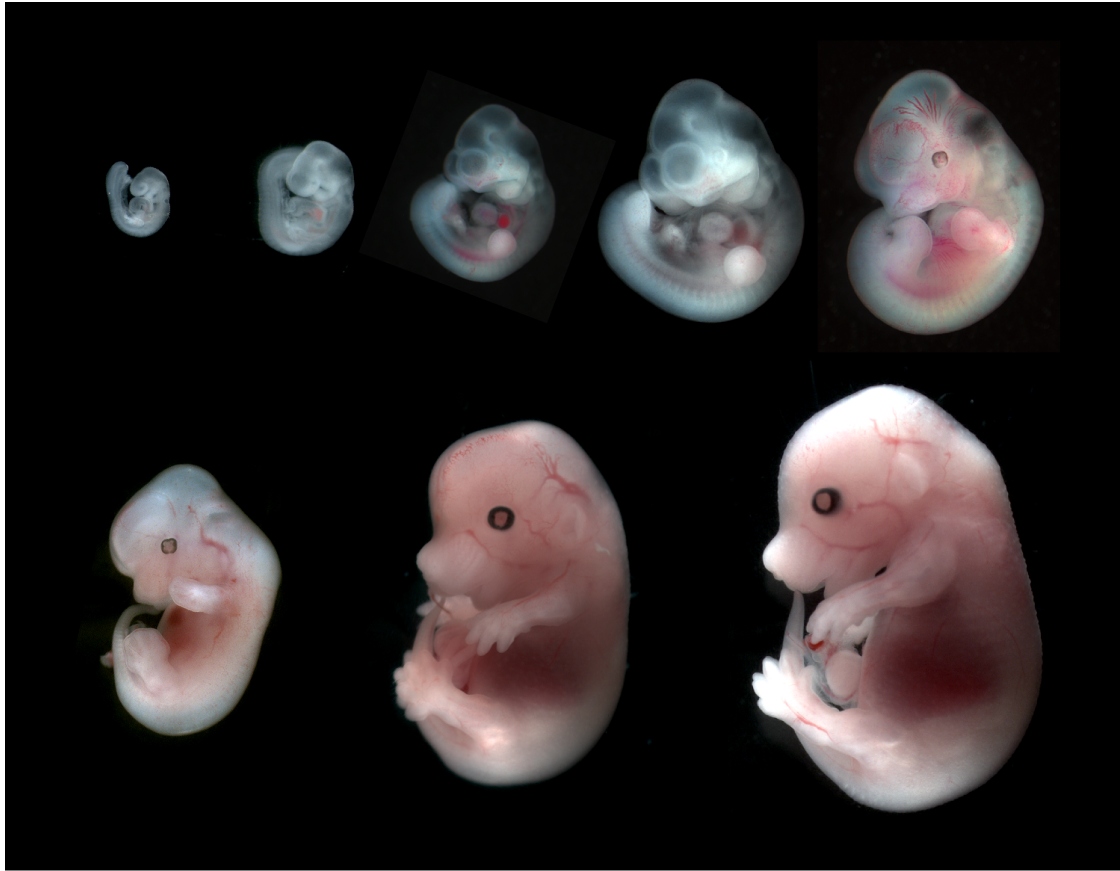


Figure 6.2: Mouse embryo development from embryonic age 9.5 days to 15.5 days. The first three images are half a day apart, the rest are evenly spaced one day apart. The average mouse gestation is 20 days. [Image from: Dr Erica D. Watson, University of Cambridge (with permission)]

6.1 Image Acquisition

Two lines of transgenic mice, *Dlx5/6-cre-IRES-EGFP* (Stenman et al., 2003) and *Dcx-DsRed* (Wang et al., 2007), were crossed to generate bitransgenic mice containing GFP labeled interneurons and DsRed positive projection neurons, respectively. The 4% paraformaldehyde fixed brains were excised, embedded in agarose, and coronally sectioned, using a vibratome into $50 - 70\mu m$ sections (see Figure 6.3 for an overview of the sectioning process). The two distinct classes of neurons were then immunolabeled with fluorescent anti-GFP and anti-RFP antibodies (Higginbotham et al., 2012) and cell nuclei were tagged with DAPI markers. The tissue sections were imaged, using a Zeiss LSM 780 32-channel spectral imaging confocal microscope, resulting in 3 channels shown in Figure 6.4: interneurons (green), projection neurons (red), and cell nuclei (blue). The embryonic brains were imaged at three different embryonic (E) ages: E14, E16, and E18 days (see Figure 6.2 for an illustration of the prenatal mouse development).

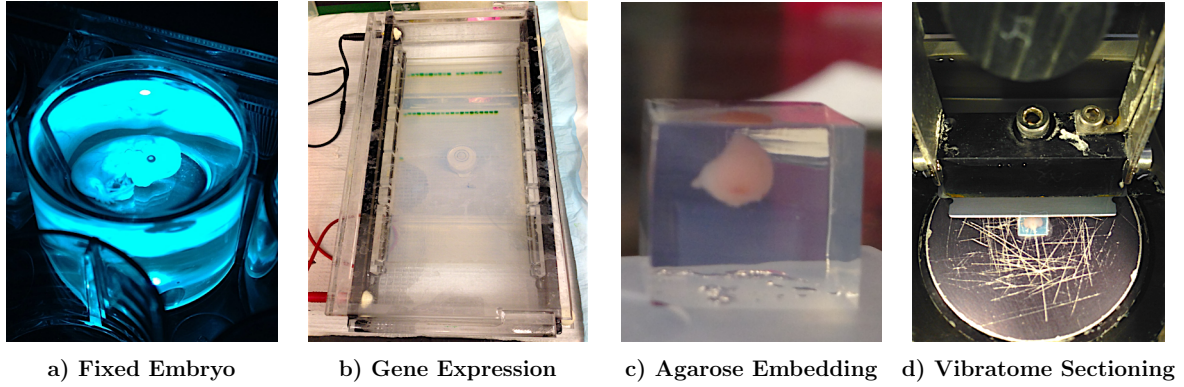


Figure 6.3: Serial sectioning of the embryonic mouse brain. The embryo is first fixed in paraformaldehyde and the presence of the fluorescent transgenic markers is checked by visual inspection (a) and with a gene expression assay (b). The brain is then excised, embedded in agarose (c), and sectioned into $50 - 70\mu m$ sections using a vibratome (d). The tissue sections are immunolabeled with fluorescent anti-GFP and anti-RFP antibodies, and the cell nuclei are tagged with DAPI marker. Finally, the sections are imaged with a spectral imaging confocal microscope, resulting in 3 channels (one for each of the fluorescent markers).

Four samples were collected at E14 and E16 and three samples at E18, resulting in 11 normal brains total. One brain at each time point was acquired at a spatial resolution of $0.42 \times 0.42 \times 1.2\mu m$, while the others at a lower resolution of $0.83 \times 0.83 \times 1.2\mu m$ or $0.83 \times 0.83 \times 1.0\mu m$. Whole brain datasets of serially sectioned fixed tissue allow wide spatial coverage but only provide a static snapshot of the brain. However, by imaging multiple brains at different stages of embryonic development, we can capture a coarse temporal trend (on the order of days) of neuron migration. The acquisition produces a stack of approximately 10 – 18 images (also referred to as slices) from each tissue section (in total, about 40 – 70 tissue sections, 500 – 1000 optical images, 50 – 800 G voxels per brain). In addition, two mouse models of fetal alcohol syndrome were also imaged at E18.

6.1.1 Measuring Tissue Loss Due to Sectioning

The mechanical sectioning process and mounting introduce tears, deformations, shrinkage of tissue sections and gaps in between where image information cannot be acquired (Dauguet et al., 2007). These artifacts have to be considered for a faithful 3D reconstruction.

The size of the gaps and tissue shrinkage was estimated by imaging a region of interest ($607 \times 607\mu m$ with $1.1861 \times 1.1861 \times 1\mu m^3$ voxel size) of a thick section with a two-photon microscope (that has deep penetration down to $500\mu m$), resulting in a 3D volume, I^{tp} . Next, the thick section was sectioned further

Table 6.1: Details of the 13 mouse brain datasets. The datasets are numbered in the order of acquisition and prefixed with N for normal subjects and F for subjects with fetal alcohol syndrome. The following channels were used to image interneurons (green), projection neurons (red), and cell nuclei (blue): **EGFP (488 nm)**, **DsRed (561 nm)**, **DAPI (405 nm)**. The order of the channels listed in the table matches the acquisition order. Three datasets, highlighted in bold, were excluded from analysis: N01 (missing DsRed channel), N11 (missing sections), and F13 (acquisition artifacts). The number of tissue sections is also listed, along with the number of damaged sections due to folding or tearing.

Dataset	Age (days)	Objective	Channels	Resolution	Voxel Size (μm)	Sections [damaged]
N01	E14	10x	EGFP, DAPI	512	0.83 x 0.83 x 1.0	38 [0]
N02	E14	20x	DAPI, EGFP, DsRed	1024	0.42 x 0.42 x 1.2	43 [2]
N03	E14	20x	DsRed, EGFP, DAPI	512	0.83 x 0.83 x 1.2	46 [0]
N04	E14	20x	DsRed, EGFP, DAPI	512	0.83 x 0.83 x 1.2	45 [0]
N05	E16	20x	DAPI, EGFP, DsRed	1024	0.42 x 0.42 x 1.2	36 [0]
N06	E16	20x	DsRed, EGFP, DAPI	512	0.83 x 0.83 x 1.2	28 [0]
N07	E16	20x	DsRed, EGFP, DAPI	512	0.83 x 0.83 x 1.2	29 [3]
N08	E16	20x	DsRed, EGFP, DAPI	512	0.83 x 0.83 x 1.2	46 [5]
N09	E18	20x	DAPI, EGFP, DsRed	1024	0.42 x 0.42 x 1.2	40 [3]
N10	E18	20x	DsRed, EGFP, DAPI	512	0.83 x 0.83 x 1.0	52 [25]
N11	E18	20x	DAPI, EGFP, DsRed	512	0.83 x 0.83 x 1.2	53 [21]
F12	E18	20x	DAPI, EGFP, DsRed	512	0.83 x 0.83 x 1.2	54 [6]
F13	E18	20x	DAPI, EGFP, DsRed	512	0.83 x 0.83 x 1.2	66 [6]

into 7 consecutive $50\mu m$ sections, and the same region of interest was imaged with the imaging protocol used to acquire the neuron migration data on the confocal microscope ($1.0378 \times 1.0378 \times 1.4734\mu m^3$ voxel size), resulting in 7 image volumes, I_i^{con} for $i = 1, \dots, 7$. The thin sections were then located within the thick section, using 56 manually identified landmark pairs. The gaps and the tissue shrinkage were measured, using the two-photon volume as a reference. Figure 6.5 shows the mapping of landmarks and section boundaries between the two acquisitions. I measured tissue shrinkage by computing the distances along the z-axis (depth) between consecutive landmarks in the tissue sections of both acquisitions. Next, I computed the ratio of the corresponding landmark distances between the two acquisitions as

$$d_{i,j} = \frac{LM_{i,j}^{tp} - LM_{i+1,j}^{tp}}{LM_{i,j}^{con} - LM_{i+1,j}^{con}}, \quad (6.1)$$

where $LM_{i,j}^{tp}$ is the depth of landmark i in slice j of the two-photon image and $LM_{i,j}^{con}$ is the depth of the corresponding landmark in the sectioned confocal images. The median decrease of consecutive landmark distances from the two-photon image to the confocal images was 50%. That is, on average the tissue sections were half of their original thickness (based on the two-photon acquisition) after sectioning, staining, mounting and confocal acquisition.

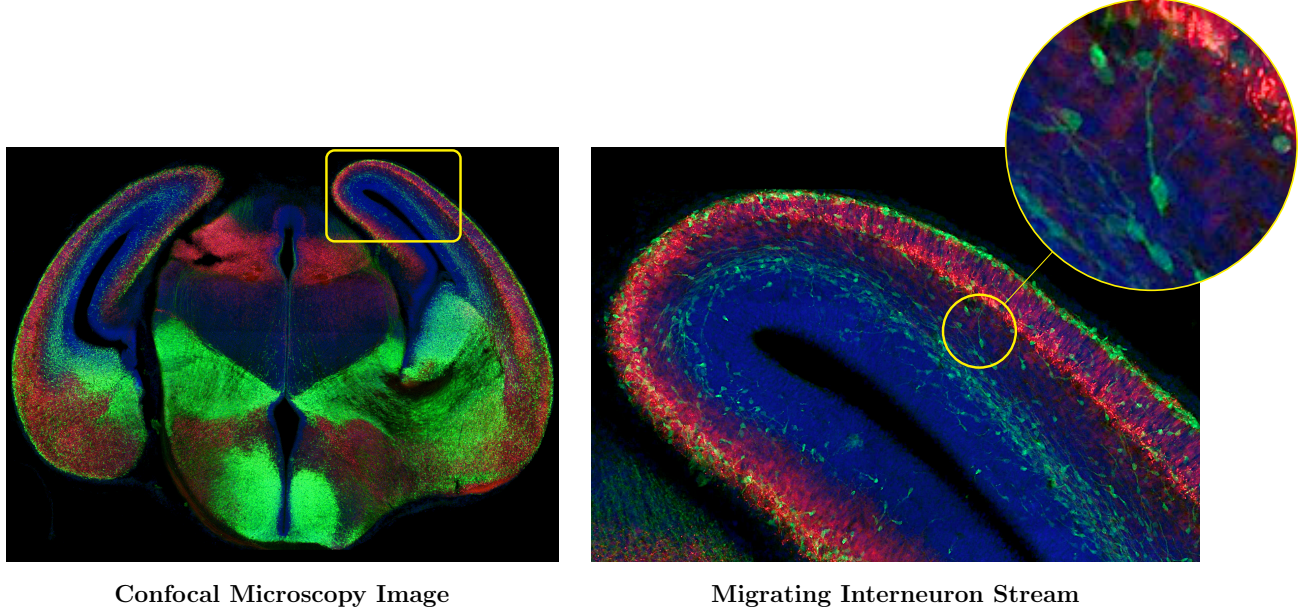


Figure 6.4: Confocal microscopy imaging of a tissue section labeled with 3 fluorescent markers: projection neurons (red), interneuron (green), and cell nuclei (blue). A maximum intensity projection of a single tissue section is shown on the left. An enlarged section (yellow rectangle) on the right shows the stream of interneurons migrating parallel to the cortical plate. The magnification shows projection neuron breaking away from the migration stream and moving towards the cortical plate. The neuron uses its extended process for guidance and locomotion.

In addition, I estimated the size of the gaps between tissue sections where tissue was destroyed or image data could not be acquired. The confocal image volumes contained sectioning artifacts (tissue tearing or folding) and imaging artifacts that required manual identification of the tissue section boundaries. Using the manually identified section boundaries as a reference, I computed the depth of each landmark, $d_{i,j}^{con}$ (depth of landmark i in confocal section j), within the confocal tissue section that contained the landmark. To identify the corresponding section boundary in the intact two-photon volume, the confocal landmark distances were first mapped to corresponding distances in the two-photon image, $d_{i,j}^{tp}$ based on the 50% tissue shrinkage. Finally, candidates of the tissue boundary location were calculated using each two-photon landmark and its mapped distance to the boundary. The final tissue boundary was computed as the median of the candidate locations (see dashed lines in Figure 6.5). The gaps between the sections were 2, 4, 0, 6, 3, and 20 μm , with a median gap size of 3.5 μm .

The 50% decrease in tissue thickness is likely caused by stretching during the mounting process, pressure from the coverslip, and additional loss of moisture from the tissue after the sectioning. The landmark positions, and therefore the shrinkage and tissue gap estimates, show considerable variation.

This is due, in part, to the challenging task of identifying landmarks and reliably matching those sparse landmarks across the two different acquisitions. Furthermore, even good landmark pairs can produce highly variable results, due to the differential compression and deformation of tissues with different physical properties (Gardella et al., 2003). The gaps between the sections indicated an average 7% tissue loss, with an average $53\mu m$ two-photon tissue section thickness.

6.2 3D Reconstruction

The continuous 3D brain volume is reassembled by minimizing the secondary deformations, due to sectioning and mounting, via image registration. The registration method used for the reconstruction needs to take into account the gaps between sections, as well as tissue shrinkage, and allow large deformations to account for the displacements caused by the mechanical stresses of sectioning and mounting—requirements not met by standard registration methods. At the same time, the deformable registration should not produce exact matching between sections, since the sections are not anatomically equivalent. That is, I cannot simply register the neighboring slices at the tissue section boundaries of different sections, since the slices do not contain the same anatomy; direct registration would remove the true anatomical differences between the sections. Figure 6.6 shows a set of synthetic 3D images that illustrates the typical artifacts arising from sectioning. The aim of the proposed method is to estimate the original 3D shape of the intact brain (top row) and undo the effects of secondary deformations (middle row) and tissue loss (bottom row). In addition to the secondary deformation artifacts, incidental artifacts are introduced when the thin tissue sections tear or fold during sectioning or mounting. The registration method proposed here only aims to remove the typical artifacts due to secondary deformations, but can handle occasional tearing and folding of individual sections.

Another acquisition side effect is the variability of the tissue staining that affects the appearance of the images (Model and Burkhardt, 2001). While the same protocol was used to prepare, mount, and image each tissue section, the variability in tissue properties, sectioning, staining, mounting, and imaging resulted in considerable variability in the appearance of the tissue sections. Figure 6.7 show maximum intensity projections of the 45 sections from one of the highest quality collects (N04). The appearance changes between sections result from a number of spatially non-uniform processes, therefore even after intensity normalization the appearance of some of the neighboring sections differs significantly.

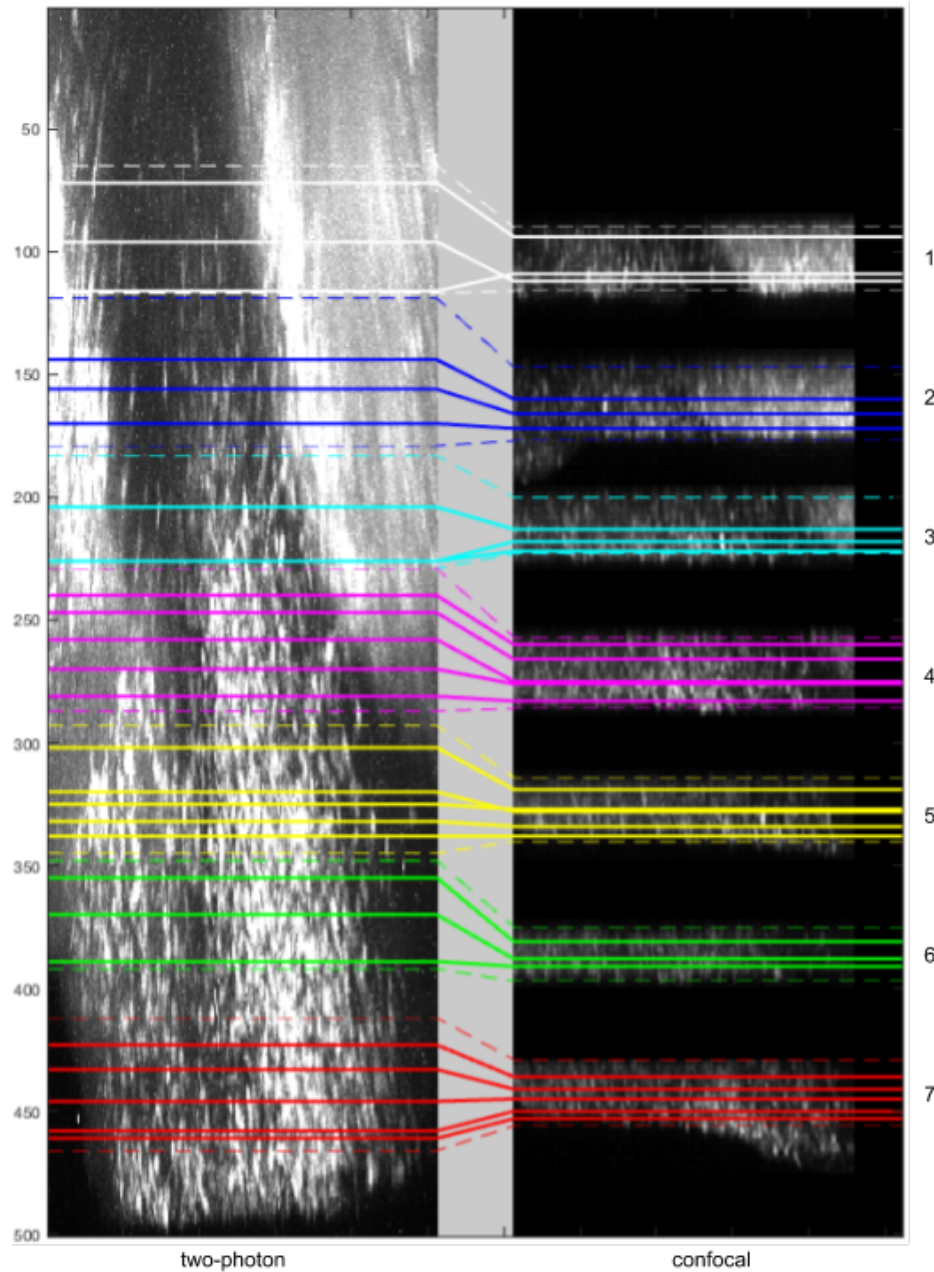


Figure 6.5: Maximum intensity projection of 7 confocal sections (right) mapped to the two-photon image (left) of the same region before sectioning. The mapping was established with the aid of 56 manually chosen landmark pairs that identify corresponding anatomical points in the two acquisitions. The solid colored lines show the placement of corresponding landmarks (note that a single line might represent multiple landmarks in the same slice). The dashed lines show the mapping of the tissue section boundaries from the confocal sections to the two-photon volume. The landmark mappings reveal a 50% decrease in thickness after sectioning, staining, mounting, and imaging. In addition to shrinkage, the mapping shows a 2, 4, 0, 6, 3, and 20 μm gap between tissue sections in the two-photon volume (from top to bottom).

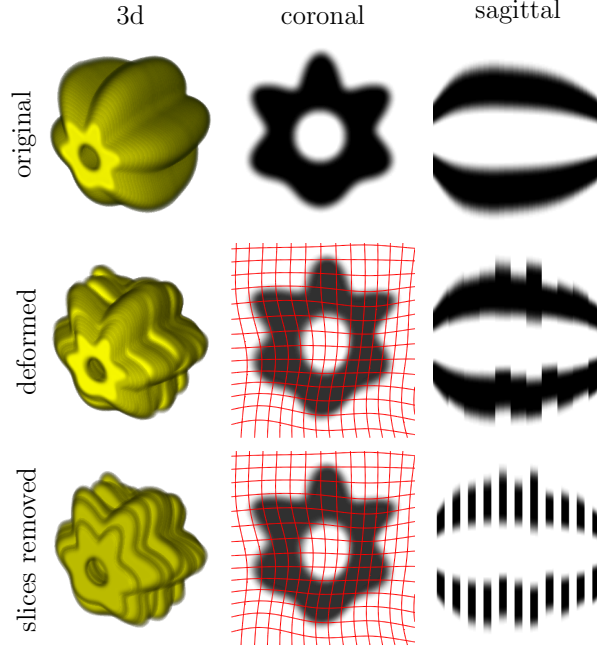


Figure 6.6: Synthetic serially-sectioned dataset. *Top row*: toy data in 3D and with 2D cross sections. *Middle row*: the mechanical distortions introduced by sectioning are simulated by adding random deformations to each section. *Bottom row*: tissue loss during sectioning is simulated by removing slices at the section boundaries.

Instead of relying on the appearance of the sections for registration, the proposed method uses only the shape of the tissue sections. The shape of the sections is estimated by acquiring the tissue mask of each slice via image segmentation. However, segmenting each slice in a section is problematic, due to yet another set of acquisition artifacts which result from the uneven mounting of the sections and the optical limitation of the microscope to image a sample near the glass coverslip. Figure 6.8 shows a set of slices from a single tissue section. In addition to the secondary deformations, mounting artifacts can also include bubbles, debris (Ju et al., 2006), regions of high or low intensity, and tilting. The optical limitation of the microscope shows up as low contrast and low intensity at the boundary slices. Both types of artifacts make segmentation near the tissue boundaries unreliable. To compensate for these artifacts, the segmentation was performed on the maximum intensity projection image of each section and copied the other slices. This is a reasonable simplification, as the shape of a tissue section changes little across slices; note that the sections are considerably thinner at the time of imaging than the original $50 - 70\mu m$ thickness after sectioning, for the reasons described in Section 6.1.1. In order to illustrate the consistent shape through a tissue section, Figure 6.9 shows the through-plane maximum intensity projection of a section (N04, section 17) and the contour of its tissue mask overlaid on the boundary

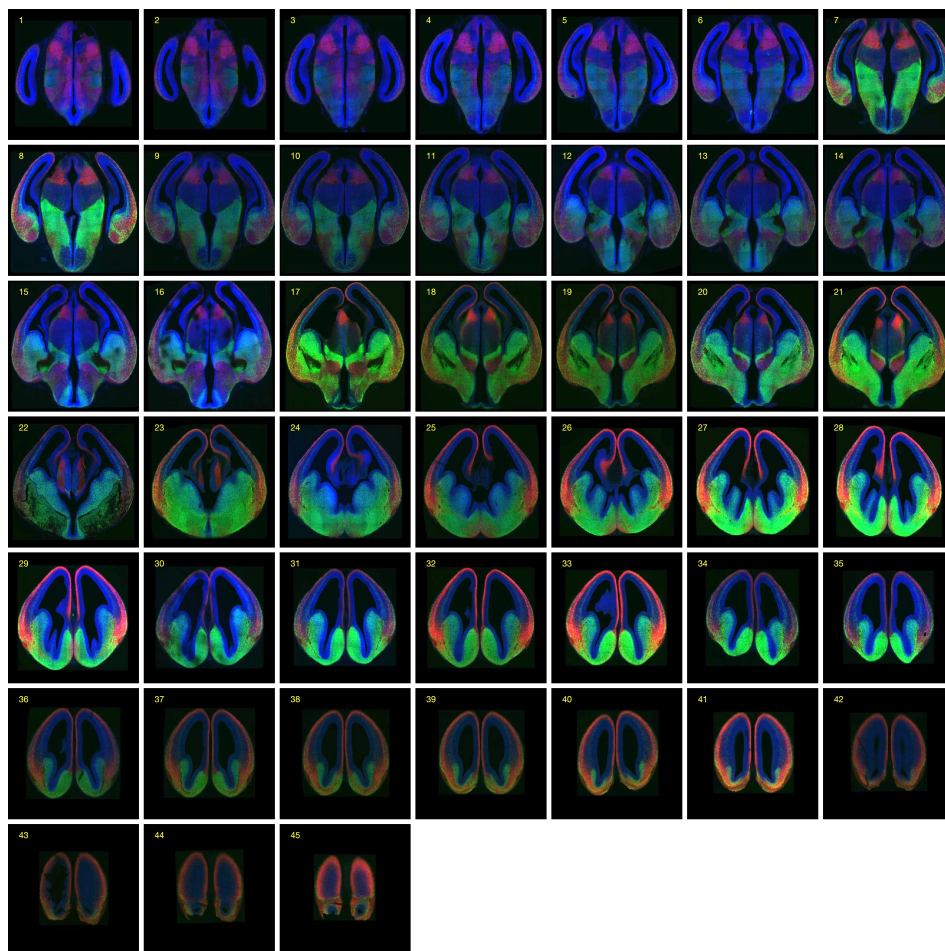


Figure 6.7: Through-plane maximum intensity projection of the 45 sections of the N04 dataset. The sections were manually ordered and oriented. The orientation step included flipping sections that were incorrectly mounted and aligning the centerlines of the sections. The sections were also cropped to the bounding box of the largest section. Note the large variation in the intensity distribution of the channels. Sections that were mounted on the same slide and imaged together appear more similar than sections on different slides.

slices of the same section. Note that the contour matches the shape of the boundary slices, indicating that the shape of the section does not change considerably across the slices. Low contrast, tilting, and debris are also visible in the boundary slices.

6.2.1 Manual Preprocessing

The 3D reconstruction process requires the series of sections to be in the correct order and approximate orientation. The sectioning workflow mostly preserved the order and orientation of the sections; however, all of the series required some manual reordering and flipping of the sections. The manual

correction was performed in image space after the acquisition. The quality of the images was also inspected during the ordering step, and three datasets (N01, N11, F13) with poor quality or missing channels were excluded from further analysis. Furthermore, the centerline dividing the hemispheres and the bounding box in the x-y plane of the tissue samples were also manually determined, using the 2D through-plane maximum intensity projection image of each section. The centerlines and bounding boxes were used for the initial alignment.

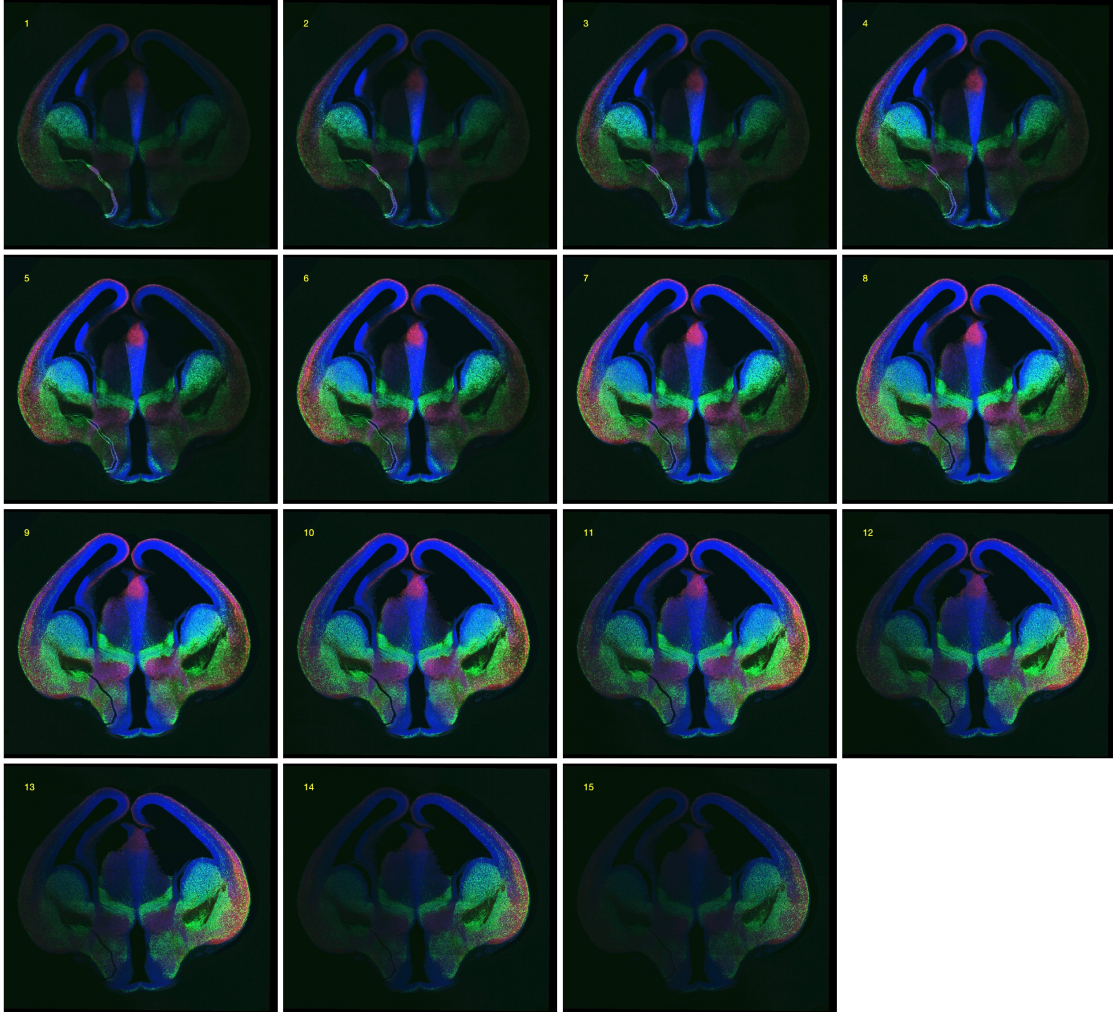


Figure 6.8: Optical slices from a single tissue section (dataset N04, section 17). A number of artifacts are present in the slices, including uneven mounting, debris, and poor contrast near the boundary slices.

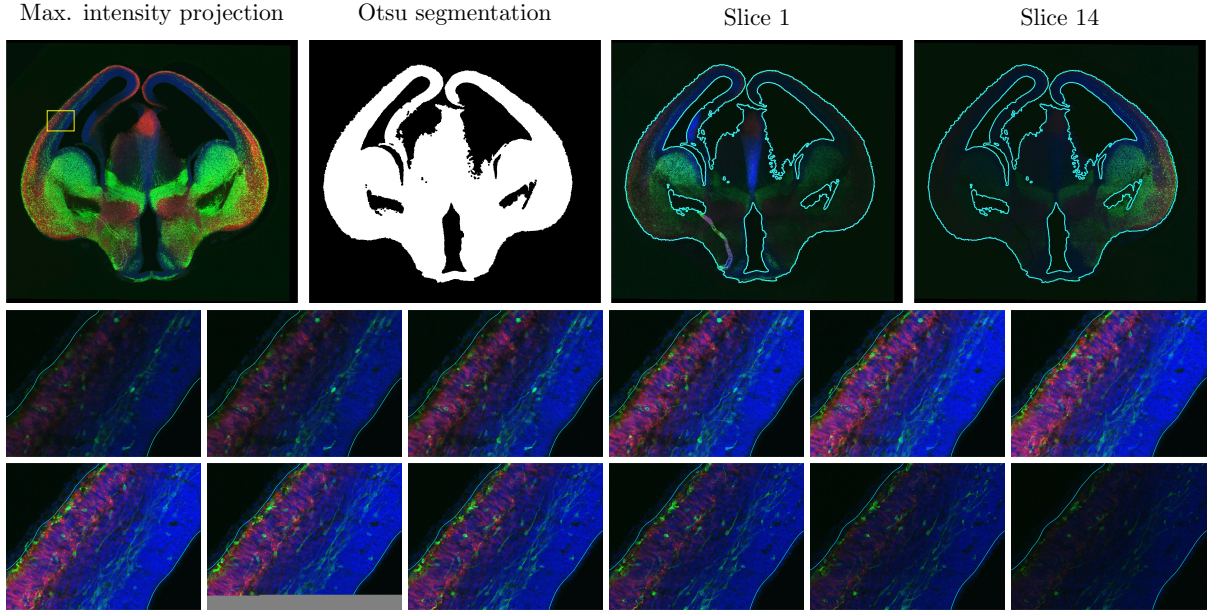


Figure 6.9: Figure illustrating the match between the tissue mask (second image) obtained from the through-plane maximum intensity projection of the channels (first image; the segmentation process is described in Section 6.2.3) and the boundary slices of the sections (right images; the tissue mask contour is overlaid in cyan). The bottom two rows show a magnified region (yellow square) of all the slices where the tissue is visible; however, the first and last slices are not in focus. The outline of the tissue mask is overlaid on the region. Given the 10 slices in focus with $1.2\mu m$ thickness, the imaged section is $12\mu m$ thick, which is only 24% of the $50\mu m$ vibratome setting.

6.2.2 Intensity Normalization

The appearance of the maximum intensity projection of the sections varies considerably, due to variations in the staining, mounting, and imaging processing (Model and Burkhardt, 2001). The sections contain different anatomies and do not have the same intensity distribution—histogram equalization or histogram matching are not appropriate. Instead, each of the three channels is uniformly normalized to the same 98th percentile intensity value across all datasets. Figure 6.10 shows axial slices of the N02 dataset before and after normalization.

6.2.3 Segmentation

The shape of the brain was estimated by stacking the tissue masks of the individual sections. The tissue masks were obtained through segmenting the through-plane maximum intensity projection of each channel, using adaptive thresholding (Otsu, 1979) and combining the per channel, masks into a single tissue mask using a bit-wise OR operator. The thresholding was performed per channel since

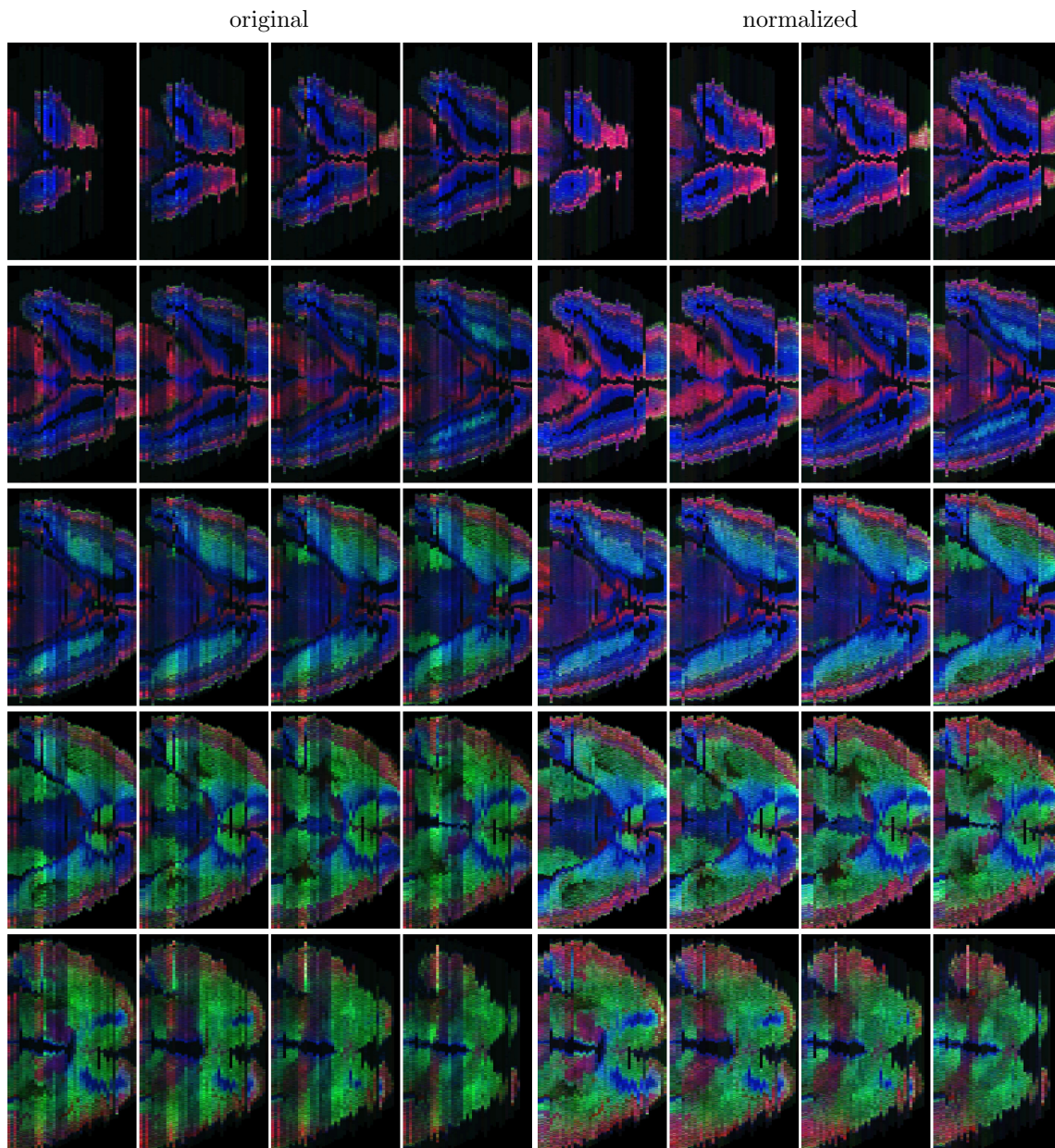


Figure 6.10: Tissue section intensity normalization for each fluorescence microscopy channel: interneurons (green), projection neurons (red), and cell nuclei (blue). To remove the intensity variability between sections, all sections across the datasets are normalized to have the same 98th percentile intensity per channel. The group of images on the left shows axial slices of the sections without intensity normalization. The sections have been manually ordered and oriented. The jagged anatomical structures result from the uncorrelated secondary deformations. The group of images on the right shows the same set of axial slices after normalization. The fluorescent signal becomes more homogeneous across the slices after normalization.

the algorithm assumes a bi-modal intensity distribution—an assumption that no longer holds for the combined grayscale image of all channels. Morphological closing (structuring element: disk with 5 pixel

radius) was applied to the final tissue mask to remove small debris from the background and small holes from the mask, respectively. Figure 6.11 shows the tissue masks for the 45 sections of the N04 dataset.

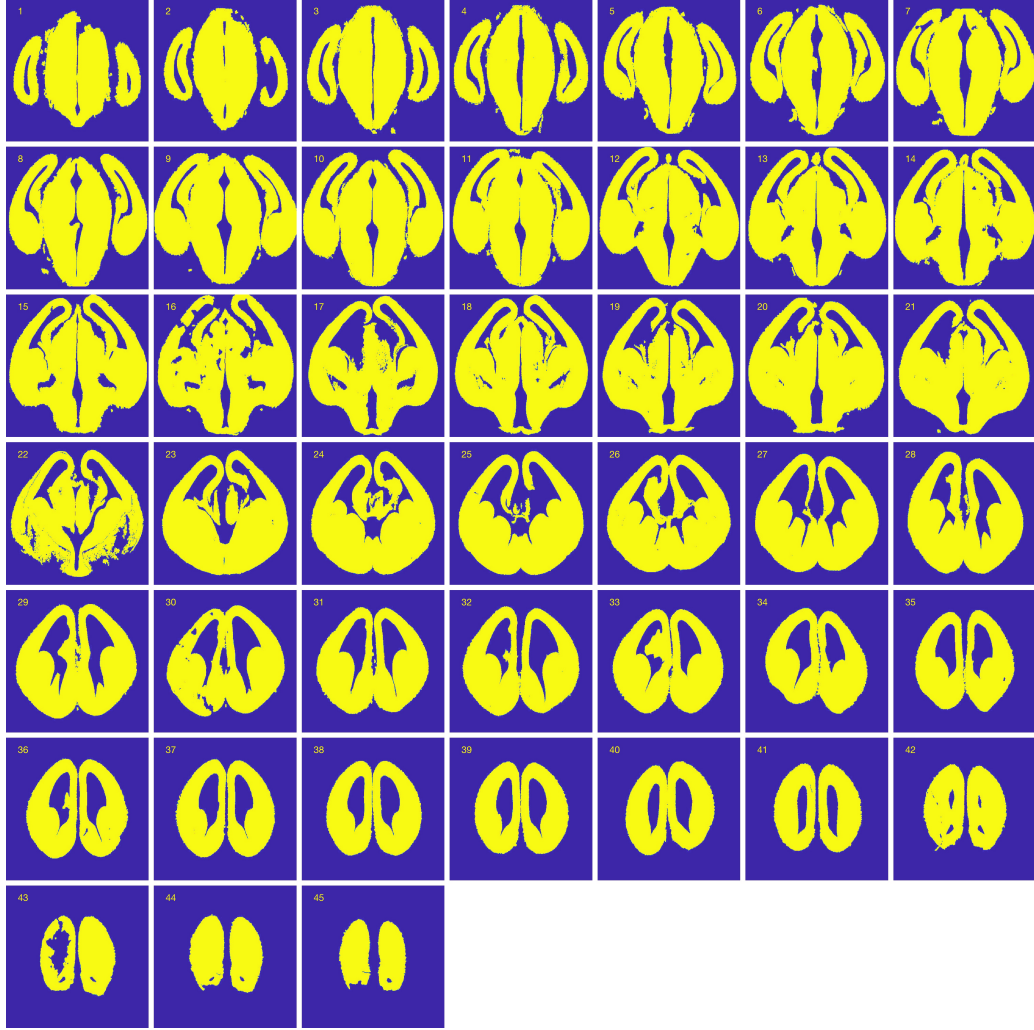


Figure 6.11: The tissue masks for the N04 dataset sections. The masks were obtained by segmenting the through-plane maximum intensity projection of each channel, using adaptive thresholding (Otsu, 1979) and combining the per channel masks into a single tissue mask.

6.2.4 Stacking

The manually ordered and aligned tissue masks (one per section) were downsampled to 512×512 pixels for the reconstruction. Due to the large variability of tissue shrinkage and gap size, the single slice tissue masks were stacked to approximate the $50 - 70\mu m$ thickness set for the vibratome. For the E14 brains, the downsampling yielded an $7\mu m$ isotropic voxel size, resulting in 7 slices per section (giving

49 μm sections). Similarly, the downsampling gave 9 μm and 11 μm voxel sizes and 6 and 5 slices per section for the E16 and E18 brains, respectively.

6.2.5 Reconstruction

After the initial manual preprocessing, alignment, and stacking, the 3D reconstruction algorithm aims to remove the secondary deformations from each section without an external template. Figure 6.12 illustrates the preprocessing steps and the reconstruction. Given an intact mouse brain, I^k , where k is the index of the dataset, the sectioning results in n consecutive sections, I_i^k for $i = 1, \dots, n$. Segmentation and stacking give n tissue masks, $M_1^k \dots M_n^k$, corresponding to each of the sections.

The reconstruction method takes a series of tissue section masks and uses an iterative algorithm with two steps:

1. Given the stacked tissue section masks of a dataset k , $M_1^k \dots M_n^k$, estimate a coherent 3D shape, \hat{M}^k from the stack that approximates the original shape of the intact brain before sectioning.
2. Register each of the section masks, M_i^k to their corresponding sections, \hat{M}_i^k , in the estimated 3D volume using deformable elastic registration.

The method converges when each tissue section, M_i^k , matches its corresponding section from the estimated 3D volume, \hat{M}_i^k , within a given threshold. The match is measured by the sum of the magnitude of the deformation field at the given iteration.

The shape estimation step exploits the fact that the brain anatomy changes smoothly across sections, while the secondary deformations are independent and uncorrelated between sections. The shape estimation is done by smoothing the stacked tissue masks with a 3D Gaussian operator ($\sigma = 20$). By smoothing the stacked tissue masks I can estimate the smooth shape of the intact brain, which in turn can be used as a "regularized" registration target. The smoothing also ensures that the target section is estimated from not only the corresponding section, but the neighboring sections as well.

The deformable image registration was performed with the FAIR toolbox (Modersitzki, 2009), using the elastic regularizer described in Section 3.2.1 (with $\mu = 1$ and $\lambda = 0$) with the SSD similarity measure ($\alpha = 5000$). The parameters were experimentally chosen to allow large smooth deformations without folding.

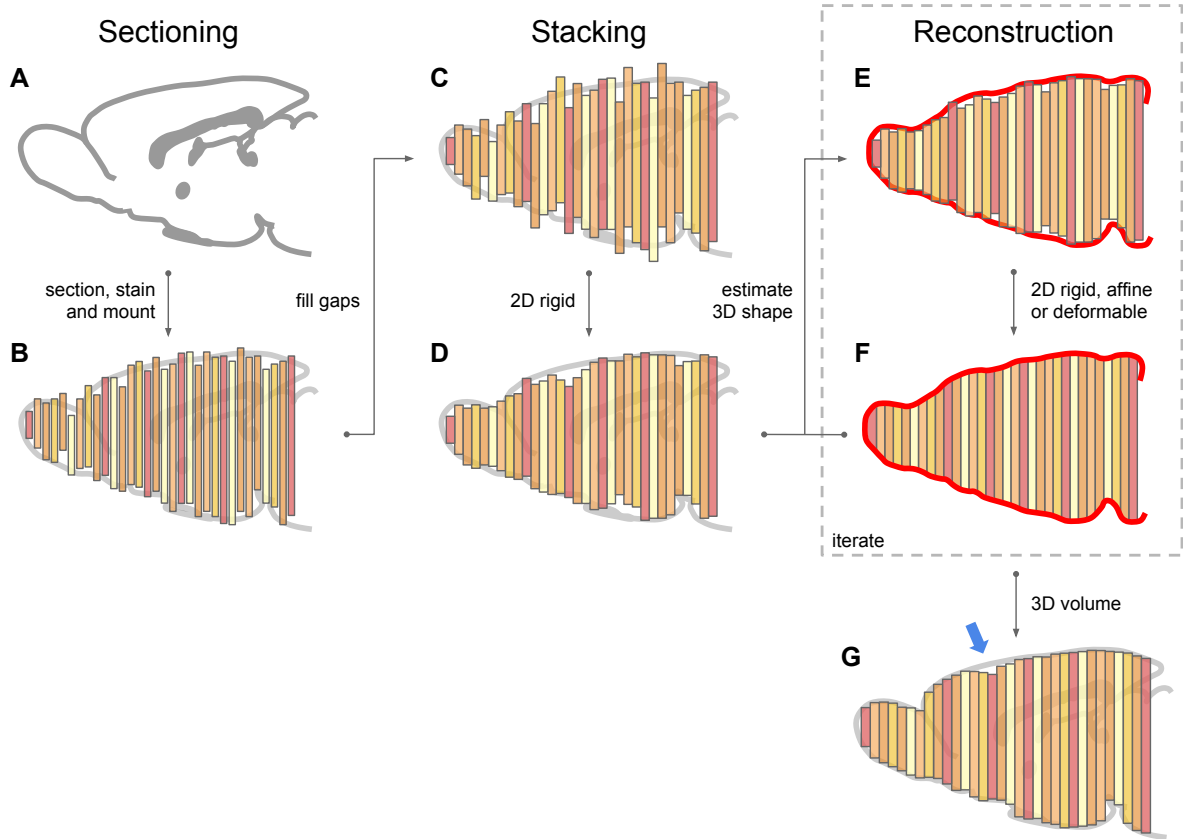


Figure 6.12: 3D reconstruction. The excised and prepared embryonic brain (A) is sectioned into $50\ \mu\text{m}$ sections using a vibratome. Sectioning and mounting introduce secondary deformations, tissue loss and tissue shrinkage, and the stacked sections do not resemble the anatomical structure of the brain (B). First, a tissue mask is acquired via automatic segmentation of the fluorescent microscope images; the tissue loss (measured in Section 6.1.1) is mitigated by duplicating the segmented images at the section boundaries (C). At this stage, the images within a section represent the tissue mask of the section with approximately the correct thickness. However, the sections might be flipped and out of order, and they are not aligned to the neighboring sections. Next, the sections are manually flipped and reordered, if necessary, and are aligned to the neighboring sections using 2D rigid registration (D). The secondary deformations are estimated through an iterative reconstruction process. First, the shape of the whole brain is estimated by blurring the stacked tissue masked images (E). Next, the tissue mask images are registered to the corresponding slices from the estimated 3D brain mask (F). A new 3D brain mask is estimated from the registered images and the process is repeated until convergence. The final transformation for each section is then applied to the fluorescence microscopy images (G). The reconstruction algorithm aims to remove secondary deformations only; incidental artifacts, such as tearing (blue arrow), remain in the final 3D volume.

6.3 Experimental Results

In order to assess the feasibility of the reconstruction method, it was first applied to a synthetic 3D dataset. Next, the serially-sectioned embryonic brains, described in Section 6.1, were reconstructed.

6.3.1 Reconstructing 3D Synthetic Data

The validation of the reconstruction method was performed with a set of synthetic 3D datasets. Using synthetic data allows the comparison of the reconstruction results to a known ground truth.

The 3D synthetic volume, shown in Figure 6.6, is a tubular shape with six lobes and smoothly varying cross-sectional area along the z-axis. The synthetic data resembles the tissue mask that is used for the reconstruction of a real mouse confocal fluorescence microscopy dataset. The 3D volume has 256×256 voxel in-plane resolution and consists of 132 slices divided into 11 sections of equal thickness (giving 12 slices per section). Two additional steps are performed, in order to make the synthetic dataset similar to the data generated after the mechanical sectioning and imaging of a typical real mouse brain:

1. A random transformation is applied to each of the sections to simulate the independent secondary deformations resulting from the mechanical stresses. The random transformations are generated from an identity spline transform (that produces no deformation) with 4×5 equally spaced control points. Each of the 20 control points is perturbed in both the x and y directions by a small distance drawn from a normal distribution (with $\mu = 0$, $\sigma^2 = 0.2$), and the resulting transformation is applied to all slices of the section (see the middle row of Figure 6.6).
2. Four out of the 12 slices are removed from each section (two slices at each tissue boundary) to simulate tissue loss and shrinking of the sections (see bottom row of Figure 6.6).

6.3.1.1 Experiment

The proposed method is validated against a common approach, used with reference-free reconstruction algorithms where sections are registered directly to neighboring sections:

1. Given a synthetic volume, $I_{i,j}^k$, where k is the index of the dataset, $i = 1, \dots, 11$ is the index of the section, and $j = 1, \dots, 12$ is the index of the slice within a section, choose a target section, $I_{t,\cdot}^k$. For this experiment, the middle section $t = 6$ is used as the target.
2. Register the boundary slices of the two neighboring moving sections to the boundary slices of the target section: $I_{t-1,12}^k$ to $I_{t,1}^k$ and $I_{t+1,1}^k$ to $I_{t,12}^k$. Apply the resulting transformations to each of the remaining slices in the moving sections.

3. Repeat the previous step for the remaining sections, but using the previous moving sections as the new targets for each iteration, $l = 0, \dots$: register $I_{t-l-1,12}^k$ to $I_{t-l,1}^k$ and $I_{t+l+1,1}^k$ to $I_{t+l,12}^k$.

The method described above is tested, using three types of transformation models: rigid, affine, and deformable with elastic regularization. The aim of the experiment is to recover the original shape of the sections, using the proposed method and the three variants of the reference-free approach described above. The performance of the four methods is measured by the sum of squared differences (SSD) similarity measure between the reconstructed sections and the original ground truth volumes (both including tissue gaps). The closer the reconstructed sections match the ground truth sections the lower the resulting SSD measure.

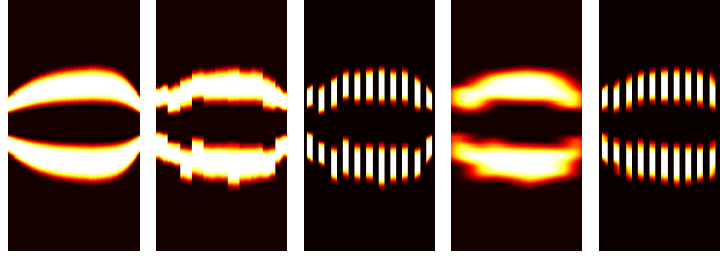


Figure 6.13: Sagittal cross sections of a serially sectioned 3D synthetic dataset and its reconstruction with Gaussian smoothing. *Left to right*: original dataset; deformed sections; simulated tissue loss; shape atlas with smoothing; final reconstruction.

Each experiment was repeated 100 times for each transformation model, with different random deformations giving a total of 400 reconstructed volumes. Figure 6.13 shows the cross section of the synthetic dataset and the result of the proposed reconstruction algorithm for a single experiment. The figure illustrates a typical result of the proposed method: while a number of the secondary deformations are severe, the estimated shape of the dataset, and consequently the reconstructed sections, resemble the original intact dataset. Figure 6.14 shows a comparison between the four tested methods. The reference-free elastic method generates a smooth reconstruction, but the shape of the reconstructed volume diverges from the original shape towards the distal sections of the synthetic dataset. The proposed shape-based method on the other hand results in a more jagged outline, but one that follows the original shape more closely. These observations are also supported by the boxplot of the SSD similarity measure for all the 100 experiments shown in Figure 6.15. The mean SSD measures for sectioned test dataset and the four reconstruction results (rigid, affine, elastic, and shape-based, respectively) were 2.97, 2.80, 4.62, 4.35, and 1.99. The shape-based method significantly improved the reconstruction (calculated with

a paired-sample t-test at a significance level of $\alpha = 0.01$), while the reference-free methods did not significantly improve reconstruction.

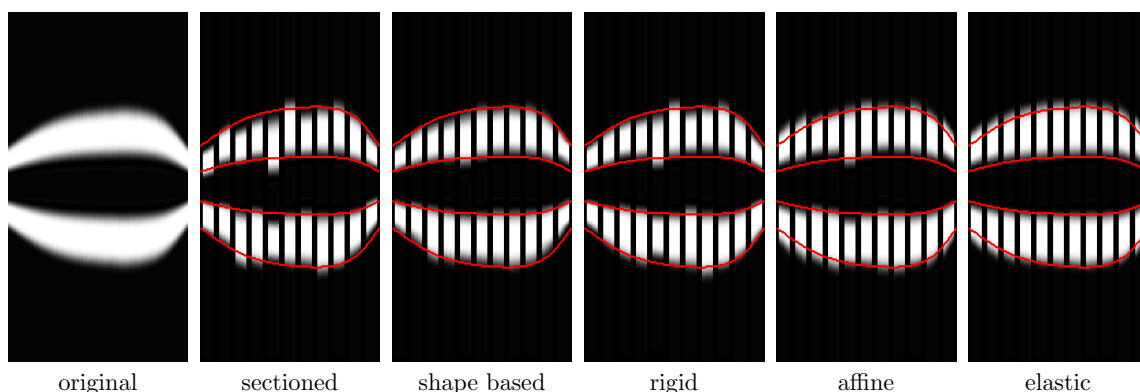


Figure 6.14: Sagittal cross sections of the synthetic 3D dataset and reconstruction results. *Left to right:* original dataset; sectioned dataset to be reconstructed; reconstruction with the proposed method; reconstruction with the rigid, affine, and elastic reference-free methods used for validation. The outline of the original dataset is overlaid in red as a reference. The reconstruction algorithms should produce results that match the outline closely. While the affine and elastic algorithms produce reconstructed sections, the lack of a shape reference results in the distal sections diverging from the original shape.

6.3.2 Reconstructing Confocal Microscopy Embryonic Mouse Data

The reconstruction method was applied to the 10 mouse datasets described in Section 6.1 (3 of the 13 datasets were excluded from analysis). The lack of reference volume obtained by other imaging modalities before sectioning does not allow quantitative analysis of the proposed method on the real datasets. However, the biological plausibility of the resulting brain volumes can be qualitatively evaluated.

Figure 6.16 shows the axial cross sections of the stacked tissue section masks of the sectioned brains before and after 3D reconstruction. The sections before the reconstruction were manually ordered, oriented, and rigidly aligned. The rigidly aligned sections still contain the secondary deformations that appear as jagged anatomy, whereas the reconstructed brains resemble the smooth anatomy of the intact brains before sectioning. Note that other artifacts, such as missing tissue regions, tearing, folding, and overlap between tissue regions that were displaced during mounting are not removed by the reconstruction method and thus appear in the final volume.

Figures 6.17, 6.18, 6.19 and 6.20 show the 3D rendering of the E14, E16, E18, and FAS datasets before and after reconstruction. The reconstructed volumes retained the overall shape of the rigidly

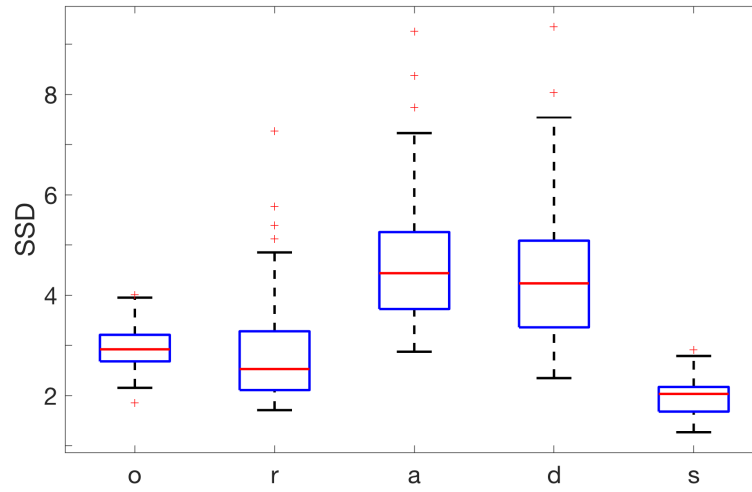


Figure 6.15: Sum of squared difference (SSD) measure between the reconstructed volumes and the original ground truth volume for 100 experiments. *Left to right*: sectioned synthetic volume to be reconstructed (o); reference-free method with rigid (r), affine (a), and elastic (d) transformation models; proposed shape-based method (s). While the rigid reference-free method results in improved reconstruction, the shape-based method produces the best reconstruction results.

aligned tissue section stacks. At the same time, the reconstruction generated smooth anatomy that is plausible for biological tissue.

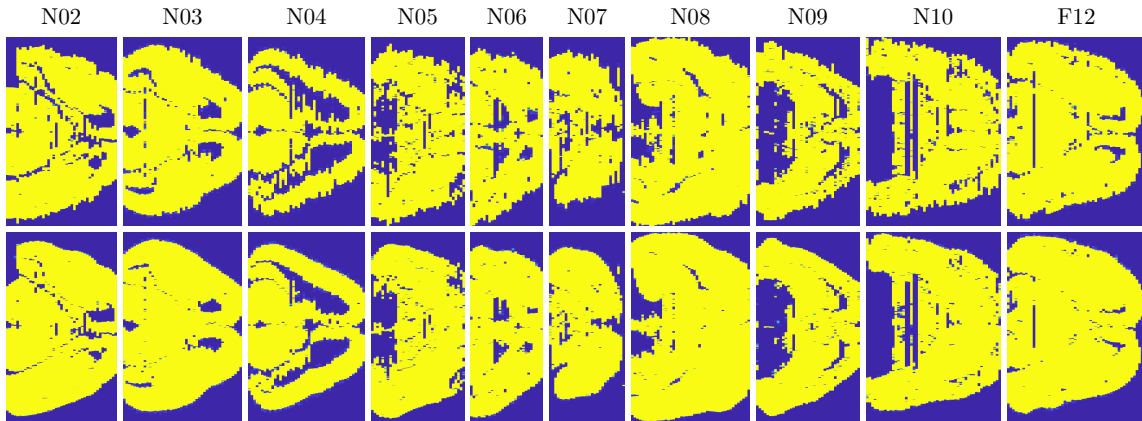


Figure 6.16: Axial cross sections of the stacked tissue section masks of the serially-sectioned embryonic mouse brains before (top row) and after (bottom row) 3D reconstruction. The reconstructed brains resemble the smooth anatomy of the intact brains before sectioning.

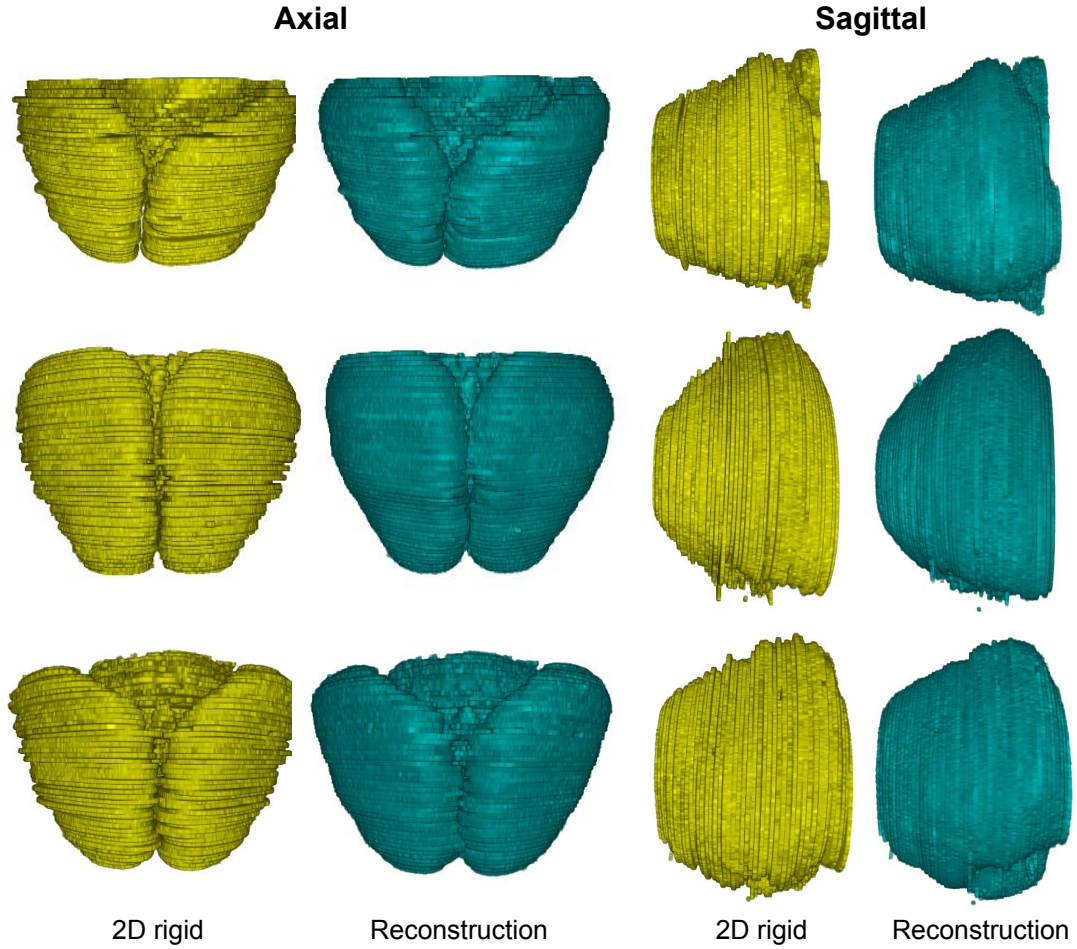


Figure 6.17: Axial and sagittal view of serially sectioned embryonic brains at age E14, with 2D slice-to-slice rigid registration only (yellow), and using the proposed reconstruction method (cyan). The reconstructed brains have a smoother shape and fewer discontinuities than the brains with rigid only registration, while the shape of the reconstructed brains closely resembles the original shape.

6.3.3 Mapping Neuron Migration in the Developing Brain

The aim of the mouse study is to map the spatial and temporal pattern of neuron migration during a critical period of brain development and provide a population summary of neuron migration. Two major populations of neurons are imaged: interneurons that form short distance inhibitory connections, and projection neurons that form long distance excitatory connections. The atlas aggregates information from 10 fixed mouse brains. Figure 6.21 summarizes the mapping steps from the 3D reconstruction of a serially-sectioned dataset to the resulting 3D neuron density map for two populations of neurons. Once the individual neuron density maps are acquired, the densities of the two types of neuron population need to be summarized across time points.

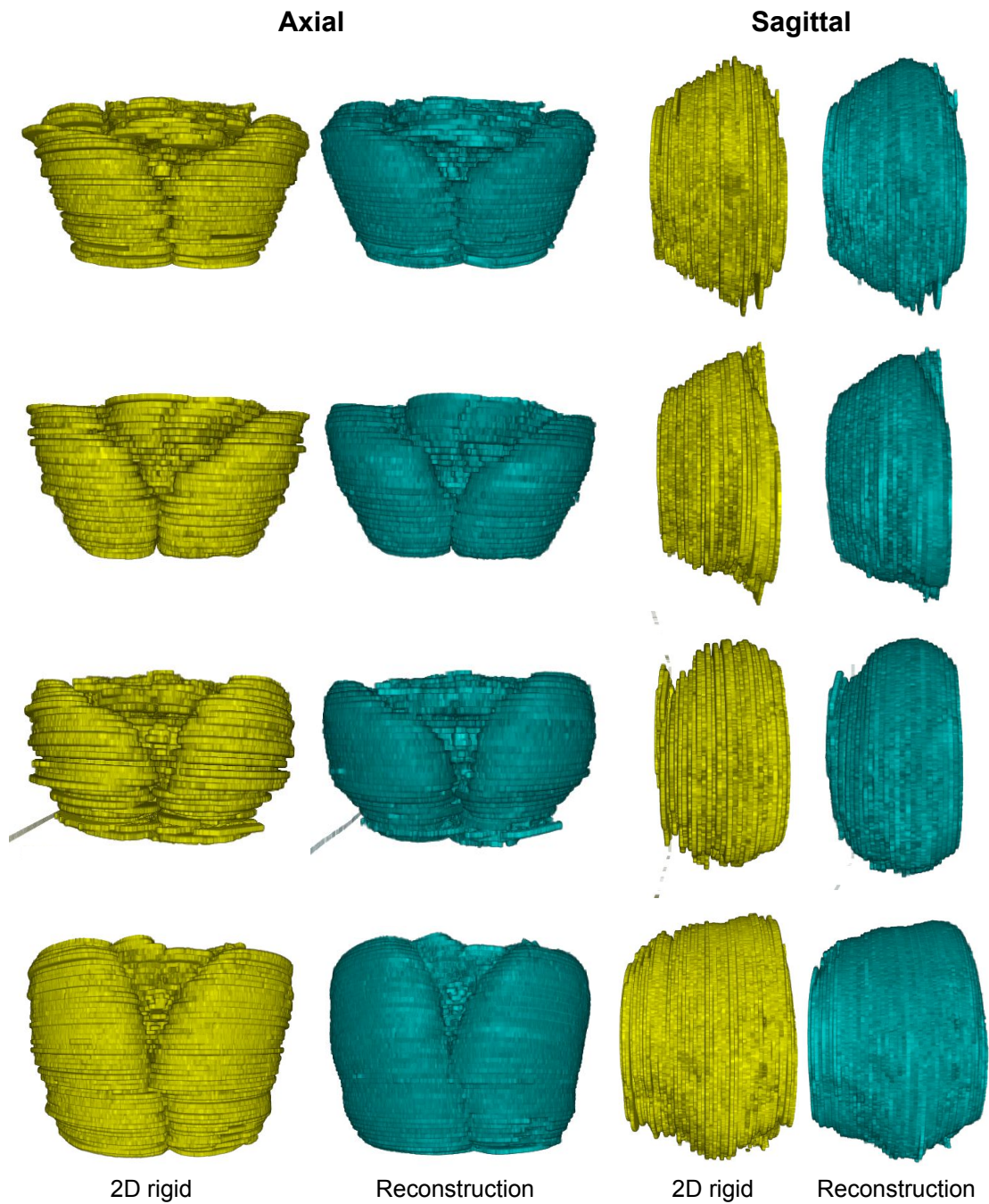


Figure 6.18: Axial and sagittal view of serially sectioned embryonic brains at age E16, with 2D slice-to-slice rigid registration only (yellow), and using the proposed reconstruction method (cyan).

The reconstructed 3D images are aligned to each other to aggregate the neuron migration information in a common coordinate system. As the embryo develops the shape of the brain changes drastically, therefore the registration has to be flexible enough to allow the direct alignment between different time

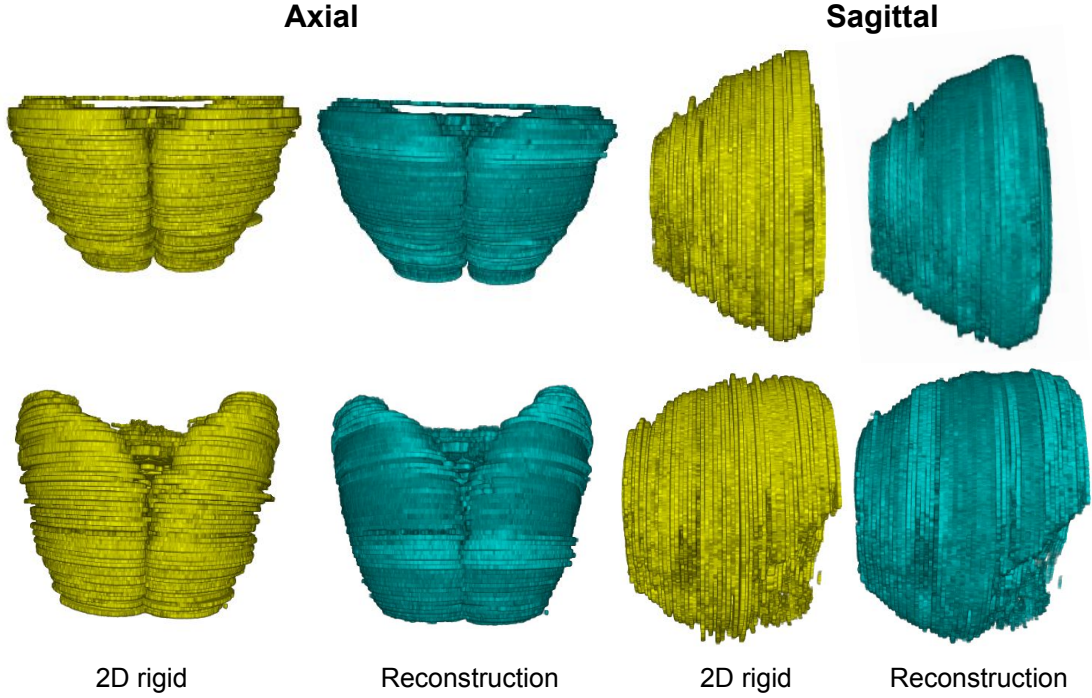


Figure 6.19: Axial and sagittal view of serially sectioned embryonic brains at age E18, with 2D slice-to-slice rigid registration only (yellow), and using the proposed reconstruction method (cyan).

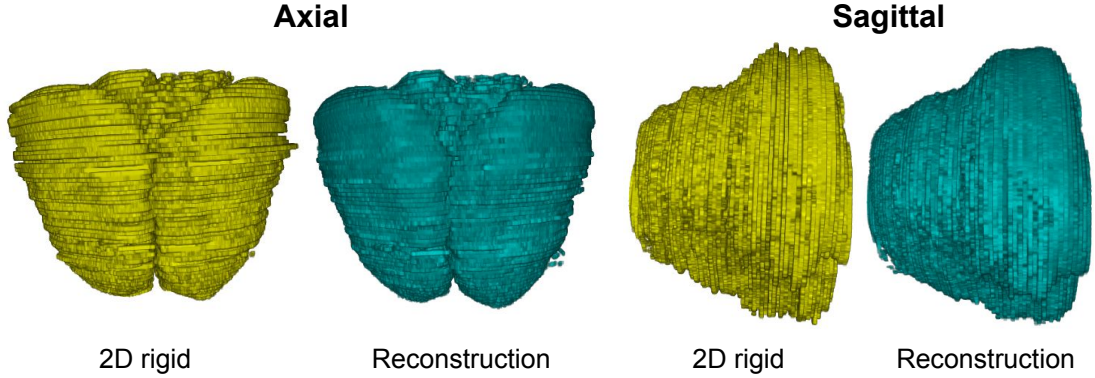


Figure 6.20: Axial and sagittal view of serially sectioned embryonic brains with fetal alcohol syndrome at age E14, with 2D slice-to-slice rigid registration only (yellow), and using the proposed reconstruction method (cyan).

points (2 days apart). To mitigate the effects of the damaged tissue sections and reconstruction errors, the estimated smooth 3D shapes, \hat{M}^k , were used. The target dataset for the registration, N03, was chosen based on the quality of the reconstruction; all other datasets were registered to this target, \hat{M}^{N03} . Figure 6.22 shows the 10 datasets aligned to the common target dataset.

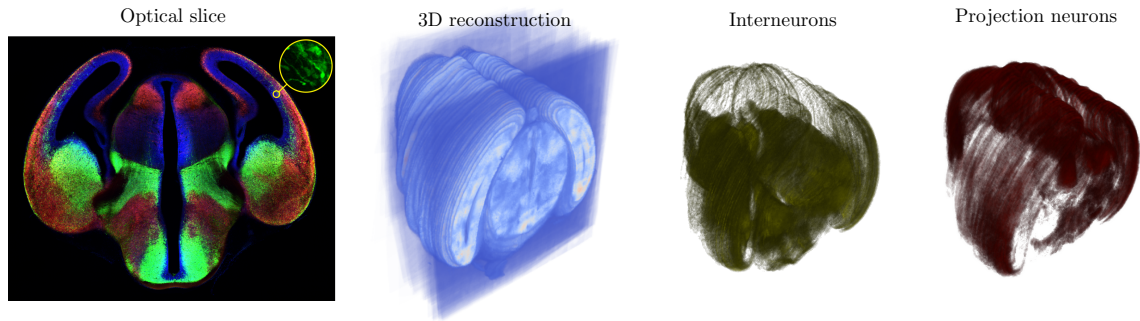


Figure 6.21: Reconstruction results overview (*left to right*): single optical image with 3 channels; 3D reconstruction from sectioned tissue; neuron density from the 3D reconstruction for inter- and projection neurons.

Once the 3D volumes are in a common coordinate system, the spatiotemporal changes in neuron placement and composition were summarized by spatially averaging the neuron densities for each time point. Figure 6.23 shows the aggregated neuron densities for the three time points (E14, E16, E18) and the single brain with fetal alcohol syndrome (FAS). The aggregate maps reveal some expected trends clearly for both neuron populations. Interneurons (green) are predominantly generated near the ganglionic eminence (GE) and migrate tangentially along the cortical plate. The interneuron migration appears as a green cluster at the E14 time point and diffusing throughout the cortical plate in the subsequent time points, E16 and E18. The radial migration of the projection neurons, from their place of birth near the ventricular zone (VZ) to the cortical plate, exhibits more subtle patterns that are better visualized in the cross section views of Figure 6.24. The projection neurons are first placed near the outer surface of the cortical plate (seen as a thin red region at E14), then fill in the deeper layers (the thin red region expands inward in later time points).

6.4 Conclusions

I proposed a template-free 3D reconstruction method for serially-sectioned fluorescence microscopy images. The reconstruction method uses the estimated shape of the intact brain as a regularized reference for the individual tissue sections. The proposed method was applied to 10 sectioned embryonic mouse datasets in an effort to map the patterns of neuron migration in the developing mouse brain. The reconstructed datasets were mapped into the same coordinate system to aggregate the densities of two distinct neuron populations. The aggregate neuron density maps show the patterns of neuron migration over time.

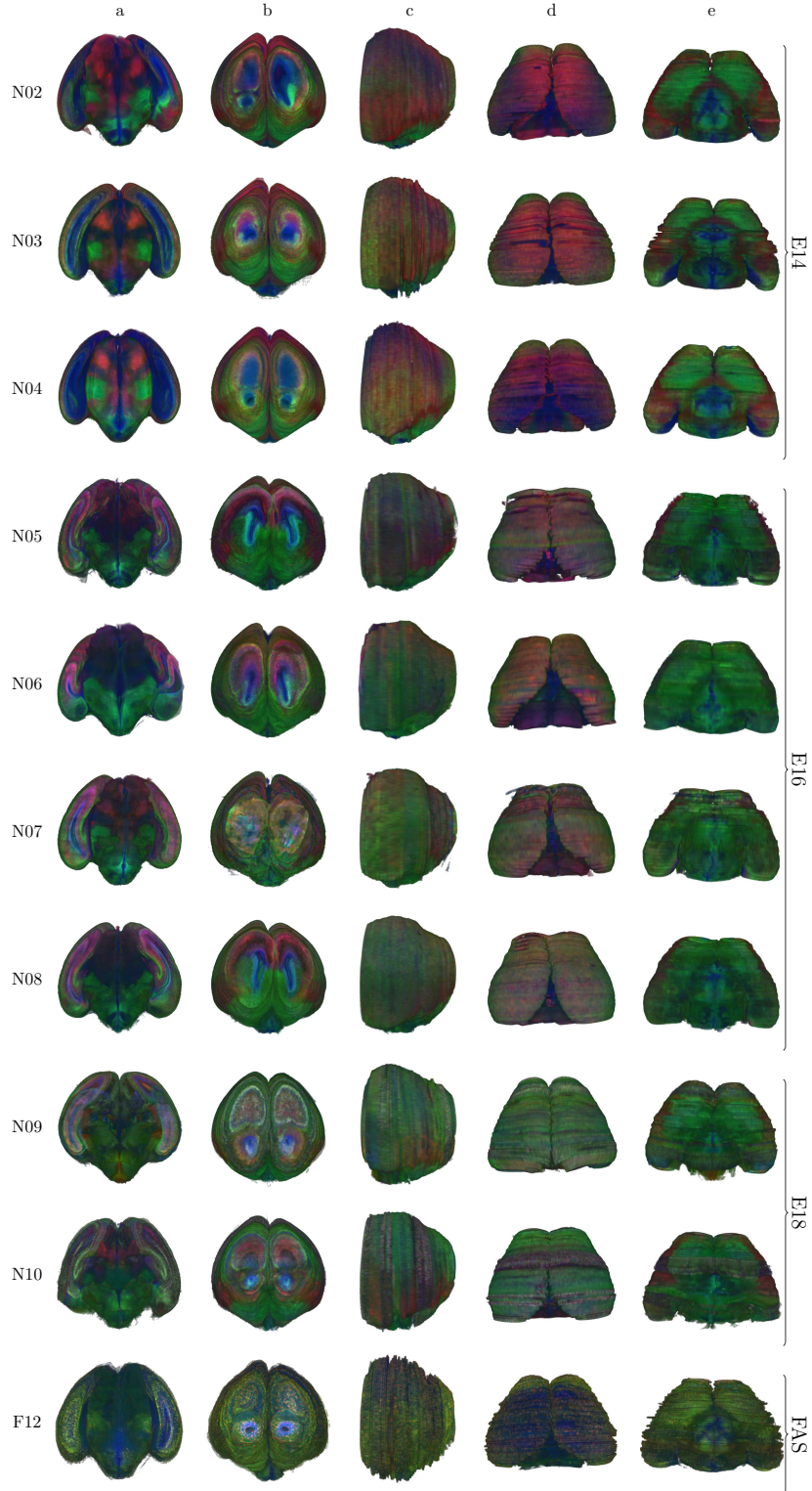


Figure 6.22: 3D reconstructions of the 10 fluorescence microscopy datasets are mapped into a common coordinate system. The reconstructed 3D volumes were not directly registered, but the smooth estimate of their shape from the reconstruction step was used instead. The target dataset, N03, was chosen based on the quality of the reconstruction. The consistency of the distribution of the two neuron populations, interneurons (green) and projection neurons (red), is clearly visible within the first two time points, E14 and E16. For the E18 and FAS images, the neuron distributions are expected to be more diffuse.

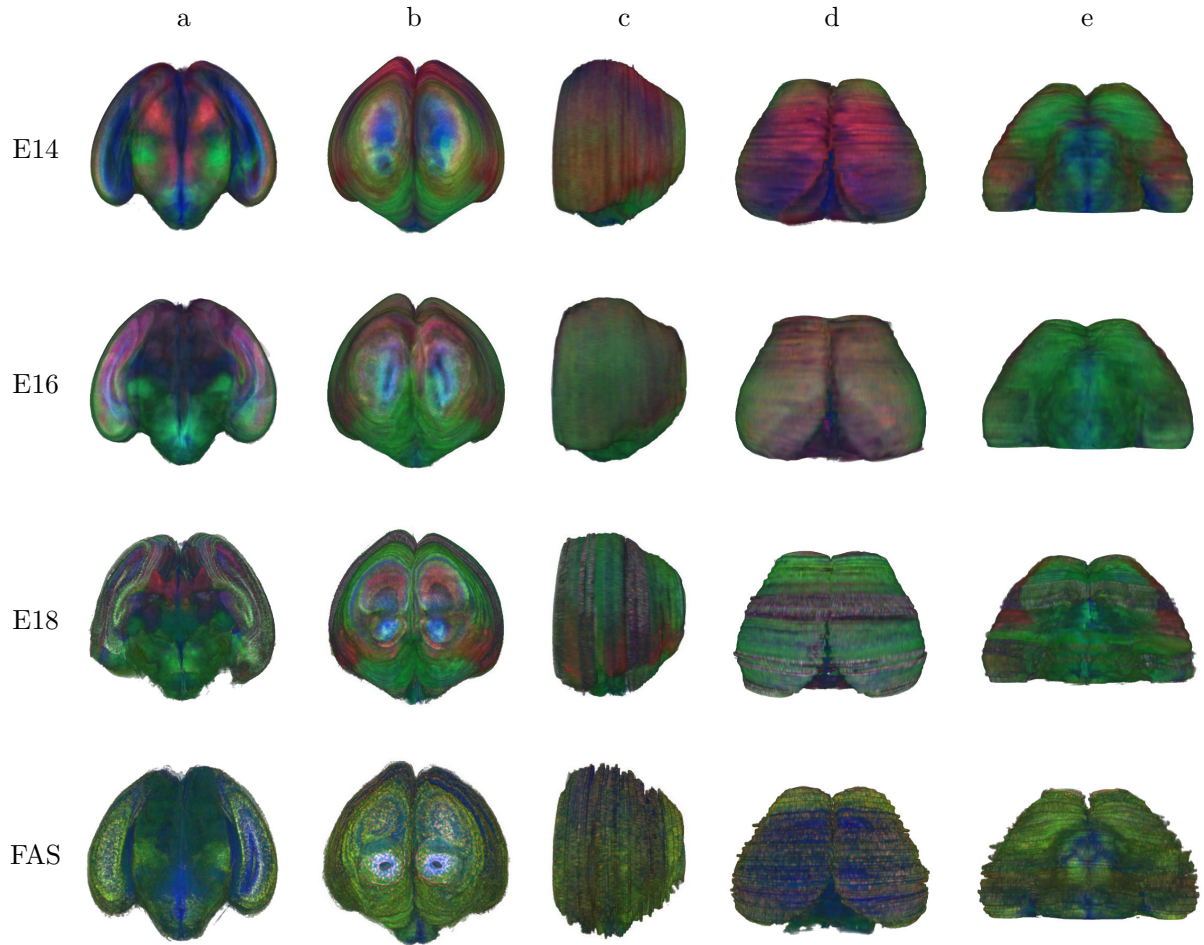


Figure 6.23: 3D volumes of aggregate neuron densities per time point. The maps reveal neuron migration trends over time for both neuron populations: interneurons (green) and projection neurons (red). The DAPI stained cell bodies are shown in blue. The interneurons are predominantly generated near the ganglionic eminence (GE), cluster of green points seen in column *a* and *e* of the *E14* row, and migrate tangentially along the cortical plate, seen as diffusing green points in subsequent time points. The projection neurons migrate radially from their place of birth near the ventricular zone (VZ) to the cortical plate (not readily visible in the volumetric renderings).

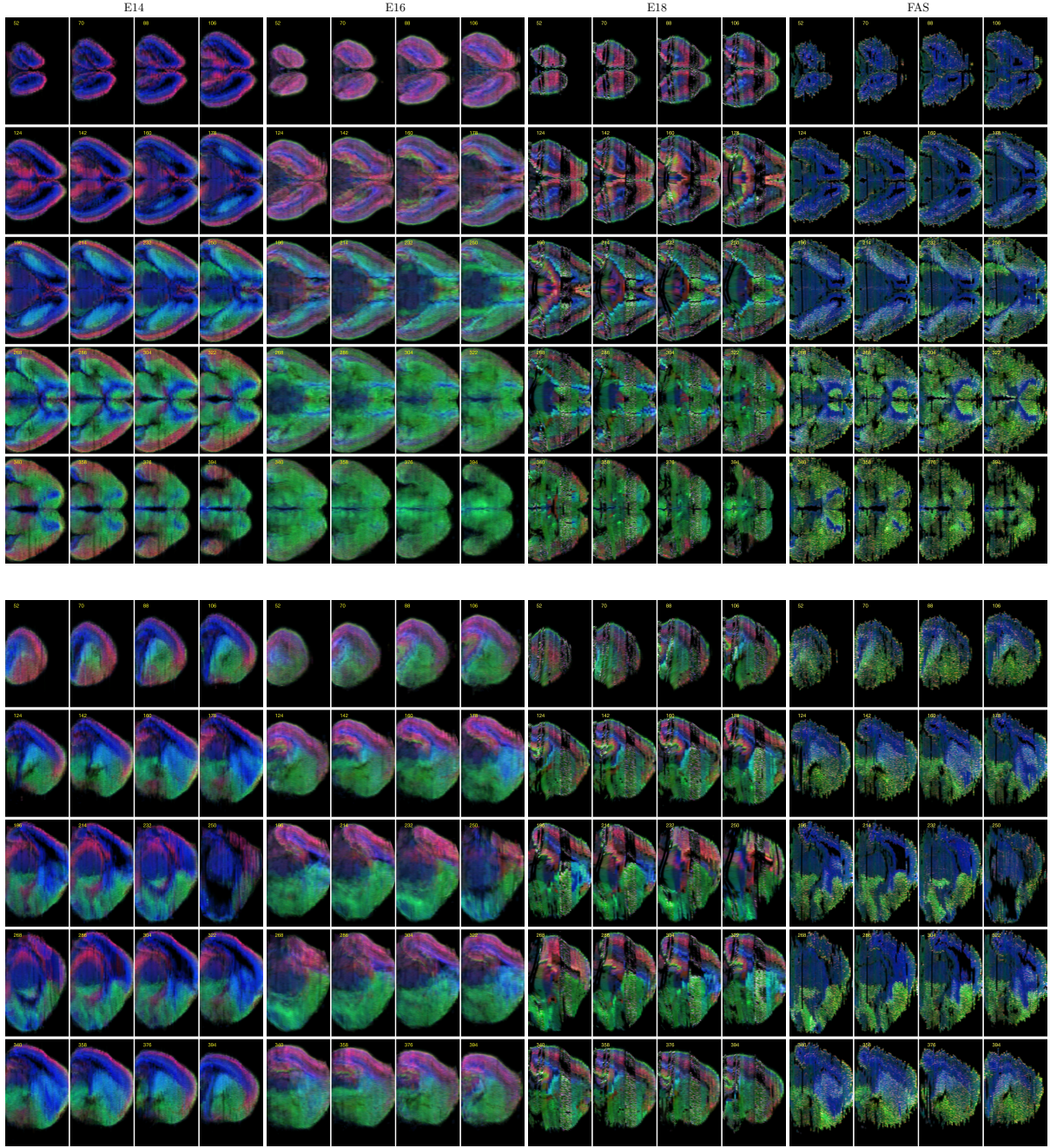


Figure 6.24: Cross-sectional views (*top rows: axial; bottom rows: sagittal*) of the aggregated 3D neuron densities within time points. The patterns of migration for interneurons (green) and projection neurons (red) are visible for the E14 and E16 time points. The quality of the aggregate maps is poor for the E18 and FAS datasets, caused by the lower quality of the reconstruction step compared to the earlier time points.

CHAPTER 7

Discussion

7.1 Summary of Contributions

This section reviews the thesis statement and how each of the claims introduced in Chapter 1 is addressed in the dissertation.

1. *I propose a novel similarity metric, called the sum of squared residuals (SSR), that enables the registration of longitudinal image sequences with large appearance changes.*

The similarity measure, presented in Chapter 3, incorporates a time-dependent appearance model into the registration framework. The appearance model is estimated from a sequence of longitudinal images, and it is subject specific. Once the model is estimated, it is used to generate a new set of target images that match the appearance of each of the moving images, but have the same geometry as the original target image. The moving images then can be registered to the intensity-adjusted target images, effectively removing the appearance change, for a good model.

The proposed similarity metric is tested against the commonly used NCC and MI on both synthetic and real datasets. The results show that SSR outperforms the standard measures in the presence of appearance changes over time with strong intensity gradients.

2. *I build a population atlas that characterizes the appearance changes over time of a rhesus macaque monkey population during early postnatal development.*

The parameters estimated with SSR for individual subjects capture the local properties of myelination. However, these observations from individuals can be used to characterize brain maturation more broadly in a population. In Chapter 4, I build a maturation atlas from the parameters of the model-based similarity measure for each subject. The atlas is defined only in the white matter mask of the latest time point. The logistic model is used as the temporal intensity model for each

voxel, with the additional benefit of biologically meaningful parameters that characterize the onset and rate of myelination.

The atlas shows patterns of brain maturation similar to derived patterns from previous histological and MR studies. The atlas is also used in Chapter 5 as a prior to aid longitudinal registration with missing time points.

3. *I incorporate a population maturation atlas, as a prior into the model-based similarity metric, to better guide the deformable registration for longitudinal datasets with missing time points.*

In Chapter 3, I showed that SSR performs well for registering longitudinal image sequences of brain development. However, the parameter estimation becomes unreliable if the number of images in the longitudinal dataset is low—a common problem for longitudinal studies where not all images can be acquired. One approach to account for missing time points, during the parameter estimation step, is to include prior knowledge about the model parameters into the model. In Chapter 5, I reformulate SSR to include the population atlas as a prior. The prior is weighted such that its influence diminishes as the number of available time points increases.

The proposed method, called SSRP, was evaluated on synthetic and real datasets with missing time points and showed significant improvements compared to SSR, as the number of missing time points increased. SSRP, therefore, can reduce the number of image sequences that need to be excluded from analysis in longitudinal studies.

4. *I present a novel method for reconstructing serially-sectioned fluorescence microscopy images without an external template.*

In order to study brain development at the resolution of individual neurons, fluorescence confocal microscopy is commonly used. However, it requires sectioning the brain into thin tissue sections that need to be reassembled into a coherent 3D volume after imaging. The reconstructed volume should resemble the geometry of the intact sample before sectioning. In Chapter 6, I develop a 3D reconstruction method for serially-sectioned samples that does not rely on external references, or on the use of an imaging modality with dense structural information—two conditions that many commonly used reconstruction methods rely on.

The method is evaluated on synthetic images and used to reconstruct serially-sectioned fluorescence microscopy images of embryonic mouse brains. The reconstructed images are then used to generate aggregate neuron density maps that show the patterns of neuron migration over time.

Thesis: *Advanced image registration methods can allow accurate anatomical mapping between images that are dissimilar in appearance or anatomy. Such registration methods are essential for analyzing animal brain development.*

Chapter 3, an advanced similarity measure, SSR, is described as an extension of the standard SSD similarity measure. The new measure incorporates a time-dependent appearance model that allows the registration of longitudinal image sequences with spatially and temporally non-uniform appearance change—images that are dissimilar in appearance. In Chapter 4, SSR is used to study brain maturation in a population of rhesus macaques. The estimated model parameters from SSR are then used to build an atlas that summarizes the rate and onset of white matter myelination. In Chapter 5, the myelination atlas is incorporated into SSR as a prior, allowing the analysis of datasets with missing time points that were previously excluded from analysis.

In Chapter 6, a novel method is introduced to reconstruct a 3D volume from serially-sectioned fluorescence microscopy images without an external reference. The sectioning and imaging process introduces gaps between the tissue sections, producing images that are dissimilar in appearance. The proposed template-free reconstruction method is applied to serially-sectioned images of the mouse embryo. The reconstructed 3D volumes are then used to map the neuron migration patterns over time in the population.

7.2 Future Work

There are several directions for future research that can be further explored. This section will give a brief overview of these directions.

7.2.1 Model-Based Similarity Measure

The model-based similarity measure presented in this dissertation is tested with an elastic regularizer and a logistic intensity model. The logistic model is often used to model biological processes, and it is suitable for the appearance change seen in the MR images of myelination. However, the formulation is general and can be used with any parametric appearance model.

A possible future direction is to investigate what other types of longitudinal registration problems can benefit from a model based similarity measure. As the experiments have shown, the most significant improvement is expected for images that have strong intensity gradients associated with the temporal appearance change of a particular tissue type. Besides MR images of white matter myelination, there are a number of other imaging techniques that produce longitudinal image sequences with appearance change. One such technique is magnetic resonance angiography (MRA), used to image blood vessels by labeling the blood with either a special MR sequence or an injected contrast agent. These MR sequences often produce longitudinal image sequences, as the health of the vessels can be assessed from the progress of the labeled blood through the circulatory system and the diffusion or leaking of the contrast agent into surrounding tissues. The images in these sequences need to be registered; the progressing front of labeled blood produces local appearance changes with strong gradients—exactly the type of appearance change SSR is well suited for.

7.2.2 Atlas of Brain Maturation

The white matter myelination atlas was built from a small number of subjects. One possible improvement over the current atlas is using a larger cohort of the subjects from the same population. The increased number of subjects would allow capturing the general trend in the population with higher confidence.

7.2.3 Template-free 3D Reconstruction

The proposed 3D reconstruction method generates a reference shape from the stacked tissue masks of the sections by smoothing the stack with a Gaussian kernel. The synthetic experiments demonstrated that this simple approach gives reasonably good estimations of the intact reference shape, but it also has some negative side effects. One of the side effects is the straightening of curved shapes; the other is making tubular shapes with varying thickness more uniform—this could be seen in the synthetic experiments.

While curved shapes are difficult to reconstruct without a prior, the straightening of tubular shapes can be mitigated. The cause of this unwanted side effect is the deformable registration step. This deformation is necessary to estimate the inverse of the secondary deformations due to sectioning, but it also allows sections with different diameters from their neighbors to deform towards those neighbors. One way to avoid the unwanted component of the deformation is to prevent the deformable registration to change the volume of the moving sections. This would allow the sections to deform towards the reference shape, but would prevent the stretching or shrinking of the tissue.

Investigating better shape estimation methods is also an interesting direction for future work.

BIBLIOGRAPHY

- Adler, D. H., Pluta, J., Kadivar, S., Craige, C., Gee, J. C., Avants, B. B., and Yushkevich, P. A. (2014). Histology-derived volumetric annotation of the human hippocampal subfields in postmortem mri. *NeuroImage*, 84:505–523.
- Ali, W. and Cohen, F. (1998). Registering coronal histological 2-d sections of a rat brain with coronal sections of a 3-d brain atlas using geometric curve invariants and b-spline representation. *IEEE Transactions on Medical Imaging*, 17(6):957–966.
- Amat, F. and Keller, P. J. (2013). Towards comprehensive cell lineage reconstructions in complex organisms using light-sheet microscopy. *Development, Growth and Differentiation*, 55(4):563–578.
- Andreasen, A., Drewes, A., Assentoft, J., and Larsen, N. (1992). Computer-assisted alignment of standard serial sections without use of artificial landmarks. a practical approach to the utilization of incomplete information in 3-d reconstruction of the hippocampal region. *Journal of Neuroscience Methods*, 45(3):199–207.
- Avants, B. B., Tustison, N. J., Song, G., and Gee, J. C. (2009). Ants: Open-source tools for normalization and neuroanatomy.
- Ayala, R., Shu, T., and Tsai, L.-H. (2007). Trekking across the brain: The journey of neuronal migration. *Cell*, 128(1):29–43.
- Bailey, A. (1998). A clinicopathological study of autism. *Brain*, 121(5):889–905.
- Barkovich, A. J., Kjos, B. O., Jackson, D. E., and Norman, D. (1988). Normal maturation of the neonatal and infant brain: Mr imaging at 1.5 t. *Radiology*, 166(1):173–180.
- Bill, B. R. and Geschwind, D. H. (2009). Genetic advances in autism: heterogeneity and convergence on shared pathways. *Current Opinion in Genetics and Development*, 19(3):271–278.
- Born, G. (1883). Die plattenmodellirmethode. *Archiv für Mikroskopische Anatomie*, 22(1):584–599.
- Broit, C. (1981). *Optimal Registration of Deformed Images*. MS-CIS. University of Pennsylvania.
- Burton, R. A. B., Lee, P., Casero, R., Garny, A., Siedlecka, U., Schneider, J. E., Kohl, P., and Grau, V. (2014). Three-dimensional histology: tools and application to quantitative assessment of cell-type distribution in rabbit heart. *Europace*, 16(suppl 4):iv86–iv95.
- Capitanio, J. P. and Emborg, M. E. (2008). Contributions of non-human primates to neuroscience research. *The Lancet*, 371(9618):1126–1135.
- Carlsson, H.-E., Schapiro, S. J., Farah, I., and Hau, J. (2004). Use of primates in research: A global overview. *American Journal of Primatology*, 63(4):225–237.
- Casero, R., Siedlecka, U., Jones, E. S., Gruscheski, L., Gibb, M., Schneider, J. E., Kohl, P., and Grau, V. (2017). Transformation diffusion reconstruction of three-dimensional histology volumes from two-dimensional image stacks. *Medical Image Analysis*, 38:184–204.
- Casey, B., Tottenham, N., Liston, C., and Durston, S. (2005). Imaging the developing brain: what have we learned about cognitive development? *Trends in Cognitive Sciences*, 9(3):104–110.

- Ceritoglu, C. (2010). Large deformation diffeomorphic metric mapping registration of reconstructed 3d histological section images and in vivo mr images. *Frontiers in Human Neuroscience*.
- Christensen, G., Rabbitt, R., and Miller, M. (1996). Deformable templates using large deformation kinematics. *IEEE Transactions on Image Processing*, 5(10):1435–1447.
- Chuang, N., Mori, S., Yamamoto, A., Jiang, H., Ye, X., Xu, X., Richards, L. J., Nathans, J., Miller, M. I., Toga, A. W., and et al. (2011). An mri-based atlas and database of the developing mouse brain. *NeuroImage*, 54(1):80–89.
- Chung, K. and Deisseroth, K. (2013). Clarity for mapping the nervous system. *Nature Methods*, 10(6):508–513.
- Cifor, A., Bai, L., and Pitiot, A. (2011). Smoothness-guided 3-d reconstruction of 2-d histological images. *NeuroImage*, 56(1):197–211.
- Cohen, F., Yang, Z., Huang, Z., and Nianov, J. (1998). Automatic matching of homologous histological sections. *IEEE Transactions on Biomedical Engineering*, 45(5):642–649.
- Collignon, A., Maes, F., Delaere, D., Vandermeulen, D., Suetens, P., and Marchal, G. (1995). Automated multi-modality image registration based on information theory. In: *Bizais*.
- Csapo, I., Davis, B., Shi, Y., Sanchez, M., Styner, M., and Niethammer, M. (2012a). Longitudinal image registration with non-uniform appearance change. *Lecture Notes in Computer Science*, page 280–288.
- Csapo, I., Davis, B., Shi, Y., Sanchez, M., Styner, M., and Niethammer, M. (2012b). Temporally-dependent image similarity measure for longitudinal analysis. *Lecture Notes in Computer Science*, page 99–109.
- Csapo, I., Davis, B., Shi, Y., Sanchez, M., Styner, M., and Niethammer, M. (2013). Longitudinal image registration with temporally-dependent image similarity measure. *IEEE Transactions on Medical Imaging*, 32(10):1939–1951.
- Dauguet, J., Delzescaux, T., Condé, F., Mangin, J.-F., Ayache, N., Hantraye, P., and Frouin, V. (2007). Three-dimensional reconstruction of stained histological slices and 3d non-linear registration with in-vivo mri for whole baboon brain. *Journal of Neuroscience Methods*, 164(1):191–204.
- Dean, D. C., O’Muirheartaigh, J., Dirks, H., Waskiewicz, N., Lehman, K., Walker, L., Piryatinsky, I., and Deoni, S. C. (2015). Estimating the age of healthy infants from quantitative myelin water fraction maps. *Human Brain Mapping*, 36(4):1233–1244.
- Dean, D. C., O’Muirheartaigh, J., Dirks, H., Waskiewicz, N., Walker, L., Doernberg, E., Piryatinsky, I., and Deoni, S. C. L. (2014). Characterizing longitudinal white matter development during early childhood. *Brain Structure and Function*, 220(4):1921–1933.
- Deisseroth, K. (2015). Optogenetics: 10 years of microbial opsins in neuroscience. *Nature Neuroscience*, 18(9):1213–1225.
- Di Cristo, G. (2007). Development of cortical gabaergic circuits and its implications for neurodevelopmental disorders. *Clinical Genetics*, 72(1):1–8.
- Dobbing, J. and Sands, J. (1973). Quantitative growth and development of human brain. *Archives of Disease in Childhood*, 48(10):757–767.

- Durrleman, S., Pennec, X., Trounev, A., Gerig, G., and Ayache, N. (2009). Spatiotemporal atlas estimation for developmental delay detection in longitudinal datasets. *Lecture Notes in Computer Science*, page 297–304.
- Evsyukova, I., Plestant, C., and Anton, E. (2013). Integrative mechanisms of oriented neuronal migration in the developing brain. *Annual Review of Cell and Developmental Biology*, 29(1):299–353.
- Fekedulegn, D., Mac Siurtain, M., and Colbert, J. (1999). Parameter estimation of nonlinear growth models in forestry. *Silva Fennica*, 33(4).
- Fischer, B. and Modersitzki, J. (2003). *Journal of Mathematical Imaging and Vision*, 18(1):81–85.
- Fischl, B., Salat, D. H., Busa, E., Albert, M., Dieterich, M., Haselgrove, C., van der Kouwe, A., Killiany, R., Kennedy, D., Klaveness, S., and et al. (2002). Whole brain segmentation. *Neuron*, 33(3):341–355.
- Fishbaugh, J., Durrleman, S., and Gerig, G. (2011). Estimation of smooth growth trajectories with controlled acceleration from time series shape data. *Medical Image Computing and Computer-Assisted Intervention – MICCAI 2011*, page 401–408.
- Friess, S. H., Ichord, R. N., Owens, K., Ralston, J., Rizol, R., Overall, K. L., Smith, C., Helfaer, M. A., and Margulies, S. S. (2007). Neurobehavioral functional deficits following closed head injury in the neonatal pig. *Experimental Neurology*, 204(1):234–243.
- Friston, K. J., Ashburner, J., Frith, C. D., Poline, J.-B., Heather, J. D., and Frackowiak, R. S. J. (1995). Spatial registration and normalization of images. *Human Brain Mapping*, 3(3):165–189.
- Gaffling, S., Daum, V., Steidl, S., Maier, A., Kostler, H., and Hornegger, J. (2015). A gauss-seidel iteration scheme for reference-free 3-d histological image reconstruction. *IEEE Transactions on Medical Imaging*, 34(2):514–530.
- Gardella, D., Hatton, W. J., Rind, H. B., Rosen, G. D., and von Bartheld, C. S. (2003). Differential tissue shrinkage and compression in the z-axis: implications for optical disector counting in vibratome-, plastic- and cryosections. *Journal of Neuroscience Methods*, 124(1):45–59.
- Ghashghaei, H. T., Lai, C., and Anton, E. S. (2007). Neuronal migration in the adult brain: are we there yet? *Nature Reviews Neuroscience*, 8(2):141–151.
- Gilmore, J. H., Shi, F., Woolson, S. L., Knickmeyer, R. C., Short, S. J., Lin, W., Zhu, H., Hamer, R. M., Styner, M., and Shen, D. (2011). Longitudinal development of cortical and subcortical gray matter from birth to 2 years. *Cerebral Cortex*, 22(11):2478–2485.
- Goldszal, A. (1995). Three-dimensional reconstruction of activated columns from 2-[14c]deoxy-?-glucose data. *NeuroImage*, 2(1):9–20.
- Guo, J. and Anton, E. (2014). Decision making during interneuron migration in the developing cerebral cortex. *Trends in Cell Biology*, 24(6):342–351.
- Harlow, H., Harlow, M., and Suomi, S. (1971). From Thought to Therapy: Lessons from a Primate Laboratory. *American Scientist*, 59:538–549.
- Hibbard, L. S. and Hawkins, R. A. (1988). Objective image alignment for three-dimensional reconstruction of digital autoradiograms. *Journal of Neuroscience Methods*, 26(1):55–74.

- Higginbotham, H., Eom, T.-Y., Mariani, L., Bachleda, A., Hirt, J., Gukassyan, V., Cusack, C. L., Lai, C., Caspary, T., and Anton, E. (2012). Arl13b in primary cilia regulates the migration and placement of interneurons in the developing cerebral cortex. *Developmental Cell*, 23(5):925–938.
- Hikishima, K., Sawada, K., Murayama, A., Komaki, Y., Kawai, K., Sato, N., Inoue, T., Itoh, T., Momoshima, S., Iriki, A., and et al. (2013). Atlas of the developing brain of the marmoset monkey constructed using magnetic resonance histology. *Neuroscience*, 230:102–113.
- Horn, B. K. and Schunck, B. G. (1981). Determining optical flow. *Artificial Intelligence*, 17(1-3):185–203.
- Huang, H., Yamamoto, A., Hossain, M. A., Younes, L., and Mori, S. (2008). Quantitative cortical mapping of fractional anisotropy in developing rat brains. *Journal of Neuroscience*, 28(6):1427–1433.
- IBSR (2007). Internet brain segmentation repository (IBSR) [Online]. Available: <http://www.cma.mgh.harvard.edu/ibsr>.
- Jacobs, M. A., Windham, J. P., Soltanian-Zadeh, H., Peck, D. J., and Knight, R. A. (1999). Registration and warping of magnetic resonance images to histological sections. *Medical Physics*, 26(8):1568–1578.
- Ju, T., Warren, J., Carson, J., Bello, M., Kakadiaris, I., Chiu, W., Thaller, C., and Eichele, G. (2006). 3d volume reconstruction of a mouse brain from histological sections using warp filtering. *Journal of Neuroscience Methods*, 156(1-2):84–100.
- Just, M. A., Keller, T. A., Malave, V. L., Kana, R. K., and Varma, S. (2012). Autism as a neural systems disorder: A theory of frontal-posterior underconnectivity. *Neuroscience and Biobehavioral Reviews*, 36(4):1292–1313.
- Kay, P. A., Robb, R. A., Bostwick, D. G., and Camp, J. J. (1996). Robust 3-d reconstruction and analysis of microstructures from serial histologic sections, with emphasis on microvessels in prostate cancer. *Visualization in Biomedical Computing*, page 129–134.
- Keller, P. and Ahrens, M. (2015). Visualizing whole-brain activity and development at the single-cell level using light-sheet microscopy. *Neuron*, 85(3):462–483.
- Khimchenko, A., Deyhle, H., Schulz, G., Schweighauser, G., Hench, J., Chicherova, N., Bikis, C., Hieber, S. E., and Müller, B. (2016). Extending two-dimensional histology into the third dimension through conventional micro computed tomography. *NeuroImage*, 139:26–36.
- Kim, B., Boes, J. L., Frey, K. A., and Meyer, C. R. (1997). Mutual information for automated unwarping of rat brain autoradiographs. *NeuroImage*, 5(1):31–40.
- Kim, B., Frey, K. A., Mukhopadhyay, S., Ross, B. D., and Meyer, C. R. (1995). Co-registration of mri and autoradiography of rat brain in three-dimensions following automatic reconstruction of 2d data set. *Computer Vision, Virtual Reality and Robotics in Medicine*, page 262–266.
- Kinney, H. C., Karthigasan, J., Borenshteyn, N. I., Flax, J. D., and Kirschner, D. A. (1994). Myelination in the developing human brain: Biochemical correlates. *Neurochemical Research*, 19(8):983–996.
- Knickmeyer, R. C., Gouttard, S., Kang, C., Evans, D., Wilber, K., Smith, J. K., Hamer, R. M., Lin, W., Gerig, G., and Gilmore, J. H. (2008). A structural mri study of human brain development from birth to 2 years. *Journal of Neuroscience*, 28(47):12176–12182.

- Lacreuse, A. and Herndon, J. G. (2008). Nonhuman primate models of cognitive aging. *Animal Models of Human Cognitive Aging*, page 1–30.
- Li, G., Nikolova, S., and Bartha, R. (2006). Registration of in vivo magnetic resonance t1-weighted brain images to triphenyltetrazolium chloride stained sections in small animals. *Journal of Neuroscience Methods*, 156(1-2):368–375.
- Lichtman, J. W. and Smith, S. J. (2008). Seeing circuits assemble. *Neuron*, 60(3):441–448.
- Lipp, H.-P. and Bonfanti, L. (2016). Adult neurogenesis in mammals: Variations and confusions. *Brain, Behavior and Evolution*, 87(3):205–221.
- Loeckx, D., Slagmolen, P., Maes, F., Vandermeulen, D., and Suetens, P. (2010). Nonrigid image registration using conditional mutual information. *IEEE Transactions on Medical Imaging*, 29(1):19–29.
- Lupien, S. J., McEwen, B. S., Gunnar, M. R., and Heim, C. (2009). Effects of stress throughout the lifespan on the brain, behaviour and cognition. *Nature Reviews Neuroscience*, 10(6):434–445.
- Majka, P., Chaplin, T. A., Yu, H.-H., Tolpygo, A., Mitra, P. P., Wójcik, D. K., and Rosa, M. G. (2016). Towards a comprehensive atlas of cortical connections in a primate brain: Mapping tracer injection studies of the common marmoset into a reference digital template. *Journal of Comparative Neurology*, 524(11):2161–2181.
- Makropoulos, A., Aljabar, P., Wright, R., Hüning, B., Merchant, N., Arichi, T., Tusor, N., Hajnal, J. V., Edwards, A. D., Counsell, S. J., and et al. (2016). Regional growth and atlasing of the developing human brain. *NeuroImage*, 125:456–478.
- Marín, O. and Rubenstein, J. L. (2003). Cell migration in the forebrain. *Annual Review of Neuroscience*, 26(1):441–483.
- McEwen, B. S. (1994). The plasticity of the hippocampus is the reason for its vulnerability. *Seminars in Neuroscience*, 6(4):239–246.
- Metin, C., Vallee, R. B., Rakic, P., and Bhide, P. G. (2008). Modes and mishaps of neuronal migration in the mammalian brain. *Journal of Neuroscience*, 28(46):11746–11752.
- Miller, M. and Younes, L. (2001). *International Journal of Computer Vision*, 41(1/2):61–84.
- Model, M. A. and Burkhardt, J. K. (2001). A standard for calibration and shading correction of a fluorescence microscope. *Cytometry*, 44(4):309–316.
- Modersitzki, J. (2009). Fair.
- Morton, P. D., Ishibashi, N., and Jonas, R. A. (2017). Neurodevelopmental abnormalities and congenital heart disease. *Circulation Research*, 120(6):960–977.
- Oh, S. W., Harris, J. A., Ng, L., Winslow, B., Cain, N., Mihalas, S., Wang, Q., Lau, C., Kuan, L., Henry, A. M., and et al. (2014). A mesoscale connectome of the mouse brain. *Nature*, 508(7495):207–214.
- Osten, P. and Margrie, T. W. (2013). Mapping brain circuitry with a light microscope. *Nature Methods*, 10(6):515–523.
- Otsu, N. (1979). A threshold selection method from gray-level histograms. *IEEE Transactions on Systems, Man, and Cybernetics*, 9(1):62–66.

- Ourselin, S., Roche, A., Subsol, G., Pennec, X., and Ayache, N. (2001). Reconstructing a 3d structure from serial histological sections. *Image and Vision Computing*, 19(1-2):25–31.
- Periaswamy, S. and Farid, H. (2003). Elastic registration in the presence of intensity variations. *IEEE Transactions on Medical Imaging*, 22(7):865–874.
- Rangarajan, A., Chui, H., Mjolsness, E., Pappu, S., Davachi, L., Goldman-Rakic, P., and Duncan, J. (1997). A robust point-matching algorithm for autoradiograph alignment. *Medical Image Analysis*, 1(4):379–398.
- Rees, S. and Inder, T. (2005). Fetal and neonatal origins of altered brain development. *Early Human Development*, 81(9):753–761.
- Riley, E. P., Infante, M. A., and Warren, K. R. (2011). Fetal alcohol spectrum disorders: An overview. *Neuropsychology Review*, 21(2):73–80.
- Roche, A., Guimond, A., Ayache, N., and Meunier, J. (2000). Multimodal elastic matching of brain images. *Computer Vision — ECCV 2000*, page 511–527.
- Saalfeld, S., Fetter, R., Cardona, A., and Tomancak, P. (2012). Elastic volume reconstruction from series of ultra-thin microscopy sections. *Nature Methods*, 9(7):717–720.
- Sadeghi, N., Prastawa, M., Fletcher, P. T., Wolff, J., Gilmore, J. H., and Gerig, G. (2013). Regional characterization of longitudinal dt-mri to study white matter maturation of the early developing brain. *NeuroImage*, 68:236–247.
- Salvador, R., Peña, A., Menon, D. K., Carpenter, T. A., Pickard, J. D., and Bullmore, E. T. (2004). Formal characterization and extension of the linearized diffusion tensor model. *Human Brain Mapping*, 24(2):144–155.
- Sampaio, R. C. and Truwit, C. L. (2001). *Myelination in the Developing Brain*. In: *Handbook of Developmental Cognitive Neuroscience*, pages 35–44. MIT Press.
- Schmitt, O., Modersitzki, J., Heldmann, S., Wirtz, S., and Fischer, B. (2006). Image registration of sectioned brains. *International Journal of Computer Vision*, 73(1):5–39.
- Schormann, T., von Matthey, M., Dabringhaus, A., and Zilles, K. (1993). Alignment of 3-d brain data sets originating from mr and histology. *Bioimaging*, 1(2):119–128.
- Serag, A., Aljabar, P., Counsell, S., Boardman, J., Hajnal, J. V., and Rueckert, D. (2012). Lisa: Longitudinal image registration via spatio-temporal atlases. *2012 9th IEEE International Symposium on Biomedical Imaging (ISBI)*.
- Sjöstrand, F. and Baker, R. (1958). Fixation by freezing-drying for electron microscopy of tissue cells. *Journal of Ultrastructure Research*, 1(3):239–246.
- Stenman, J., Toresson, H., and Campbell, K. (2003). Identification of two distinct progenitor populations in the lateral ganglionic eminence: Implications for striatal and olfactory bulb neurogenesis. *Journal of Neuroscience*, 23(1):167–174.
- Stille, M., Smith, E. J., Crum, W. R., and Modo, M. (2013). 3d reconstruction of 2d fluorescence histology images and registration with in vivo mr images: Application in a rodent stroke model. *Journal of Neuroscience Methods*, 219(1):27–40.

- Studholme, C., Drapaca, C., Iordanova, B., and Cardenas, V. (2006). Deformation-based mapping of volume change from serial brain mri in the presence of local tissue contrast change. *IEEE Transactions on Medical Imaging*, 25(5):626–639.
- Styner, M., Knickmeyer, R., Coe, C., Short, S. J., and Gilmore, J. (2008). Automatic regional analysis of dti properties in the developmental macaque brain. *Medical Imaging 2008: Image Processing*.
- Sun, Y. and Genton, M. G. (2011). Functional boxplots. *Journal of Computational and Graphical Statistics*, 20(2):316–334.
- Toga, A. W., Thompson, P. M., and Sowell, E. R. (2006). Mapping brain maturation. *Trends in Neurosciences*, 29(3):148–159.
- Tustison, N. J., Avants, B. B., Cook, P. A., Zheng, Y., Egan, A., Yushkevich, P. A., and Gee, J. C. (2010). N4ITK: Improved N3 bias correction. *IEEE Trans. Med. Imaging*, 29(6):1310–1320.
- Viola, P. and Wells, W. (1995). Alignment by maximization of mutual information. *Proceedings of IEEE International Conference on Computer Vision*.
- Wang, X., Qiu, R., Tsark, W., and Lu, Q. (2007). Rapid promoter analysis in developing mouse brain and genetic labeling of young neurons by doublecortin-dsred-express. *Journal of Neuroscience Research*, 85(16):3567–3573.
- Zhan, Y., Ou, Y., Feldman, M., Tomaszewski, J., Davatzikos, C., and Shen, D. (2007). Registering histologic and mr images of prostate for image-based cancer detection. *Academic Radiology*, 14(11):1367–1381.
- Zhang, J., Miller, M. I., Plachez, C., Richards, L. J., Yarowsky, P., van Zijl, P., and Mori, S. (2005). Mapping postnatal mouse brain development with diffusion tensor microimaging. *NeuroImage*, 26(4):1042–1051.
- Zilles, K. (1992). Neuronal plasticity as an adaptive property of the central nervous system. *Annals of Anatomy - Anatomischer Anzeiger*, 174(5):383–391.